

**Fabrication and Tailoring Plasmonic Properties of Two  
Dimensional (2D) Assemblies of Metal Nanostructures towards  
Engineering Novel Plasmonic Sensors**

By

**Nur Uddin Ahamad**

A thesis submitted to the Faculty of Graduate and Postdoctoral Affairs

In partial fulfillment of the requirements for the degree of

**Doctor of Philosophy**

**in**

**Chemistry**

Department of Chemistry

Carleton University

December, 2011

©Copyright

Nur Uddin Ahamad, 2011



Library and Archives  
Canada

Published Heritage  
Branch

395 Wellington Street  
Ottawa ON K1A 0N4  
Canada

Bibliothèque et  
Archives Canada

Direction du  
Patrimoine de l'édition

395, rue Wellington  
Ottawa ON K1A 0N4  
Canada

*Your file Votre référence*

*ISBN: 978-0-494-89322-7*

*Our file Notre référence*

*ISBN: 978-0-494-89322-7*

#### NOTICE:

The author has granted a non-exclusive license allowing Library and Archives Canada to reproduce, publish, archive, preserve, conserve, communicate to the public by telecommunication or on the Internet, loan, distribute and sell theses worldwide, for commercial or non-commercial purposes, in microform, paper, electronic and/or any other formats.

The author retains copyright ownership and moral rights in this thesis. Neither the thesis nor substantial extracts from it may be printed or otherwise reproduced without the author's permission.

#### AVIS:

L'auteur a accordé une licence non exclusive permettant à la Bibliothèque et Archives Canada de reproduire, publier, archiver, sauvegarder, conserver, transmettre au public par télécommunication ou par l'Internet, prêter, distribuer et vendre des thèses partout dans le monde, à des fins commerciales ou autres, sur support microforme, papier, électronique et/ou autres formats.

L'auteur conserve la propriété du droit d'auteur et des droits moraux qui protègent cette thèse. Ni la thèse ni des extraits substantiels de celle-ci ne doivent être imprimés ou autrement reproduits sans son autorisation.

---

In compliance with the Canadian Privacy Act some supporting forms may have been removed from this thesis.

While these forms may be included in the document page count, their removal does not represent any loss of content from the thesis.

Conformément à la loi canadienne sur la protection de la vie privée, quelques formulaires secondaires ont été enlevés de cette thèse.

Bien que ces formulaires aient inclus dans la pagination, il n'y aura aucun contenu manquant.

Canada

### **Abstract**

Electromagnetic mechanism of enhancement, proposed to elucidate surface enhanced Raman scattering (SERS) and Surface enhanced fluorescence (SEF), was justified by studying distance dependent enhancement of SERS and SEF using 2D self-assembled spheroidal silver nanoparticles containing probe molecules. Spacer layer between the metal surface and the probe was created by layer-by-layer deposition of oppositely charged polyelectrolytes. A decreasing trend in SERS enhancement factor and an increasing trend in SEF enhancement factor with increasing separation distance were observed, which corroborate with proposed electromagnetic mechanism of SERS and SEF. In order to fabricate effective SERS substrates by exploiting hot spots, supported 2D assemblies of silver nanocubes (NCs) with controlled interparticles distance were fabricated using LB technique. Interparticles distance in such substrates was tailored by incorporation of NCs in phospholipid monolayers in Langmuir trough and optimizing lateral surface pressure during the film transfer onto a solid surface. However, to develop plasmonic sensors with high refractive index sensitivity (RIS), investigation was performed to optimize RIS of supported and colloidal silver NCs. The size of the NCs, RI of supporting dielectric substrate, and the monolayer surface pressure were used as variables in refractive index sensing optimization. It was found that high refractive index dielectric substrates, a passive molecular spacer and large angles of incidence facilitate the detection of plasmonic response of supported 2D assemblies of nanocubes. Furthermore, a simple and robust strategy was demonstrated for assembling silver NCs into 2D hierarchical structures (uniform rounded islands, branched-parallel chains) on LB films exploiting phase behaviors of multi-components lipid mixtures in Langmuir films.

The density of the building blocks, size and shape of the resulting patterns can be controlled by tailoring the lateral surface pressure, lipid composition of the Langmuir film. Finally, integration of nanoscale coating on optical fiber with noble metal was performed to engineer fiber surface plasmon sensors. The method of electroless deposition of gold was found an effective route to generate continuous film on fiber surface pre-coated with gold nanoparticles as a precursor layer. The thickness of the gold film required to support SPR was self-optimized using a Tilted Fiber Bragg Grating sensor. The resulting fiber with gold coating of optimized thickness showed potential to develop infrared surface plasmon sensor.

## **Acknowledgements**

I am very grateful to have had an opportunity to do my Ph.D. under the supervision of Professor Anatoli Ianoul. In the last five years, I was blessed with his wisdom and impressed by his research philosophy. I cordially accepted him as my science Guru. I also appreciate his mental support at different hard times during the research period.

This work was supported by the Natural Sciences and Engineering Research Council of Canada (NSERC) and Carleton University. I thankfully acknowledge those funding authorities.

I humbly acknowledge Professor M. K. Rahman of my home university for writing a recommendation letter during my admission process to Carleton University.

I also thank my employer Shahjalal University of Science and Technology, Bangladesh, for granting me the study leave to pursue my PhD degree. A significant portion of this thesis has been peer-reviewed. I acknowledge the constructive suggestions from many of those anonymous reviewers.

A special thanks to my lab members Harrison Westwick, Bryan Quan, Graham Galway, Amy Won and Adam Bottomley with whom I enjoyed working in the lab. I also like to thank Mr. Mustafa Haider for his valuable suggestion and advice during the preparation of this thesis.

My deepest gratitude goes to my parents. My father, who has been a beacon throughout my academic life, deserves the credit for all of my academic success. My sincere gratitude goes to my brothers for their affection for me.

I would like to thank my father- and mother- in- law for taking care of my wife in my three- year- long absence.

Finally, my heartfelt thanks goes to my beloved wife, Rifat Ara Rifa, for her eternal devotion to me and her unlimited patience while anticipating the long-awaited finish of this thesis. We only spent a few days together after our marriage as I had to come back to Canada for the continuation of my PhD program. She could not come with me due to complications of visa issuance. For the last three years, even though she was thousands of miles away, did not let me feel her absence. Her constant inspiration and unconditional love helped me to finish my PhD. You did your job my Lovely!

I dedicate this thesis to my father and to my wonderful wife.

## Table of Contents

Abstract	ii
Acknowledgements	iv
Table of Contents	vi
Lists of Tables	xiii
Lists of Figures	xiii
Lists of Abbreviations	xx
<b>Chapter 1 Introduction</b>	<b>1</b>
1.1. Plasmonics: Present and future	2
1.1.1. Background	2
1.1.2. Present state of plasmonics	3
1.2. Fundamentals of plasmonics	4
1.3. Metals that support surface plasmon	7
1.4. Characterization and study of surface plasmon	8
1.5. Optimizing plasmonic properties of metal nanostructures and their 2D assemblies: Silver and gold perspective	10
1.5.1. Optimization by tailoring metal nanostructures	10
1.5.1.1. Control of Shape	10
1.5.1.2. Control of Size	11
1.5.1.3. Control of internal structure	12

**Table of Contents *continues***

1.5.2. Optimization by Controlled 2D assembly of nanostructures:	
Approaches and challenges	13
1.5.2.1. Controlling interparticle gaps in nanostructures assembly	14
1.5.2.1. (a) Substrates mediated self-assembly	15
1.5.2.1. (b) Mechanical assembly	15
1.5.3. Optimization by harnessing substrate-nanostructure Interaction	15
1.6. Cutting edge plasmonic applications of gold and silver Nanostructures	17
1.6.1. Surface plasmon resonance sensing and detection	18
1.6.2. Focusing and Concentrating Light with Nanostructures	18
1.6.2.1 Surface enhanced Raman scattering	19
1.6.2.2. Surface enhanced fluorescence	19
1.6.2.3. Control of Light with Plasmonic Antennas	20
1.6.3. Plasmonic Circuitry	20
1.6.4. Optical Fiber Probes	21
1.7. Emerging applications of plasmonic nanostructures	22
1.8. Rationale and Objectives of the thesis	24
1.9. Thesis Overview	25
2.0. References	27

**Table of Contents** *continues*

<b>Chapter 2</b>	<b>Materials and Methods</b>	<b>33</b>
2.1.	Chemical Synthesis of metal nanostructures	34
2.1.1.	Citrate Reduction	34
2.1.2.	Borohydride reduction	35
2.1.3.	Polyol synthesis method	35
2.2.	Techniques for 2D assembly of metal nanostructures	37
2.2.1	Langmuir-Blodgett Technique	37
2.2.1.1.	Theoretical background	38
2.2.1.2.	Instrumentation	40
2.2.1.3.	Preparation and deposition of LB monolayer	41
2.2.2.	Self-assembled monolayer technique	42
2.3.	Technique for analysis of nanostructures morphologies	43
2.3.1.	Atomic Force Microscopy	43
2.3.1.1.	Instrumentation	44
2.3.1.2.	Operation modes of AFM	47
2.4.	Spectroscopic analysis	49
2.4.1.	Raman Spectroscopy	49
2.4.2.	Theoretical background	51
2.4.3.	Surface enhanced Raman spectroscopy	53
2.4.4.	Instrumentation	53
2.4.2.	Ultraviolet-visible absorption spectroscopy	54

## **Table of Contents *continues***

2.4. References	56
<b>Chapter 3 Fabrication and Studying Optical Field Enhancing Effects of Self-assembled Monolayer of Silver Nanoparticles</b>	<b>58</b>
3.1. Introduction	59
3.2. Experimental	61
3.2.1. Chemicals	61
3.2.2. Preparation of Metal Nanoparticles	62
3.2.3. Preparation of Polyelectrolytes Solutions	62
3.2.4. Modification of Quartz Slides	62
3.2.5. Assembly of Nanoparticle Monolayer on Modified Quartz Substrate	62
3.2.6. Deposition of Polyelectrolytes Multilayer	63
3.2.7. Deposition of Dyes on the Substrate	63
3.2.8. Raman and Fluorescence Analysis	64
3.2.9. Topography Imaging	64
3.3. Results and Discussion	65
3.3.1. Characterization of silver nanoparticle monolayer	65
3.3.2. Growth of PE film	66
3.3.3. Monitoring fluorophore diffusion in nanocomposites	66
3.3.4. Effect of local environment on surface plasmon resonance absorption	71
3.3.5. Concentration correction for SERS and SEF	71

**Table of Contents** *continues*

3.3.6. Enhancement factor calculation	72
3.3.7. SERS activities of the substrates	72
3.3.8. SEF activities of the substrates	75
3.4. Conclusions	77
3.5. References	78
<b>Chapter 4</b>	<b>Using Phospholipid Phase Behavior to Control Inter-particle</b>
	<b>Distance in SERS-active Substrates</b>
	<b>82</b>
4.1. Introduction	83
4.2. Materials and Methods	84
4.2.1. Chemicals	84
4.2.2. Preparation of nanocubes	85
4.2.3. Purification of colloidal silver nanocubes	85
4.2.4. Preparation of LB monolayers	86
4.2.5. UV-vis measurement	86
4.2.6. Topography measurements	87
4.2.7. SERS measurement	87
4.3. Results and Discussion	87
4.3.1. Monolayers of silver nanocube substrates	87
4.3.2. Surface plasmon resonance spectra	91
4.3.3. Morphology of silver nanocube substrates	95

## **Table of Contents** *continues*

4.3.4. SERS Response of the Substrate	99
4.4. Conclusion	101
4.5. References	102
<b>Chapter 5</b>	<b>Optimizing Refractive Index Sensitivity of Supported Silver</b>
	<b>Nanocube Monolayers</b>
	<b>105</b>
5.1. Introduction	106
5.2. Materials and Methods	108
5.2.1. Chemicals	108
5.2.2. Preparation of nanocubes	108
5.2.3. Purification of colloidal silver nanocubes	109
5.2.4. Preparation of LB monolayers	110
5.2.5. UV-vis measurement	110
5.2.6. Topography measurements	111
5.3. Results and Discussion	111
5.3.1. Effect of nanocube size on the refractive index sensitivity	111
5.3.2. Refractive index sensing by supported vs. suspended nanocubes	116
5.3.2. Effect of substrate on the refractive index sensitivity	123
5.4. Conclusion	128
5.5. References	129

**Table of Contents** *continues*

<b>Chapter 6</b>	<b>Assembling Plasmonic Nanostructures into Distinct Configurations on Solid Substrates Using Lipids as Template</b>	<b>132</b>
6.1.	Introduction	133
6.2.	Materials and methods	134
6.2.1.	Chemicals	134
6.2.2.	Preparation of nanocubes	134
6.2.3.	Purification of colloidal silver nanocubes	135
6.2.4.	Preparation of LB monolayers	135
6.2.5.	UV-vis measurement	136
6.2.5.	Topography measurements	136
6.3.	Results and Discussions	137
6.3.1.	Assembly of silver nanocubes into circular islands	137
6.3.2.	Linear-branched chains of silver nanocubes	143
6.4.	Conclusion	146
6.5.	References	147
<b>Chapter 7</b>	<b>Conclusions and Recommendations for Future Work</b>	<b>149</b>
7.1.	Conclusions	150
7.2.	Recommendation for future work	153

### Lists of Tables

Table 5.1.	Refractive indices sensitivities of silver nanocubes in suspension	114
Table 5.2.	Refractive index sensitivities of supported silver nanocube monolayers on glass at low surface pressure	119
Table 5.3.	Refractive index sensitivities of monolayer of 80 nm silver nanocube on glass as a function of surface pressure	121

### List of Figures

Figure 1.1.	Stained glass window of Notre-Dame de Paris (left), Microscope slide with original colloidal gold solution synthesized by Michael Faraday(right)	3
Figure 1.2.	Schematic illustration of the two types of surface plasmon modes supported by the metal nanostructures upon interaction of light: (a) localized surface plasmon mode and (b) excitation of PSPs by Prism coupling to PSPs using Kretschmann configuration.	4
Figure 1.3.	Plot of the (a) real, $\epsilon_r$ , and (b) imaginary, $\epsilon_i$ components of the dielectric function of Ag, Au, and Si as a function of wavelength	8
Figure 1.4.	Energy level diagrams illustrating the bonding and anti-bonding plasmon hybridization modes for the dipole plasmon of nanospheres with different interparticle gaps. Spectra are shown to demonstrate how the LSPR will shift upon hybridization and its sensitivity to gap width	13
Figure 1.5.	Effect of glass substrate on LSPs modes of 60 nm silver NC (a), FEM calculated E-field amplitude around NC (b), normalized surface charge distributions of the silver nanocube plasmon modes: dipolar mode (top) and quadrupolar mode (bottom) (c) and FDTD calculated E-field enhancement of Au nanowire on Au film and Si substrate, respectively. The near-field intensities are larger for the nanowires on the metallic film (d).	16

**List of Figures continues**

Figure 1.6.	Transmission of EM wave from a quantum dot (QD) to distal place through Ag nanowire. $\Gamma_{\text{rad}}$ and $\Gamma_{\text{pl}}$ are the emission rates into free space or guided plasmon modes, respectively	20
Figure 1.7.	Designs of next generation plasmonic devices: superlens (a), plasmonic solar cell (b) and SPASER (c)	22
Figure 2.1.	Formation processes of silver nanocubes and other morphologies in polyol synthesis method	36
Figure 2.2.	Typical pressure-area isotherm of a silver nanocubes monolayer (left). During the compression, the monolayer undergoes different phases i.e.; (a) gas phase, (b) liquid extended phase, (c) liquid condensed phase and (d) Solid phase. Organizations of constituent nanostructures in different phases (inset). A cross section of LB trough (right) showing (a) Trough boundary, (b) single barrier, (c) well for film deposition, (d) surface pressure sensor, (e) upward-pulling substrate, (f) a Langmuir monolayer of silver nanocubes and (g) water sub-phase	40
Figure 2.3.	Fabrication of self-assembled monolayers of nanoparticles; Silanization approach (a) and polyelectrolytes deposition approach (b)	43
Figure 2.4.	Schematic diagram of different components in an atomic force microscope (AFM)	44
Figure 2.5.	Schematic illustration of Stokes and anti-Stokes Raman effects in both non-resonance and resonance Raman scatterings	50
Figure 2.6.	Schematic diagram of basic components in a Raman spectrophotometer	54
Figure 2.7.	Diagram of a standard double beam UV-vis absorption spectrophotometer	55
Figure 3.1.	(A) AFM topography image of a substrate containing a monolayer of silver nanoparticles deposited on modified quartz slide, (B) the corresponding surface plasmon resonance absorption spectra of the Ag nanoparticle	

**List of Figures** continues

- monolayer (solid line) and the spectrum of the colloidal nanoparticles solution (dotted line) 65
- Figure 3.2. (A) UV-Vis absorption spectra of the substrates containing nanoparticles, a variable number (1, 5, 10, 20 and 30) of PE bilayers (PSS/PDADMAC) and Rh6G. Solution phase spectrum of Rh6G ( $1 \times 10^{-6}$  M, pH~2.5) is shown to track the position of Rh6G absorption signal of the substrates. (B) Absorbance at 227 nm was used to monitor the growth of PE film. (C) Position of surface plasmon (SP) absorption maxima shifts as the number of PE bilayers increases 67
- Figure 3.3. Dependence of Rh6G absorption intensity with increasing number (1, 5, 10, 20 and 30) of PE bilayers 68
- Figure 3.4. (A) UV-Vis absorption spectra of the substrates containing nanoparticle-monolayer, a variable number (1, 5, 10, 20 and 30) of PE bilayers (PSS/PDADMAC) and PAH-FITC. Solution phase spectrum of PAH-FITC ( $1 \times 10^{-6}$  M, pH~4) is shown to track the position of PAH-FITC absorption signal. (B) Absorbance at 227 nm was used to monitor the growth of PE film. (C) Position of surface plasmon (SP) absorption maxima shifts as a function of number of PE bilayers 69
- Figure 3.5. UV-Vis absorption spectra of the substrates without NP containing variable number (1, 5, 10, 20 and 30) of PE bilayers (PSS/PAH-FITC). PSS absorption at 227 nm was observed only after the deposition of 5 bilayers and a detectable FITC absorption (at 496 nm) signal was seen after deposition of 10 bilayers. Growth of PSS/PAH-FITC PE film (absorption @ 227 nm) and variation of FITC absorption intensities (absorption @ 496 nm) with increasing number of PE bilayers are shown 70
- Figure 3.6. SERS spectra (with fluorescence background) for substrates containing a monolayer of Ag nanoparticles covered with variable number (1, 5, 10, 20 and 30) of PE bilayers (PSS/PDADMAC) and Rh6G. '0' refers to a substrate used as control with Rh6G deposited on bare (without Ag NP and PE bilayers) quartz slide 74

### List of Figures continues

- Figure 3.7. Distance dependence of the Rh6G SERS signal measured by using the intensity of the Raman scattering band at  $1665\text{ cm}^{-1}$  as a function of the number of bilayers from the figure 3.6 spectra. Intensity was adjusted by using the figure 3.3 data for the amount of Rh6G deposited on the substrates 74
- Figure 3.8. Fluorescence emission spectra of the substrates containing Ag NPs, a variable number (1, 5, 10, 20 and 30) of PE bilayers (PSS/PDADMAC) with three PSS/PAH-FITC bilayers adsorbed on the top. '0' refers to a substrate used as control having PAH-FITC deposited on bare (without Ag NP and PE bilayers) quartz slide 76
- Figure 3.9. Distance dependent fluorescence enhancement of Rh6G (triangle) and FITC (rectangle) deposited on substrates containing Ag and with increasing number (1, 5, 10, 20 and 30) of PE bilayers (PSS/PDADMAC). '0' refers to the substrates used as controls having Rh6G or PAH-FITC deposited on bare (without NP and PE bilayers) quartz slides. The enhancement factors for Rh6G and FITC were estimated from the emission spectra presented in Figures 3.6 and 3.8 respectively 77
- Figure 4.1. Compression isotherm of pure (solid line) and 1:1 mixture of DPPE/DPPE-RhB (dashed line) 89
- Figure 4.2. Surface pressure-area isotherm of Langmuir monolayers of silver nanocubes (solid line), nanocubes mixed with DPPE (broken line) and nanocubes with DPPE/DPPE-RhB 1/1 mixture (dashed line) 90
- Figure 4.3. UV-vis absorption spectra of colloidal silver nanocubes with edge length 80 nm dissolved in chloroform 92
- Figure 4.4. UV-vis absorption spectra of silver nanocube substrates deposited at different surface pressure (0.1, 5, 15, 20, 25 and 35 mN/m) 94

**List of Figures continues**

- Figure 4.5. UV-vis absorption spectra of substrates prepared from silver nanocubes mixed with DPPE/DPPE-RhB and deposited at different surface pressure (0.1, 5, 15, 25 and 35 mN/m) 94
- Figure 4.6. UV-vis absorption spectra of substrates prepared from silver nanocubes mixed with DPPE and deposited at different surface pressure (0.1, 5, 15, 20, 25 and 35 mN/m) 95
- Figure 4.7. AFM topography images of silver nanocube substrates deposited at different surface pressure (0.1, 15 and 35 mN/m) 96
- Figure 4.8. AFM topography images of substrates of nanocubes mixed with DPPE/DPPE-RhB and deposited at different surface pressure (0.1, 15 and 35n mN/m) 98
- Figure 4.9. AFM topographic images of substrates of nanocubes mixed with DPPE and deposited at different surface pressure (0.1, 15 and 35 mN/m) 99
- Figure 4.10. Surface enhanced Raman scattering spectra measured for substrates composed of silver nanocubes and DPPE/DPPE-RhB lipid mixture at different surface pressure (0.1, 15, 20, 25 and 35 mN/m). The reference spectrum was measured for DPPE/DPPE-RhB deposited on glass slide without nanocubes at 35mN/m 100
- Figure 4.11. Surface pressure dependent relative (to the values at surface pressure of 0.1 mN/m) intensities of (a) SERS peak at  $1651\text{cm}^{-1}$ ; (b) fluorescence, and (c) background intensity measured for DPPE/DPPE-RhB without nanocubes 101
- Figure 5.1. AFM topographic images of supported nanocube substrates prepared by Langmuir monolayer technique at low (0.1-1 mN/m, 15mN/m for 130 nm cubes) surface pressure. The histograms show height distribution in the samples (bottom, left) 112

**List of Figures continues**

- Figure 5.2. Extinction spectra of colloidal suspensions in different water/ethylene glycol solutions for A: 40 nm, B: 80 nm, and C: 130 nm nanocubes. The spectra were measured in water (lowest spectra in series), followed by water: EG 4:1, ethanol (40 and 80 nm only), water: EG 3:2, 2:3, 1:4, and pure EG 113
- Figure 5.3. Plasmonic shifts as functions of refractive index for silver nanocube suspensions 115
- Figure 5.4. Extinction spectra of supported nanocube monolayers in air (lowest spectra in series) and immersed in different water/ethylene glycol solutions for A: 40 nm on a glass substrate, B: 40 nm on a glass substrates coated with 5 nm TiO<sub>2</sub> film; C: 80 nm, and D: 130 nm nanocubes. The spectra were measured in water (first spectra in series), followed by water: EG 4:1, water: EG 3:2, 2:3, 1:4, and pure EG 117
- Figure 5.5. Plasmonic shifts as functions of refractive index for supported silver nanocubes 120
- Figure 5.6. UV-vis spectra of supported 40 nm nanocubes (A) and irregular shaped nanoparticles (B) on different substrates: (1) quartz, (2) glass, (3) sapphire, (4) glass slide with coated with 5 nm TiO<sub>2</sub> film, (5) glass slide coated with 5 nm of silicon, (6) spectra of suspensions in ethanol 123
- Figure 5.7. Plasmon shift of the dipolar (diamonds) and quadrupolar (squares, cubes only) bands in extinction spectra of supported 40 nm Ag nanocubes (open symbols) and irregular Ag nanoparticles (filled symbols) as a function of support refractive index 124
- Figure 5.8. UV-vis spectra of supported 80 nm nanocubes on different substrates: quartz, sapphire, glass slide with coated with 5 nm TiO<sub>2</sub> film, glass slide coated with 5 nm of silicon (left). Plasmon shifts plotted vs. the refractive index of a substrate (right) 125

**List of Figures continues**

- Figure 5.9. Angular dependence of UV-vis extinction spectra for 40 nm nanocubes deposited on different substrates 127
- Figure 6.1. AFM topography images (top,  $50 \times 50 \mu\text{m}^2$  and bottom,  $10 \times 10 \mu\text{m}^2$ ) of DOPC/SPM/cholesterol (2:2:1)/NCs monolayers deposited on glass at different surface pressures 139
- Figure 6.2. AFM topographic images (top,  $50 \times 50 \mu\text{m}^2$  and bottom,  $10 \times 10 \mu\text{m}^2$ ) of DOPC/SPM/cholesterol (1:1:1)/NCs monolayers deposited on glass at different surface pressures 140
- Figure 6.3. Extinction spectra of glass supported monolayers of DOPC/SPM/cholesterol (2:2:1)/NCs (dashed line) and DOPC/SPM/cholesterol (1:1:1)/NCs (solid line). The transfer pressure for both monolayers was 10 mN/m 141
- Figure 6.4. AFM topographic images of DOPC/NCs monolayer deposited on glass at 10 mN/m surface pressure 142
- Figure 6.5. AFM topography images of DPPC/DLPC (1/3)/NCs deposited on mica at two different surface pressures (A) 15 mN/m, (B) 32 mN/m. (C) AFM topography image of DPPC/NCs deposited at 32 mN/m 144
- Figure 6.6. AFM topography images of DPPC/DLPC (1/3)/NCs monolayer deposited on glass at 15 and 32 mN/m surface pressures 145
- Figure 7.1. Schematic diagram of TFBG-SPR sensor platform (a), SEM image of the fiber's circumference after 45 min of electroless deposition (b), response of the TRBG-SPR sensor to the LBL deposition of polyelectrolytes (c) and AFM image of a LB monolayer of silver NCs deposited on the fiber surface (d) 155

## List of Abbreviations

NPs	Nanoparticles
SP	Surface plasmons
SPR	Surface plasmon resonance
LSPs	Localized surface plasmons
PSPs	Surface plasmon polaritons
LSPR	Localized surface plasmon resonance
Q	Quality factor
PA	Photo-acoustic
PHI	Photo-thermal heterodyne imaging
SERS	Surface enhanced Raman scattering spectroscopy
SEF	Surface enhanced fluorescence
NSOM	Near-field scanning optical microscopy
DDA	Discrete dipole approximation
FSTD	Finite difference time domain method
FEM	Finite element method
EM	Electromagnetic field
NWs	Nanowires
LTs	Lithographic techniques
SPAM	Solution-phase assembling methods
LB	Langmuir-Blodgett
NC	Nanocube
QD	Quantum dot
LPG	Long-period fiber grating
TFBG	Tilted fiber Bragg grating
SPASER	Surface plasmon amplification by stimulated emission of radiation
RIS	Refractive index sensitivity
FOM	Figure of merit
PVP	Polyvinylpyrrolidone
EG	Ethylene glycol
$\Pi$	Surface pressure
LE	Liquid extended phase
LC	Liquid condensed phase
PSS	Poly (sodium-4-styrenesulfonate)
PDADMAC	Poly (diallyldimethylammonium chloride)
APTMS	3-aminopropyltrimethoxy-silane
AFM	Atomic force microscopy
FIB	Focused ion beam
EBD	Electron beam deposition
Rh6G	Rhodamine 6G
PE	Polyelectrolyte

**List of Abbreviations continues**

SAM	Self-assembly monolayer
LBL	Layer by layer
PAH-FITC	Poly (fluorescein isothiocyanate allylamine hydrochloride)
CF	Correction factor
DPPE	1, 2-Dipalmitoyl-sn-Glycero-3-Phosphoethanolamine
DPPE-RhB	1, 2-Dipalmitoyl-sn-Glycero-3-Phosphoethanolamine-N- (lissamine rhodamine B) sulfonyl
PTFE	Polytetrafluoroethylene
FWHM	Full width at half maximum
RIU	Refractive index unit
D	Dipolar mode
Q	Quadrupolar mode
RI	Refractive index
DOPC	1, 2-dioleoyl-sn-glycero-3-phosphocholine
SPM	Sphingomyelin
DPPC	1, 2- dipalmitoyl-sn-glycero-3-phosphocholine
DLPC	1, 2-Dilauroyl-sn-glycero-3-phosphocholine

## **Chapter 1**

---

### **Introduction**

## **1.1. Plasmonics: Present and future**

### ***1.1.1. Background***

Coinage metals, such as gold and silver have been used since antiquity. Due to their strong scattering properties in the visible range, they show attractive colors. One of their first applications, dating back to the Roman Empire more than 2000 years ago, was as a colorant for clothing. In art, they were used to stain window glass and ceramics. Spectacular color of reflection that can be seen in the windows of Notre-Dame de Paris, a medieval Cathedral, reveals the artistic application of gold in ancient time (Shown in figure 1.1, left).<sup>1</sup> Obviously, it was unknown in that era that the colorants being used contained metal nanoparticles (NPs) or that the spectacular colors were due to the interaction of light with metal nanoparticles. It was Michael Faraday in 1857 who first described the scientific method of preparation of colloidal gold solution which he called “a beautiful ruby fluid” and demonstrated the variation of solution colors with the size of the gold nanoparticles.<sup>2</sup> One of his original colloidal gold samples is presented in figure 1.1(right). The explanation for this observation could be found in Maxwell’s equations; however, it would not be extracted until 1908 when Gustav Mie provided an analytical solution to the equations for a sphere of arbitrary size.<sup>3</sup> Mie was able to calculate the extinction spectra (summation of absorption and scattering spectra) for metal colloids containing spherical particles of any size. In doing so, he was able to explain many of the experimental observations of his day, including the red color of Faraday’s gold colloid. Since then, the field encompassing the understanding of how light interacts with metals

on the nanometer length scale has exploded and evolved into an interdisciplinary field known as plasmonics.



Figure 1.1. Stained glass window of Notre-Dame de Paris (left), Microscope slide with original colloidal gold solution synthesized by Michael Faraday (right). Reproduced with permission from ref 1 and 2.

### ***1.1.2. Present state of plasmonics***

Modern plasmonics is related to the localization, guiding, and manipulation of electromagnetic waves beyond the diffraction limit and down to the nanometer-length scale. However, its connection with nanoscale science and technology was not widely or actively explored until recently.<sup>4</sup> Plasmonics is part of nanotechnology because nanostructures are used (i) as active components to focus, guide, and manipulate light and (ii) as building blocks for larger, more complex “metamaterials” sought for controlling light. Although the interaction of light and metal nanoparticles has long attracted the interest of scientists, plasmonics represents a relatively new level of control and study involving both nanostructures and light. In contrast to simply establishing the valuable optical properties of metal nanostructures, this interaction is now controlled for the specific purpose of manipulating the propagation of light. However, many new technologies stand to be realized from plasmonics, with notable examples including super-lenses,<sup>5</sup> invisibility cloaks<sup>6</sup>, quantum computing,<sup>7,8</sup> plasmonic solar cells<sup>9</sup> and

nano-lasers<sup>10</sup> etc. Plasmonics is also a burgeoning field of nanoscience because sophisticated models, theories, and methods are being developed to understand the interaction between a metal nanostructure and light. Plasmonics is therefore a new subfield of nanoscale science and technology that aims to understand and control light using metal nanostructures in novel ways.

## 1.2. Fundamentals of plasmonics

The delocalized electrons of a metal are often described as being a free electron “gas” (or cloud) around positively charged nuclei. When the oscillating electric field from incident light interacts with the delocalized electrons of a metal, the electron cloud can be perturbed in such a way that it is physically displaced from the metal framework and the metal structure assumes the plasma state. This charge polarization is short lived, because the Coulombic attraction from the positively charged nuclei of the metal will pull the electron cloud back to its initial position. Due to the large difference in mass, it is typically assumed that the heavy nuclei remain in a fixed position while the lighter electrons experience motion. With the electric field component of incident light acting as a sinusoidal driving force and Coulombic attraction acting as a restoring force, total

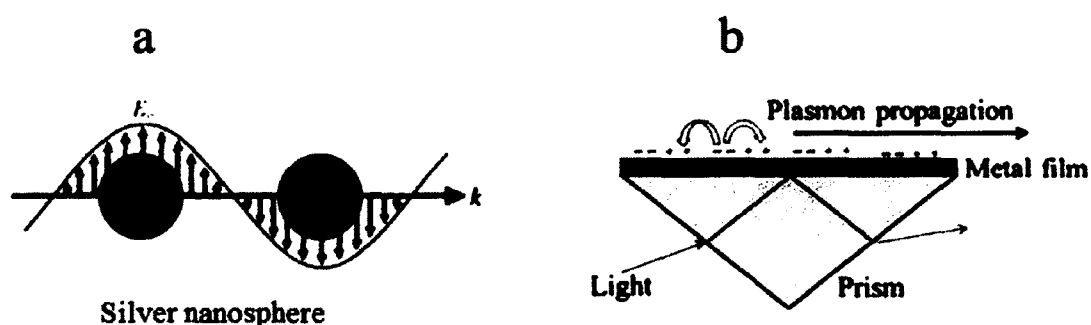


Figure 1.2. Schematic illustration of the two types of surface plasmon modes supported by the metal nanostructures upon interaction of light: (a) localized surface plasmon mode and (b) excitation of PSPs by Prism coupling to PSPs using Kretschmann configuration. Reproduced with permission from ref 11 and 13.

system behaves like a harmonic oscillator. Consequently, resonant conditions can be achieved when light is coupled in phase to the natural frequency of the plasmon oscillation. At these resonant conditions, the metal structures absorb the maximum amount of incident electromagnetic radiation, causing the greatest amount of charge displacement. However, when the light interacts with metal particle with dimension smaller than its wavelength, only the surface plasmons are excited. Under specific conditions interaction of light causes coherence oscillation of surface plasmons which is termed as surface plasmon resonance (SPR). This unique optical property of metal nanostructures plays the key role in the emerging field of plasmonics. However, depending on the dimensional characteristics of the metal nanoparticles, surface plasmon modes that they support are classified into localized surface plasmon (LSPs) and propagating surface plasmon, also called surface plasmon polaritons (PSPs). In LSPs, the time varying electric field associated with the light ( $E_0$ ) exerts a force on the gas of negatively charged electrons in the conduction band of the metal and drives them to oscillate collectively. At a certain excitation frequency ( $\omega$ ), this oscillation will be in resonance with the incident light, resulting in a strong oscillation of the surface electrons, commonly known as a localized surface plasmon resonance (LSPR) mode.<sup>11</sup> This phenomenon is illustrated in figure 1.2a. Structures that support LSPRs experience a uniform  $E_0$  when excited by light as their dimensions are much smaller than the wavelength of the light. In contrast, PSPs are supported by structures that have at least one dimension that approaches the excitation wavelength and  $E_0$  is not uniform across the structure and other effects must be considered as shown in figure 1.2b.<sup>12</sup> PSPs on a flat metal/dielectric interface cannot be excited directly by light because of phase

mismatching between the propagation constant and the wave vector of the incoming light.<sup>13</sup> However, phase matching to PSPs can be achieved in a three-layer system consisting of a thin metal film sandwiched between two insulators of different dielectric constants. Such a phase matching configuring is shown in figure 1.2b.<sup>13</sup> The ability of a metal nanoparticle to support surface plasmons (SP) is dependent on its dielectric function  $\epsilon$ , which includes a real part ( $\epsilon_r$ ) and an imaginary part ( $\epsilon_i$ ), both of which vary with excitation wavelength ( $\lambda$ ) or frequency ( $\omega$ )

$$\epsilon = \epsilon_r + i\epsilon_i \quad (1.1)$$

The real and imaginary parts of this complex dielectric function are expressed as

$$\text{Real: } \epsilon_r(\omega) = \epsilon_\infty \left(1 - \frac{\omega_p^2}{\omega^2 + \gamma_0^2}\right) \quad (1.2)$$

$$\text{Imaginary } \epsilon_i(\omega) = \frac{\epsilon_\infty \omega_p^2 \gamma_0}{\omega(\omega^2 + \gamma_0^2)} \quad (1.3)$$

$\gamma_0$  and  $\omega_p$  are the collision frequency of free electrons in the electron gas and plasma frequency respectively.  $\epsilon_\infty$  is the dielectric function including the positive ion core as background.

The optical properties of a spherical metal nanoparticle can be obtained from Mie theory by calculating its extinction cross section ( $C_{\text{ext}}$ ):<sup>14</sup>

$$C_{\text{ext}} = \frac{24\pi^2 R^3 \epsilon_m^{3/2}}{\lambda} \left[ \frac{\epsilon_i}{(\epsilon_r + 2\epsilon_m)^2 + \epsilon_i^2} \right] \quad (1.4)$$

The extinction cross section describes the probabilities of absorption and scattering of light by a nanoparticle. The larger the value, higher the probability is. Equation (1.4) shows the dependence of dielectric function of the surrounding medium to the extinction peaks of surface plasmon resonance. The resonance condition is obtained when  $\epsilon_r =$

$-2\varepsilon_m$  i.e.; the extinction cross section is maximum. Although the position of plasmon resonance of a metal nanoparticle in a dielectric medium is primarily determined by the real part of the  $\varepsilon(\omega)$ , the imaginary part determines the strength of both the surface plasmon resonances (LSP and PSP). The larger the imaginary part  $\varepsilon_i(\omega)$ , the more “lossy” surface plasmons are. For LSPR, this damping is characterized by a quality factor defined as<sup>15</sup>

$$Q = \frac{\omega \left( \frac{d\varepsilon_r}{d\omega} \right)}{2(\varepsilon_i)^2} \quad (1.5)$$

Large values of Q mean strong surface plasmons and small values indicate a lossy or weak surface plasmons. In simple terms, Q is large when  $\varepsilon_i$  is small and, therefore, characterizes the strength (and width) of the resonance. In general, Q should be larger than  $\sim 10$  for most plasmonic applications.

### 1.3. Metals that support surface plasmon

In terms of plasmonic application, it is important to choose a metal that can support a strong SP at the desired resonance wavelength as well as metals having enough stability to oxidation.<sup>16,17</sup> For supporting a strong SP, dielectric function of a metal must possess a negative real part,  $\varepsilon_r$  and small value of the imaginary part,  $\varepsilon_i$  of the dielectric function. Among the metals, gold and silver respect the dielectric function constraints in the UV-vis region of the spectrum as shown in the figure 1.3. Nonmetals typically have  $\varepsilon_r$  values between 1 and 50 and are not used in plasmonics (Figure 1.3).<sup>18</sup> Silver and gold, however, have higher quality factor across most of the spectrum from 300 to 1200 nm.<sup>19</sup>

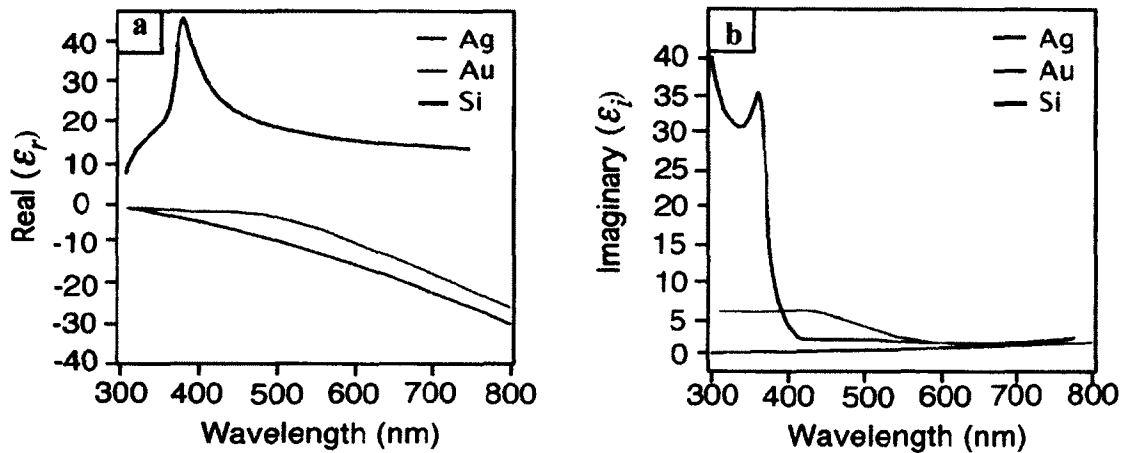


Figure 1.3. Plot of the (a) real,  $\epsilon_r$ , and (b) imaginary,  $\epsilon_i$  components of the dielectric function of Ag, Au, and Si as a function of wavelength. Reproduced with permission from ref 61.

As a disadvantage, Ag forms silver sulfide when exposed to air<sup>20,21</sup> and its nanostructures are considered to be toxic, although passivation of the surface can greatly increase their stability and thus attenuate or eliminate their toxicity.<sup>22</sup> Gold is well-known for its bio-inertness, and its surface is believed to be oxide-free. For these reasons, Au nanostructures are well-suited for in vivo applications with humans.<sup>23</sup> In contrast; Ag nanostructures are largely used in plasmonic applications outside a human body where they have consistently reported much better performance than Au-based nanostructures.<sup>24-26</sup> Gold and silver are the most promising, and indeed the most widely used, materials in plasmonics. Considering all these factors Ag and Au were chosen as the best candidates for preparation of plasmonic nanostructures in this thesis work.

#### 1.4. Characterization and study of surface plasmon

Two of the primary challenges of plasmonics are to understand and maneuver SPs at the nanoscale. Critical to these goals is an ability to fully characterize and model the

plasmonic properties of metal nanostructures. In pursuit of this goal, a number of methods have been developed to detect and image both the far- and near-field properties of plasmonic nanostructures.<sup>27,28</sup> The characterization methods can be classified into two broad classes: experimental methods and theoretical methods. Experimental method includes UV-vis-NIR spectroscopy<sup>29</sup>, dark-field microscopy<sup>30</sup>, photo-acoustic (PA) techniques<sup>31</sup>, spatial modulation spectroscopy<sup>32</sup>, photo-thermal heterodyne imaging (PHI)<sup>33</sup>, surface enhanced Raman scattering spectroscopy (SERS)<sup>34</sup>, near-field scanning optical microscopy (NSOM): aperture-based and apertureless and NSOM-Raman.<sup>35,36</sup> Theoretical modeling represents another important approach to understanding the plasmonic properties of metal nanostructures. Theoretical models create greater understanding of the effect of experimental parameters on plasmonic properties, and have been used to describe plasmon hybridization<sup>37</sup>, the substrate effect on plasmons<sup>38,39</sup>, and structures composed of different kinds of nanoparticles.<sup>40,41</sup> For a homogeneous nanosphere and an incident plane wave of light, Mie theory gives a simple solution to obtain the scattering and absorption cross sections of spherical particles.<sup>42</sup> However, for more complicated shapes with lower symmetry, such as cubes or bars, an exact solution cannot be reached and in such situation the discrete dipole approximation (DDA),<sup>43</sup> finite difference time domain (FDTD) method,<sup>44</sup> and the finite element method (FEM)<sup>45</sup> can be used. However, in our research projects, UV-vis spectroscopy and SERS were employed to detect and characterize the plasmonic properties of the nanostructures samples (Details about these techniques can be found in materials and methods chapter of this thesis report).

## **1.5. Optimizing plasmonic properties of metal nanostructures and their 2D assemblies: Silver and gold perspective**

Maneuvering plasmonic properties for development of new devices and applications require engineered nanostructures and their controlled 2D assemblies. The physical shape, size, morphology and defects in crystal structures are related to the plasmonic properties of metal nanostructures. However, interparticles gaps and supporting substrates are related to the plasmonic properties of assembled nanostructures.

### ***1.5.1. Optimization by tailoring metal nanostructures***

#### ***1.5.1.1. Control of Shape***

The specific geometry of a metal nanostructure can have a strong effect on its LSPR properties.<sup>46</sup> In general, the number of resonance peak increases as the symmetry of a structure decreases. The position of the LSPR peak can also change depending on the geometry. For example, the spectrum of the 40 nm cube contains a couple of peaks or shoulders beyond the strong dipole peak near 450 nm, whereas the spectrum of the sphere with same diameter only shows one resonance peak near 400 nm.<sup>47</sup> The sharpness of corners or edges of a nanostructure can have a large effect on its plasmonic properties. Silver nanocube, as an example, shows multiple extinction peaks corresponding to higher order plasmon modes along with dipolar mode. Each mode originates from different charge distribution in nanocube's surface. The commonly observed plasmon modes for silver NC are dipolar and quadrupolar modes. In dipolar plasmon mode the induced charges concentrated on the corners of the cube, with charges of the same sign residing on either side of the cube (Figure 1.5.c, top). This charge distribution is thus characterized by a large electric dipole moment. In quadrupolar mode, induced charges

concentrated on the corners of the cube but in a manner such that the overall dipole moment vanishes (Figure 1.5.c, bottom). Sharp corners and edges concentrate EM field.<sup>48</sup> However, structures with sharp corners red shift LSPR peaks when compared to rounded structures of similar sizes. Therefore, silver nanostructures, such as nanocubes, with sharp corners and edges are ideal for plasmonic application.

#### *1.5.1.2. Control of Size*

The simplest approach to optimize plasmonic properties of a metal nanostructure is to manipulate its dimensions. The size of a nanoparticle determines plasmonic features that include the ratio of absorption to scattering, the number of LSPR modes, the peak position of an LSPR mode, and the extent of PSP localization.<sup>14,49</sup> For small nanoparticles ( $R < \sim 30$  nm), absorption dominates over scattering. On the other hand, larger particles can scatter light more efficiently than the smaller one. The number of LSPR peaks depends on the size of the nanostructures. In general, there are only dipole excitations in small particles whereas both dipole and multi-pole excitations are possible in large particles.<sup>50</sup> In addition; an increase in size red shifted the LSPR peaks.<sup>49</sup> For example, 40-nm Ag sphere exhibits only one strong, dipole mode at 400 nm, whereas the 140-nm sphere shows a quadruple mode at  $\sim 600$  nm in addition to the dipole mode at 450 nm. For PSPs, the spatial parameters of the waveguide are also very important and can affect the number of guided modes, the spatial confinement of the PSP, and the propagation length of the PSP modes.<sup>51</sup> As the diameter of Ag or Au nanowire decreases, the PSP modes are also decreased and become confined to the center of the nanowire as opposed to the surface.<sup>52</sup> This is important for sub-wavelength localization of guided signals. However, as more of the PSP's energy is carried in the waveguide, the PSP

experiences higher energetic losses and, consequently, cannot travel long distance (millimeters for example).<sup>53</sup> Therefore, the size of the nanostructures is important to optimize their plasmonic properties for specific application.

#### *1.5.1.3. Control of internal structure*

Metal nanostructures prepared by solution phase synthesis may take different crystalline structures i.e.; single crystalline, singly twinned, multiply twinned or vertically stacked with faults. The presence of these different structures can possibly have a significant impact on the plasmonic properties of nanostructures since the defects at twin boundaries can serve as scattering centers for conduction electrons in a metal.<sup>54</sup> It was found that the multiply twinned particles transferred energy faster.<sup>55</sup> For PSPs, the effect of crystallinity has already been found to be more pronounced than for LSPRs. This is primarily because multicrystalline structures have surface defects (or roughness). For PSPs on Ag or Au nanowires waveguides, defects on these structures can serve as scattering sites where the PSP are radiated as light.<sup>55</sup> The overall propagation loss can be lowered by using single crystalline nanowires (NWs) prepared by solution phase methods, as such NWs have smoother surface and fewer defects. Another approach of tuning plasmonic properties of metal nanostructures is the alloying of metals. Silver-based alloys and core-shell nanostructures have been shown to exhibit optical properties distinct from nanoparticles of pure Ag.<sup>56</sup> One popular structure is the Ag-Au alloy nanocages/nanoboxes formed via a galvanic replacement reaction, whose LSPR peaks can be tuned across the visible spectrum and into the NIR region.<sup>57</sup> The galvanic replacement reaction can be performed with Ag nanocubes. These Ag-based alloy nanostructures have many interesting applications. For example, hollow Au-Ag

nanostructures with a LSPR in the NIR region are highly favorable for biomedical applications, including imaging,<sup>58</sup> therapies,<sup>59</sup> and controlled release.<sup>60</sup>

### ***1.5.2. Optimization by Controlled 2D assembly of nanostructures: Approaches and challenges***

Although individual nanostructures have many fascinating plasmonic properties, controlling their assembly into larger structures gives rise to more interesting collective optical properties.<sup>61</sup> When nanostructures approach one another, their far- and near-field properties can be dramatically altered as depicted in figure 1.4.<sup>61</sup>

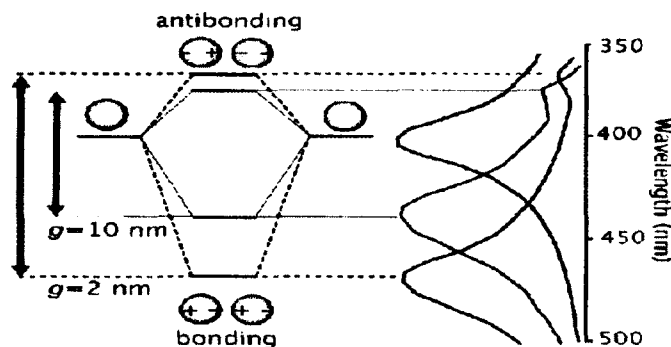


Figure 1.4. Energy level diagrams illustrating the bonding and anti-bonding plasmon hybridization modes for the dipole plasmon of nanospheres with different interparticle gaps. Spectra are shown to demonstrate how the LSPR will shift upon hybridization and its sensitivity to gap width. Reproduced with permission from ref 61.

These changes are a result of the strong coupling between the LSPs of the nanostructures during excitation. When separated by a small distance, the interaction can be viewed as hybridization between the LSPs of the nanostructures to form gap plasmons, analogous to the hybridization of atomic orbitals in a molecule.<sup>62</sup> One of the interesting results of SP coupling is that fundamentally different LSP modes are produced with

unique charge distributions and resonances. The new modes are more sensitive to the external environment than their primitive modes and therefore can be used for molecular detection.

The gap SP mode is red-shifted compared to a single nanostructure's LSPR. More importantly, the inter particles gaps can concentrate light to exceedingly small volumes and thus create huge near-field enhancements known as hot spots. Such hot spots are thought to be a good candidate for single molecular detection. For these reasons much attention has been paid to create gap plasmons in 2D assemblies of metal nanostructures.

#### *1.5.2.1. Controlling interparticle gaps in nanostructures assembly*

Both lithographic techniques (LTs) and solution-phase assembling methods (SPAM) are used to engineer 2D organization of metal nanostructures. However, it is still challenging to create 2D patterns of nanostructures with controlled nanoscopic interparticles gaps for plasmonic applications. Although, lithographic techniques produce well-defined structures over large areas, such techniques are limited by patterning on planar substrates and gaps size (not as good at producing gaps controlled below 10 nm).<sup>63</sup> On the other hand, solution phase assembling can produce gaps size below 10 nm. In addition, nanostructures synthesized by chemical process possess high degree of crystallinity and less surface-roughness. Some disadvantages of this method are placement of nanostructures on desired positions, surface attached molecules during synthesis. However, both LTS and SPAM are important to create 2D patterns of plasmonic nanostructures. In our research purpose we used self-assembly method and mechanical assembling technique like Langmuir-Blodgett.

#### 1.5.2.1 (a) Substrates mediated self-assembly

In this assembly approach, the solid substrates (planar or curved) are activated by addition of an adhesive layer.<sup>64</sup> The adhesive layer can be formed either by covalent bond or electrostatic interaction of molecules with substrates. The common adhesive molecules are amino-silane, polyelectrolytes etc.<sup>65</sup> Then the substrate is submerged into the colloidal metal nanoparticles solution for a predetermined time to get a complete coverage of the nanoparticles.

#### 1.5.2.1 (b) Mechanical assembly

Mechanical assembly is carried out by using LB technique (Details is described in materials and methods section). In this technique a water supported monolayer of nanostructures is formed and compressed to a desired surface pressure at which the monolayer is transferred onto a solid substrate. Using this technique, the number of constituent, orientation, interparticle gaps can be tuned by choosing monolayer transfer pressure.<sup>66</sup>

#### ***1.5.3. Optimization by harnessing substrate-nanostructure interaction***

Depositing metal nanostructures onto solid substrates imparts new plasmonic properties to the nanostructures. The substrate imposes an anisotropic environment to the nanoparticles. This can have unusual effects on the plasmonic properties of a nanostructure depending on the nature of the substrates. The substrate effect on a nanoparticle has only recently been investigated. However, controlling the physical properties of a supporting substrate for plasmonic applications is still in its infancy. Dielectric substrate breaks the environmental symmetry of nanostructures deposited on it and differentiates the degenerate LSPR modes of the nanostructure. As an example, glass

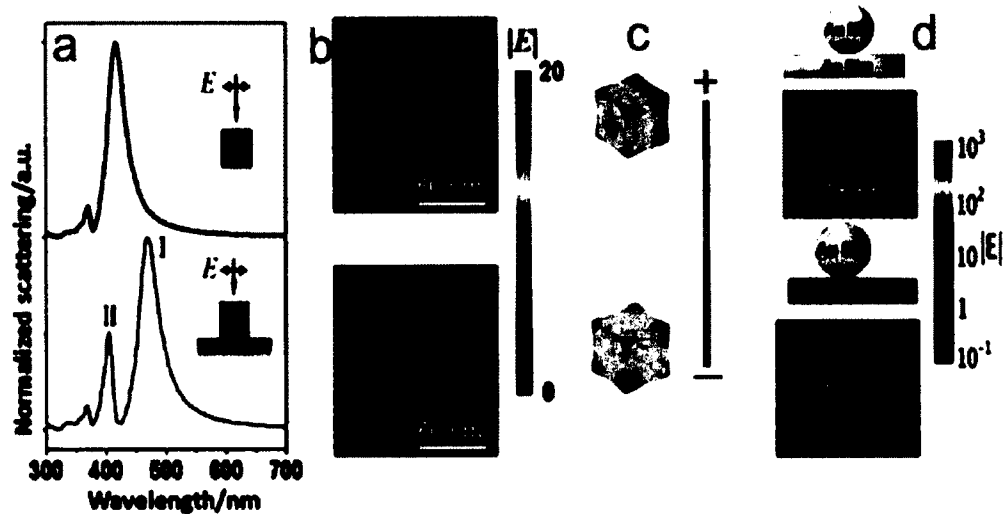


Figure 1.5. Effect of glass substrate on LSPs modes of 60 nm silver NC (a), FEM calculated E-field amplitude around NC (b), normalized surface charge distributions of the silver nanocube plasmon modes: dipolar mode (top) and quadrupolar mode (bottom) (c) and FDTD calculated E-field enhancement of Au nanowire on Au film and Si substrate, respectively. The near-field intensities are larger for the nanowires on the metallic film (d). Reproduced with permission from ref 67 and 69.

has been reported to red shift and split the LSPR of 60 nm Ag nanocubes as shown in the figure 1.5.<sup>67</sup> When the cube is in contact with the glass, dipolar (I) mode is red-shifted (while NC is in vacuum) and a new mode (II) emerges at 404 nm (figure 1.5.a). Mode (I) is oriented toward the substrate while the new mode II is oriented predominantly on the vacuum side. The scattering peaks I and II were assigned by finite element method (FEM) as shown in figure 1.5 (b). These two modes are the bonding and antibonding hybridized modes resulting from the substrate-mediated interaction of two nearly degenerate dipolar and quadrupolar modes.<sup>68</sup> Interestingly, the LSPR peak facing away from the substrate (peak II) was found to be much more sensitive to changes in the local

environment compared to LSPR peaks of Ag nanocubes in a solution. In contrast to dielectric substrates, the interaction between a metal substrate and a metal nanoparticle is more complicated and potentially much more interesting. Metal substrates (like evaporated thin films, 10-200 nm in thickness) can support PSPs, which can interact with metal nanoparticles, creating a strongly coupled plasmonic system.<sup>69</sup> The hybridization between a metal nanoparticle and metal substrate can fundamentally change the LSP modes supported by the nanoparticle. This can have profound effects on the near-fields of the nanoparticle (shown in figure 1.5. d) which may prove beneficial to surface-enhanced spectroscopies like surface enhanced Raman scattering (SERS) and surface enhanced fluorescence (SEF). Metal substrate effects are also sensitive to the distance between the nanoparticle and the substrate.<sup>70</sup> However, relatively little is known about the effects of metal substrates on the plasmonic properties of nanoparticles. Additional studies are required to determine if metal substrates can be used to effectively control the plasmonic properties of supported nanoparticles.

### **1.6. Cutting edge plasmonic applications of gold and silver nanostructures**

Plasmonics encompasses a fundamental light-matter interaction; consequently, there are many scientific fields that stand to benefit from it. Already, many applications of plasmonics have emerged in past decades like SERS, near-field optical microscopy, and LSPR-based sensing. Despite this wide range of research activities, current applications of plasmonic nanostructures can generally be categorized into three thrusts: (i) LSPR sensing and detection, (ii) concentration of light to enhance or manipulate the optical response of nearby molecules, and (iii) manipulation of light with plasmonic circuitry.

### ***1.6.1. Surface plasmon resonance sensing and detection***

Some of the first, and most successful, applications of plasmonic structures were in the detection of molecules. In this technique continuous metal films are chemically functionalized to selectively bind target molecules. Upon binding of the target molecule, the dielectric environment near the surface of the metal film is altered. Consequently, binding can be monitored by measuring the change in coupling geometry (i.e., the angle) between the metal film and the excitation source required to generate PSPs.<sup>4</sup> This technique has been extended to LSPR sensing with nanoparticles. When the dielectric environment around a plasmonic nanoparticle is changed by introducing analyte molecules, the resonance frequency of the LSPR shifts as well.<sup>71</sup> This is the foundation of LSPR sensing, and by carefully preparing the nanostructures to interact only with specific molecules, molecular binding affinities, reaction rates, conformational changes, and complex interactions can all be monitored with this technique. More recent advances in LSPR sensing and detection have focused on increasing the LSPR sensitivity of metal nanostructures. For example, coupling a resonant molecule to the resonance frequency of a nanostructure can increase the magnitude of the nanostructure's LSPR peak shift dramatically.<sup>72</sup> This new technique allows for LSPR detection of a small number of molecules that would not be able to significantly change the surrounding refractive index of the metal nanostructure for appreciable LSPR shifts. Colorimetric detection of enzymatic activity or heavy metal ions can also be performed using LSPR sensing.<sup>73</sup>

### ***1.6.2. Focusing and Concentrating Light with Nanostructures***

Nanostructures that are engineered to focus and manipulate light are often called nanoantennas and are typically nanostructures with sharp features or dimer structures

with engineered sizes and gap widths. The enhanced E-fields near a nanostructure's surface provide a relatively simple route to single-molecule detection<sup>74</sup> and control over the optical properties of molecules.

#### *1.6.2.1 Surface enhanced Raman scattering*

In SERS, the enhanced E-fields of a plasmonic nanostructure can increase the Raman scattering of molecules in their vicinity by a factor of  $E^4$ .<sup>75</sup> Measured enhancements range from  $10^4$  to  $10^{15}$ , and even single molecules have been detected with dimers of nanoparticles and larger aggregates.<sup>76</sup> SERS can directly detect molecule without any label by providing the unique vibrational spectrum of a molecule, a Raman fingerprint. The hot spots (the region with the highest E-field enhancement) within nanoparticles assembly has been used to detect single molecules.<sup>77</sup> More recent applications of SERS include in vivo cancer imaging,<sup>78</sup> mapping pH in living cells<sup>79</sup> and probing intercellular processes.

#### *1.6.2.2. Surface enhanced fluorescence*

The emission of resonant molecules in the vicinity of a plasmonic nanostructure can also be enhanced through a process known as surface enhanced fluorescence (SEF).<sup>80</sup> SEF occurs primarily as a result of the interactions between the excited state of a fluorophore with the near-fields of an excited metal nanostructure, increasing the optical excitation rate and the decay rate (both radiative and nonradiative) for the molecule. Current studies suggest that the fluorophore must be within ~30 nm of the metal nanostructure to benefit from the enhanced near-fields of the nanostructure. However, when a fluorophore is located too close (a few nanometers) to the metal nanoparticle

nonradiative relaxation rates can dominate and quenching arises. Both enhancement and quenching can be utilized for molecular detection and different biological processes.<sup>81</sup>

### 1.6.2.3. Control of Light with Plasmonic Antennas

Plasmonic antennas, like radio antennas, can collect electromagnetic waves and transmit them, at optical frequencies; to a desired place in nanometer scale.<sup>82</sup> Plasmonic nanostructures can also control emission from hybrid structures consisting of both

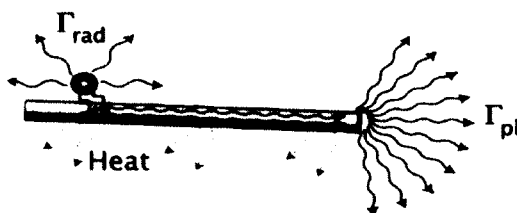


Figure 1.6. Transmission of EM wave from a quantum dot (QD) to distal place through Ag nanowire.  $\Gamma_{\text{rad}}$  and  $\Gamma_{\text{pl}}$  are the emission rates into free space or guided plasmon modes, respectively. Reproduced with permission from ref 83.

semiconductor emitters and metal nanostructures.<sup>83</sup> Energy transfer from a QD to a plasmonic structure can also result in highly coherent PSP modes (with single frequencies). As demonstrated in figure 1.6a, CdSe QD couples with an Ag nanowire to generate a single PSP mode at an optical frequency. The plasmon-exciton conversion was nearly 50%, and a single PSP mode was generated from an optically excited QD, which was then emitted at the distal end of the nanowire. Such plasmon-exciton interaction can have potential applications in lasers,<sup>10</sup> plasmonic transistors,<sup>84</sup> and quantum computing.<sup>7</sup>

### 1.6.3. Plasmonic Circuitry

Integrating optical and electronic circuits could make it possible to greatly increase the speed and reduce the size of microprocessors.<sup>50</sup> Currently, integration of optical interconnects into electronic circuits is not feasible due to the large size of optical

components (1000x larger than electronic components). However, plasmonic nanostructures can carry optical signals at sizes comparable to those of the state-of-the-art transistors (<50 nm). Plasmonic circuits can also route electric currents, which may be useful in some applications. Metal nanostructures that support PSPs are ideal for plasmonic circuitry. Unlike metal thin films, nanostructures inherently guide at scales below optical wavelengths<sup>85</sup> and are well-suited for integration (i.e., coupling) with other components. The main challenges in the use of chemically synthesized nanostructures are the difficulty in controlling their locations on a chip with accuracy at the nanometer scale and the dissipative losses of the PSPs.

#### **1.6.4. Optical Fiber Probes**

By integrating plasmonic nanoparticles with optical fibers, it may be possible to carry out LSPR sensing in very small volumes, remotely, and even in vivo. Several configurations of such fiber-based LSPR sensor were demonstrated. One of the configurations consisted of gold nanospheres adsorbed to the end of the fiber<sup>86</sup> which exhibited LSPR in the reflectance spectrum measured by the fiber. Using this device bulk refractive index sensing, nickel ion sensing, and sensing of biotin-streptavidin binding were performed. Another configuration consisted of a long-period fiber grating (LPFG), in which a segment of the optical cladding was removed and gold nanospheres were deposited on the fiber.<sup>87</sup> In this case, due to the coupling of the LSPR-associated evanescent mode of the particles with the optical modes of the fiber, there was a refractive-index sensitive dip in the fiber transmission at IR wavelengths. This device was demonstrated to have high refractive index sensitivity in terms of the transmission minimum wavelength and the intensity. However, integration of nanostructures on curved

surfaces like fiber is challenging and the plasmonics based fiber optics sensors are still developing.

### 1.7. Emerging applications of plasmonic nanostructures

Although the ability of plasmonic nanostructures to concentrate and direct light has already made them powerful materials for the applications discussed above, new applications are emerging in a broad range of areas. Some of them are discussed below.

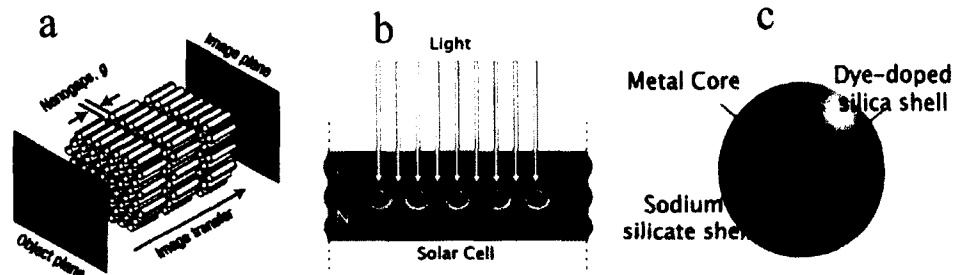


Figure 1.7. Designs of next generation plasmonic devices: superlens (a), plasmonic solar cell (b) and SPASER (c). Reproduced with permission from ref 8, 10 and 89.

Plasmonic nanostructures have been thought to be a promising candidate to fabricate superlenses, which can create images of structures below optical wavelengths ( $\sim 60$  nm).<sup>88</sup> In a superlens, evanescent waves are enhanced with surface plasmons and gain magnification to produce images of sub-wavelength features. Figure 1.7.a shows the design of a typical superlens consisting of silver nanorods.<sup>89</sup> This new design, when implemented may allow for imaging below optical wavelengths in configurations consistent with current microscopy.

One of the primary challenges in photovoltaic cells is to efficiently harvest light energy across the solar spectrum. For this reason, implementing light-harvesting plasmonic nanostructures at specific locations to trap more light and/or localize it for the

optimal generation of electrical energy is an interesting and important area of research.<sup>8</sup> In one approach (Figure 1.7.b) metal nanoparticles can be used as sub-wavelength antennas, where the near-fields of the nanoparticles is coupled to the semiconductor layer, generating electron-hole pairs and increasing the absorption cross section.

Another potential application of plasmonics deals with the creation of tiny lasers based on metal nanoparticles and a gain medium. The nano-plasmonic equivalent to conventional lasers is the surface plasmon amplification by stimulated emission of radiation (SPASER). In a SPASER, the LSPR modes provide the feedback needed for stimulated emission of dye molecules in the presence of metal nanoparticles. The SPASER can actively generate coherent LSPRs when excited through a gain medium. Figure 1.7.c shows a recent example based on Au nanoparticle inside a dye-doped silica shell. Pumping at 488 nm resulted in stimulated emission from the nanoparticle at 530 nm. A SPASER can excite a single LSPR mode in a nanoparticle, something nearly impossible with external optical fields, and the LSPR emission could be tuned to nearly any wavelength (below optical wavelengths), ideal for photolithography below the diffraction limit.<sup>9</sup>

The exciting field of plasmonics and its promising applications in nanotechnology promoted us to direct our research on exploring the plasmonic properties of metal nanostructures and their 2D assemblies.

### **1.8. Rationale and Objectives of the thesis**

Fabrication of ultrasensitive SERS substrates requires huge enhancement of electromagnetic field within the metal nanostructures. Metal nanostructures with sharp edges and corners as well as nanoscale interparticles gaps in their 2D assemblies are known to generate giant electromagnetic field which is termed as “hot spots”. Engineering hot spots in SERS substrate is essential for single molecular SERS detection. Tailoring nanoscale interparticles gaps in solid supported assembly of nanostructures is a challenging task in nanotechnology. Silver nanocubes are capable of producing hot spots due to their sharp edges and corners. Their geometrical shape is convenient for assembling them on solid support with nanoscale interparticles gaps. Therefore this thesis work primarily focuses on fabrication of 2D assembly of silver nanocubes with controlled nanoscale interparticles gaps and studying their optical field enhancing properties with an aim to engineer novel SERS substrates.

Refractive index change-based plasmonic sensor requires improved sensitivity in order to improve the detection limit. Refractive index sensitivity (RIS) and figure of merit (FOM) are two key parameters that determine the sensing capability of plasmonic nanostructures. Often supported assembly of plasmonic nanostructures is preferred over suspended one in plasmonic sensor due to reproducibility, controlled assembly as well as new plasmonic properties arising from the interaction of support and the nanostructures. Therefore, this thesis work is directed to optimize the plasmonic properties of supported 2D assemblies of silver nanocubes to improve their RIS and FOM with an ambition to develop novel plasmonic sensors.

Patterning solid substrates with plasmonic nanostructures is always demanding in nanotechnology due to their multidimensional applications such as in microfluidic devices, plasmonic circuits etc. However, patterned substrates may have new plasmonic properties that can find application in plasmonics. Lithography is a widely used technique for pattern formation on solid substrates. But this technique is sophisticated and tedious. Therefore, this thesis work also aims to fabricate nanotechnologically important patterns of plasmonic nanostructures on solid surfaces in an easy and cost effective way.

### **1.9. Thesis Overview**

This thesis report is divided into seven chapters. In chapter 1, a general introduction to plasmonics has been discussed. This chapter, in context of literature, focuses on fundamentals of plasmonics, properties and some exciting applications of plasmonic materials, and the challenges associated with this growing field which will help reader to follow the objectives of this thesis report.

Chapter 2 describes (i) methods of chemical synthesis of nanostructures, (ii) techniques for assembling nanostructures on solid support and (iii) techniques for characterizing morphology and plasmonic properties of nanostructures and their 2D assemblies.

Chapter 3 demonstrates the fabrication and optical field enhancing effects (SERS and SEF) of self-assembled monolayer of spherical silver nanoparticles. Distance dependent enhancement of SERS and SEF are discussed to reveal the EM mechanism of enhancement of these optical phenomena. These methods and techniques were employed in this thesis work.

Chapter 4 demonstrates the fabrication of 2D assembly of silver nanocubes with controlled nanoscale interparticle gaps to engineer effective SERS substrates by exploiting phospholipids phase behavior.

Chapter 5 demonstrates the optimization of refractive index sensitivity and figure of merit of supported 2D monolayer of silver nanocubes. For improving RIS and FOM of supported silver NCs, effect of different optimization parameters such as RI of solid support, angle of incident light, size and shape of nanostructures are discussed in this chapter.

Chapter 6 demonstrates an easy and cost effective way to pattern solid surfaces with silver nanocubes using phase separated lipid mixtures in Langmuir films.

Chapter 7 presents the overall conclusion derived from this thesis work and recommends some ideas for future work.

## 2.0. References

1. Fletcher, B. “*A History of Architecture on the Comparative Method*” New York, **1905**.
2. Faraday, M. *Philos. Trans. R. Soc. London* **1857**, 147, 145.
3. Mie, G. *Ann. Phys.* **1908**, 25, 377.
4. Maier, S. “*Plasmonics: Fundamentals and Applications*” *Springer*: New York, **2007**.
5. Fang, N.; Lee, H.; Zhang, X. *Science* **2005**, 308, 534.
6. Shalaev, V. M. *Nat. Photonics* **2007**, 1, 41.
7. Chang, D. E.; Sorensen, A. S.; Hemmer, P. R.; Lukin, M. D. *Phys. Rev. Lett.* **2006**, 97, 053002.
8. Chang, D. E.; Sorensen, A. S.; Demler, E. A.; Lukin, M. D. *Nat. Phys.* **2007**, 3, 807.
9. Atwater, H. A.; Polman, A. *Nat. Mater.* **2010**, 9, 205.
10. Haes, A. J.; VanDuyne, R. P. *Anal. Bioanal. Chem.* **2004**, 379, 920.
11. Haes, A. J.; VanDuyne, R. P. *Anal. Bioanal. Chem.* **2004**, 379, 920.
12. Gramotnev, D. K.; Bozhevolnyi, S. I. *Nat. Photonics* **2010**, 4, 83.
13. Maier, S.A. “*Plasmonics: fundamentals and applications*” New York: Springer, **2006**.
14. Mulvaney, P. *Langmuir* **1996**, 12, 788.
15. Wang, F. and Shen, Y.R. *Phys. Rev. Lett.*, **2006**, 97, 206806–14.
16. Lal, S.; Link, S.; Halas, N. J. *Nat. Photonics* **2007**, 1, 641.
17. Link, S.; El-Sayed, M A. *J. Phys. Chem. B* **1999**, 103, 8410.

18. Cao, W.; Elsayed-Ali, H. E. *Mater. Lett.* **2009**, *63*, 2263.
19. Ru, E. L.; Etchegoin, P. "Principles of Surface Enhanced Raman Spectroscopy"  
Elsevier: Oxford, U.K., **2009**.
20. Elechiguerra, J. L.; Larios-Lopez, L.; Liu, C.; Garcia-Gutierrez, D.; Camacho-Bragado, A.; Yacaman, M. *J. Chem. Mater.* **2005**, *17*, 6042.
21. Cao, W.; Elsayed-Ali, H. E. *Mater. Lett.* **2009**, *63*, 2263.
22. Yoon, I.; Kang, T.; Choi, W.; Kim, J.; Yoo, Y.; Joo, S.-W.; Park, Q.-H.; Ihee, H.; Kim, B. *J. Am. Chem. Soc.* **2009**, *131*, 758.
23. Frederix, F.; Friedt, J.-M.; Choi, K.-H.; Laureyn, W.; Campitelli, A.; Mondelaers, D.; Maes, G.; Borghs, G. *Anal. Chem.* **2003**, *75*, 6894.
24. Lee, K.-S.; El-Sayed, M. A. *J. Phys. Chem. B* **2006**, *110*, 19220.
25. Yoon, I.; Kang, T.; Choi, W.; Kim, J.; Yoo, Y.; Joo, S.-W.; Park, Q.-H.; Ihee, H.; Kim, B. *J. Am. Chem. Soc.* **2009**, *131*, 758.
26. Rycenga, M.; Hou, K. K.; Cobley, C. M.; Schwartz, A.; Camargo, P. H. C.; Xia, Y. *Phys. Chem. Chem. Phys.* **2009**, *11*, 5903.
27. Schnell, M.; Garcia-Etxarri, A.; Huber, A. J.; Crozier, K. B.; Borisov, A.; Aizpurua, J.; Hillenbrand, R. *J. Phys. Chem. C* **2010**, *114*, 7341.
28. Tcherniak, A.; Ha, J. W.; Dominguez-Medina, S.; Slaughter, L. S.; Link, S. *Nano Lett.* **2010**, *10*, 1398.
29. Schnell, M.; Garcia-Etxarri, A.; Huber, A. J.; Crozier, K. B.; Borisov, A.; Aizpurua, J.; Hillenbrand, R. *J. Phys. Chem. C* **2010**, *114*, 7341.
30. Munechika, K.; Smith, J. M.; Chen, Y. and David S. Ginger, D. G. *J. Phys. Chem. C* **2007**, *111*, 18906.

31. Cubukcu, E.; Degirmenci, F.; Kocabas, C.; Zimmler, M. A.; Rogers, J. A.; Capasso, F. *Proc. Natl. Acad. Sci. U.S.A.* **2009**, *106*, 2495.
32. Billaud, P.; Marhaba, S.; Grillet, N.; Cottancin, E.; Bonnet, C.; Lerme, J.; Vialle, J.-L.; Broyer, M.; Pellarin, M. *Rev. Sci. Instrum.* **2010**, *81*, 043101.
33. Chang, W.-S.; Ha, J. W.; Slaughter, L. S.; Link, S. *Proc. Natl. Acad. Sci. U.S.A.* **2010**, *107*, 2781.
34. Cubukcu, E.; Degirmenci, F.; Kocabas, C.; Zimmler, M. A.; Rogers, J. A.; Capasso, F. *Proc. Natl. Acad. Sci. U.S.A.* **2009**, *106*, 2495.
35. Nelayah, J.; Kociak, M.; Stephan, O.; de Abajo, F. J. G.; Tence, M.; Henrard, L.; Taverna, D.; Pastoriza-Santos, I.; Liz-Marzan, L. M.; Colliex, C. *Nat. Phys.* **2007**, *3*, 348.
36. Ianoul, A.; Strelak, N. and Maskevich, S. *J. Nanosc. Nanotech.* **2006**, *6*, 61.
37. Davis, T. J.; Gomez, D. E.; Vernon, K. C. *J. Appl. Phys.* **2010**, *106*, 043502.
38. Wu, Y.; Nordlander, P. *J. Phys. Chem. C* **2010**, *114*, 77302.
39. Pinchuk, A.; Hilger, A.; von Plessen, G.; Kreibig, U. *Nanotechnology* **2004**, *15*, 1890.
40. Prodan, E.; Radloff, C.; Halas, N. J.; Nordlander, P. *Science* **2003**, *302*, 419.
41. Brown, L. V.; Sobhani, H.; Lassiter, J. B.; Nordlander, P.; Halas, N. J. *ACS Nano* **2010**, *4*, 819.
42. Wang, L.; Wu, H.-I. *Biomedical Optics: Principles and Imaging*; John Wiley and Sons, Inc: New York, **2007**.
43. Yang, W.-H.; Schatz, G. C.; Duynes, R. P. V. *J. Chem. Phys.* **1995**, *103*, 869.
44. Yee, K. *IEEE Trans. Antennas Propag.* **1966**, *14*, 302.

45. Jin, J. *The Finite Element Method in Electromagnetics*; *John Wiley and Sons, Inc: New York*, **2002**.
46. Wiley, B. J.; Im, S. H.; Li, Z.-Y.; McLellan, J.; Siekkinen, A.; Xia, Y. *J. Phys. Chem. B* **2006**, *110*, 15666.
47. Wiley, B.; Chen, Y.; McLellan, J.; Xiong, Y.; Li, Z.-Y.; Ginger, D.; Xia, Y. *Nano Lett.* **2007**, *7*, 1032.
48. Mulvihill, M. J.; Ling, X. Y.; Henzie, J.; Yang, P. *J. Am. Chem. Soc.* **2010**, *132*, 268.
49. Hutter, E.; Fendler, J. H. *Adv. Mater.* **2004**, *16*, 1685.
50. Kelly, K.; Coronado, E.; Zhao, L.; Schatz, G. *J. Phys. Chem. B* **2003**, *107*, 668.
51. Ditlbacher, H.; Hohenau, A.; Wagner, D.; Kreibig, U.; Rogers, M.; Hofer, F.; Aussenegg, F. R.; Krenn, J. R. *Phys. Rev. Lett.* **2005**, *95*, 257403.
52. Gramotnev, D. K.; Bozhevolnyi, S. I. *Nat. Photonics* **2010**, *4*, 83.
53. Ditlbacher, H.; Hohenau, A.; Wagner, D.; Kreibig, U.; Rogers, M.; Hofer, F.; Aussenegg, F. R.; Krenn, J. R. *Phys. Rev. Lett.* **2005**, *95*, 257403.
54. Hartland, G. V. *Nat. Mater.* **2007**, *6*, 716.
55. McLellan, J. M.; Siekkinen, A.; Chen, J.; Xia, Y. *Chem. Phys. Lett.* **2006**, *147*, 122.
56. Moskovits, M.; Srnova-Sloufova, I.; Vlckova, B. *J. Chem. Phys.* **2002**, *116*, 10435.
57. Skrabalak, S. E.; Chen, J.; Sun, Y.; Lu, X.; Au, L.; Cobley, C. M.; Xia, Y. *Acc. Chem. Res.* **2008**, *41*, 1587.
58. Song, K. H.; Kim, C.; Cobley, C. M.; Xia, Y.; Wang, L. V. *Nano Lett.* **2008**, *9*, 183.
59. Chen, J.; Glaus, C.; Laforest, R.; Zhang, Q.; Yang, M.; Gidding, M.; Welch, M. J.; Xia, Y. *Small* **2010**, *6*, 811.

60. Yavuz, M. S.; Cheng, Y.; Chen, J.; Cobley, C. M.; Zhang, Q.; Rycenga, M.; Xie, J.; Kim, C.; Song, K. H.; Schwartz, A. G.; Wang, L. V.; Xia, Y. *Nat. Mater.* **2009**, *8*, 935.
61. Rycenga, M.; Cobley, C.M.; Zeng, J.; Li, W, Moran, C.H.; Zhang, Q.; Qin, D.and Xia, Y. *Chem. Rev.* **2011**, *111*, 3669.
62. Prodan, E.; Radloff, C.; Halas, N. J.; Nordlander, P. *Science* **2003**, *302*, 419.
63. Evans, P. R.; Kulloock, R.; Hendren, W. R.; Atkinson, R.; Pollard, R. J.; Eng, L. M. *Adv. Funct. Mater.* **2008**, *18*, 1075.
64. Decher, G. *Science* **1997**, *277*, 1232.
65. Halliwell, C.M. and Cass, A.E.G. *Anal. Chem.* **2001**, *73*, 2476.
66. P. Yang, F. Kim, *ChemPhysChem* **2002**, *3*, 503.
67. Sherry, L.; Chang, S.-H.; Schatz, G.; Van Duyne, R.; Wiley, B.; Xia, Y. *Nano Lett.* **2005**, *5*, 2034.
68. Zhang, S.; Bao, K.; Halas, N.J.; Xu, H. and Nordlander, P. *Nano Lett.* **2011**, *11*, 1657.
69. Leveque, G.; Martin, O. J. F. *Opt. Express* **2006**, *14*, 9971.
70. Mock, J. J.; Hill, R. T.; Degiron, A.; Zauscher, S.; Chilkoti, A.; Smith, D. R. *Nano Lett.* **2008**, *8*, 2245.
71. Underwood, S.; Mulvaney, P. *Langmuir* **1994**, *10*, 3427.
72. Zheng, Y. B.; Yang, Y.-W.; Jensen, L.; Fang, L.; Juluri, B. K.; Flood, A. H.; Weiss, P. S.; Stoddart, J. F.; Huang, T. J. *Nano Lett.* **2009**, *9*, 819.
73. Choi, Y.; Ho, N.-H.; Tung, C.-H. *Angew. Chem., Int. Ed.* **2007**, *46*, 707.
74. Le, R. E.; Meyer, M.; Etchegoin, P. *J. Phys. Chem. B* **2006**, *110*, 1944.

75. Le, R. E. C.; Etchegoin, P. G. *Chem. Phys. Lett.* **2006**, *423*, 63.
76. Blackie, E. J.; Ru, E. C. L.; Etchegoin, P. G. *J. Am. Chem. Soc.* **2009**, *131*, 14466.
77. Fang, Y.; Seong, N.-H.; Dlott, D. D. *Science* **2008**, *321*, 388.
78. Qian, X.; Peng, X.-H.; Ansari, D. O.; Yin-Goen, Q.; Chen, G. Z.; Shin, D. M.; Yang, L.; Young, A. N.; Wang, M. D.; Nie, S. *Nat. Biotechnol.* **2008**, *26*, 83.
79. Kneipp, J.; Kneipp, H.; Wittig, B.; Kneipp, K. *J. Phys. Chem. C* **2010**, *114*, 7421.
80. Shang, L.; Chen, H.; Dong, S. *J. Phys. Chem. C* **2007**, *111*, 10780.
81. Kuhn, S.; Hakanson, U.; Rogobete, L.; Sandoghdar, V. *Phys. Rev. Lett.* **2006**, *97*, 017402.
82. Akimov, A. V.; Mukherjee, A.; Yu, C. L.; Chang, D. E.; Zibrov, A. S.; Hemmer, P. R.; Park, H.; Lukin, M. D. *Nature* **2007**, *450*, 402.
83. Lee, J.; Govorov, A. O.; Kotov, N. A. *Angew. Chem., Int. Ed.* **2005**, *44*, 7439.
84. Tominaga, J.; Mihalcea, C.; Buchel, D.; Fukuda, H.; Nakano, T.; Atoda, N.; Fuji, H.; Kikukawa, T. *Appl. Phys. Lett.* **2001**, *78*, 2417.
85. Economou, E. N. *Phys. Rev.* **1969**, *182*, 539.
86. Cheng, S. F.; Chau, L. K. *Anal. Chem.* **2003**, *75*, 16.
87. Tang, J. L.; Cheng, S. F.; Hsu, W. T.; Chiang, T. Y.; Chau, L. K. *Sens. Actuators, B* **2006**, *119*, 105.
88. Shalaev, V. M. *Science* **2008**, *322*, 384.
89. Kawata, S.; Ono, A.; Verma, P. *Nat. Photonics* **2008**, *2*, 438.

## **Chapter 2**

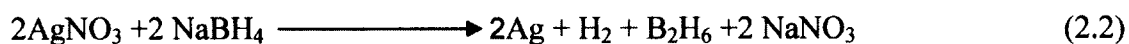
---

### **Materials and Methods**



### **2.1.2 Borohydride reduction**

This method produces monodisperse and smaller (3-15nm) silver nanoparticles (mainly spherical).<sup>4</sup> Since borohydride is a strong reducing agent, the reduction rate is faster than the citrate reduction and does not require high temperature. In this method borohydride serves both as a reducing agent and a stabilizing agent. Silver nanoparticles prepared by this method were used to study the nature of electromagnetic field existing on nanoparticle's surface upon irradiation. In a typical synthesis, aqueous AgNO<sub>3</sub> solution was mixed with ice-chilled aqueous sodium borohydride solution (NaBH<sub>4</sub>) in a 1:3 volume ratio with constant stirring. The resulting silver hydrosols exhibit a yellow color. The equation for the redox reaction can be written as



### **2.1.3. Polyol synthesis method**

The polyol process has gained popularity for achieving tight control over size and shape of silver nanoparticles.<sup>5</sup> By varying the reaction conditions, such as temperature, reagent concentration and presence of trace ions, it has been possible to achieve a high degree of control over both nucleation and growth and thus the final product. In this thesis work polyol method was employed to generate silver nanocubes of different size. In polyol method, a polyalcohol serves as both a solvent and a reducing agent; polyvinylpyrrolidone (PVP) serves as a shape control agent as well as a stabilizer, and silver nitrate acts as silver precursor. In a typical synthesis of silver nanocubes, solutions of PVP and AgNO<sub>3</sub> (in ethylene glycol) are injected simultaneously in a pre-heated (140°C) ethylene glycol (EG) containing a trace amount of HCl.<sup>6</sup> The solution is left for 26 hours under stirring to produce silver nanocubes. The reduction mechanism of EG

revealed that the primary reducing agent is glycoaldehyde which is formed when EG is heated in presence of oxygen. The relevant equations for the reaction are

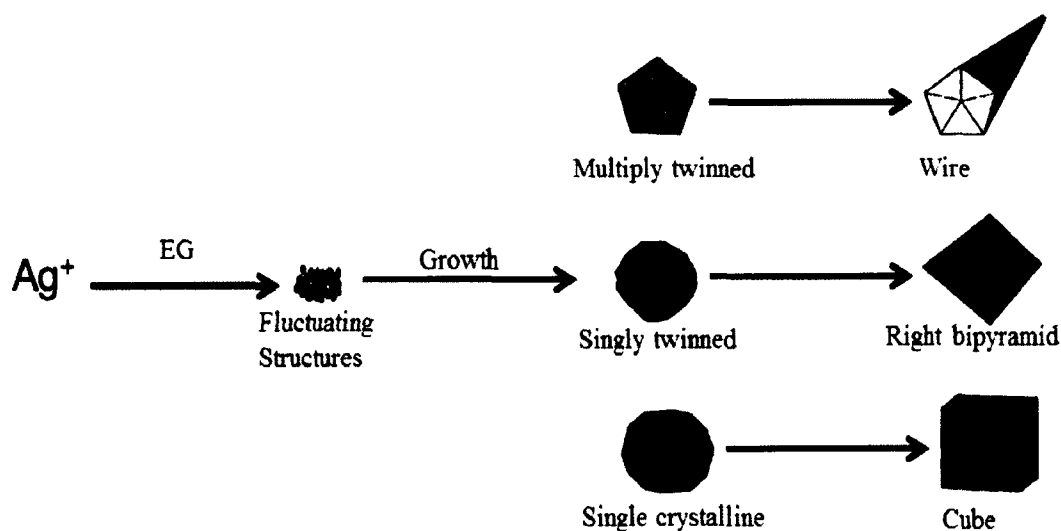


Figure 2.1. Formation process of silver nanocubes and other morphologies in polyol synthesis method. Reproduced with permission from ref 5.

Based on the experimental results, the formation process of silver nanocubes in polyol method has been proposed<sup>5</sup> which is depicted in figure 2.1. It shows that at the initial stage of the reduction process, Ag atoms form small clusters of fluctuating structures. As the silver clusters grow larger, they become stable and emerge to one of the three predominant structures: single crystalline, single twinned and multiply twinned. At this stage, larger clusters of Ag atoms are called seeds from which they will ultimately grow into nanostructures with different shapes. Typically the single crystalline seeds give rise to cuboctahedrons. At this stage of growth PVP preferentially adsorbs on {100} facets of Ag seeds and Ag atoms only deposit on {111} facets eventually giving rise to larger size Ag nanocubes (80-130 nm) enclosed by {100} sides faces. Growth of single -twinned

and multiply- twinned seeds result in the formation of right bipyramids and wires respectively. However, it is possible to force the reaction to proceed along the direction of producing nanocubes by adding appropriate oxidative etchant such as HCl in presence of oxygen. The etchant preferentially prevents the formation of twinned seeds as these seeds associate with defects and produce perfect silver nanocubes with sharp edges. Polyol process, however, is slow as it takes several hours to generate silver nanocubes. Addition of some ions such as sulfide ( $S^{2-}$ ) or hydrosulfide ( $HS^-$ ) has been shown to dramatically increase the reduction rate of  $AgNO_3$  in the polyol system, making large-scale production of Ag nanocubes within few minutes.<sup>7</sup> In this case,  $Ag_2S$  nanocrystallites are thought to form immediately upon the introduction of  $AgNO_3$  which can then serve as both catalyst and seeds for further growth in a polyol synthesis. This modified -polyol method was used to synthesis smaller nanocubes (40-50 nm).

## **2.2. Techniques for 2D assembly of metal nanostructures**

### ***2.2.1 Langmuir-Blodgett Technique***

The Langmuir-Blodgett (LB) technique, first introduced by Irving Langmuir and applied extensively by Katharine Blodgett, involves deposition of fluid supported monolayer onto solid support.<sup>7-9</sup> Originally this technique was developed for studying various physiochemical properties for different fatty acids in a monolayer, supported by a water sub-phase, which is called Langmuir monolayer. Later, it was found that the water supported film can be transferred onto solid substrates and the resultant solid supported film is referred to as Langmuir-Blodgett film.<sup>10</sup> However, this technique nowadays became a powerful tool to make thin film on solid substrates of both organic and inorganic materials of scientific and technological interest.<sup>11,12</sup>

In this study LB technique was employed to fabricate monolayer of metal nanostructures on solid substrates.

### *2.2.1.1. Theoretical background*

Amphiphilic molecules such as fatty acids can spread and orient themselves at air-water interface to minimize their free energy.<sup>13</sup> The resulting two-dimensional surface film is one molecule in thickness and is commonly called a monolayer. The molecules of most monolayer-forming materials are composed of two parts: one that by itself would mix with water (hydrophilic part) and another that by itself would not (hydrophobic). These molecules are amphiphiles, the most important types of which are soaps and phospholipids. The presence of a monolayer film on a liquid surface affects the surface tension of the pure liquid.<sup>13</sup> In monolayer experiments the effect is traditionally measured as surface pressure,  $\Pi$  which is equal to the reduction in surface tension of a pure liquid by the film, i.e.,  $\Pi = \gamma_0 - \gamma$ ; where  $\gamma_0$  is the surface tension of the pure liquid and  $\gamma$  is the surface tension of the film-covered liquid surface. During the compression, the number of molecules per unit area and relative molecular orientation are changed which alter the surface pressure of the film. However, as the monolayer is compressed on the water surface, it may undergo several phase transformations. These phases are analogous to the three dimensional gases, liquids and solids.<sup>14</sup> In Langmuir film, a gas phase is a state of molecules where the molecules are far apart from each other that the mutual interaction is negligible, in a liquid phase the molecules interact each other by their random hydrocarbon chains and in solid phase the hydrocarbon chain pointing in the same direction away from the water and the average molecular area is the same as the cross section of the molecule and the molecular interaction is highest. However, in

case of phospholipids an additional phase appears with liquid phase due to the presence of double hydrocarbon chains. A liquid expanded phase (LE) where the hydrocarbon chains are random in direction and a liquid condensed phase (LC) where the hydrocarbon chains are pointing the same direction.<sup>13</sup> The phase changes may be readily identified by monitoring the surface pressure ( $\Pi$ ) as a function of the area occupied by the film. In LB experiment such a plot is called surface pressure-area isotherm.<sup>13</sup> From this isotherm, the area occupied by a single molecule,  $a$ , can be obtained by dividing the film area,  $A$  by the total number of molecules on the water surface i.e.

$$a = (AM/CN_A V) = (A/cN_A V) \quad 2.5$$

Where  $M$  is the molecular weight of the monolayer material,  $C$  is the concentration of the spreading solution in mass per unit volume,  $c$  is the specific molar concentration of the solution and  $V$  is its volume. However, hydrophobically capped metal nanoparticles (NPs) can also be spreaded at air-water interface to make monolayer. Such monolayer during compression exhibits similar phase behaviors as those of amphiphiles. However, for metal nanoparticles monolayer, it is customary to monitor surface pressure as a function of absolute area occupied by the film instead of mean molecular area. Such a plot is shown in figure 2.2 (left) along with the different phases that a monolayer may undergo. In gas phase the NPs stay apart from each other such that surface density is low and therefore surface pressure does not change. In liquid phase, the NPs come close enough for mutual interaction to take place increasing the particle density which in turn increases the surface pressure. In solid phase, the NPs form close packing structure giving a sharp increase in surface pressure and after a critical surface pressure (collapse pressure) further compression results in multilayer formation. However, in case of NPs

with anisotropic geometry like nanocubes, liquid phase encompasses two sub-phases: a liquid extended (LE) phase where the NCs are close to each other but are in random orientations and liquid condensed (LC) phase where the NCs are orientated in a particular direction.

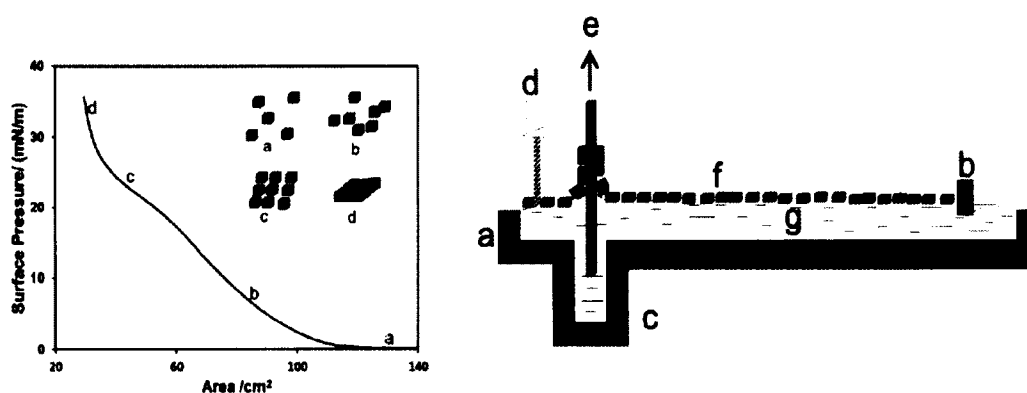


Figure 2.2. Typical pressure -area isotherm of a silver nanocubes monolayer (left). During the compression, the monolayer undergoes different phases i.e.; (a) gas phase, (b) liquid extended phase, (c) liquid condensed phase and (d) solid phase. Organizations of constituent nanostructures in different phases (inset). A cross section of LB trough (right) showing (a) trough boundary, (b) single barrier, (c) well for film deposition, (d) surface pressure sensor, (e) upward-pulling substrate, (f) a Langmuir monolayer of silver nanocubes and (g) water sub-phase.

#### 2.2.1.2. Instrumentation

Langmuir-Blodgett trough that was used in our research projects was NIMA 611, Coventry, UK. The different components of this technique are depicted in figure 2.2 (right).

#### *Trough*

The first requirement for deposition of LB film is a sub-phase (g) container called Langmuir or Langmuir-Blodgett trough. The NIMA Model 611 trough that was used is a rectangular shape one barrier trough (a). The trough material is Teflon because of its hydrophobic nature and chemical inertness. To compress or expand the monolayer, a

Teflon made barrier (b) is moved via a suitable gearing system to an electric motor. There is a well (c) at the end of the trough to allow the deposition of NPs monolayer (f) on the substrate (e).

#### *Pressure sensors*

Measurement of surface pressure is performed by means of a pressure sensor (d). NIMA trough uses a Wilhelmy plate (a small piece of chromatography paper-Whatmans Chr1) as pressure sensors. The plate detects the downward force exerted by the liquid meniscus which wets the plate.

#### *2.2.1.3. Preparation and deposition of LB monolayer*

The trough is first cleaned with chloroform and then MilliQ water. Before starting any experiment the pressure sensor is recommended to calibrate using calibration weight. Once calibration is done, the Wilhelmy plate is suspended and the trough is filled up with MilliQ water so that the sensor plate gets wet. The trough is left for a few minutes to achieve the equilibrium surface tension read by the sensor. To prepare the Langmuir monolayer, the nanoparticle has to be free from impurity (unreacted reactants from synthesis) otherwise defects appear in the monolayer. The cleaned colloidal hydrophobic nanoparticles (surface PVP are suspended in chloroform. Using a micro syringe pipette, few hundreds microliters of colloidal NPs are injected on the sub-phase surface if only one substrate is to be prepared, the substrate can be placed in the sub-phase before spreading the solution. For multiple substrates preparation the substrates can be placed once the monolayer is spreaded. However, after the monolayer has been spreaded, the carrier solvent has to be evaporated. After 20 min annealing should be performed at very low surface pressures to get rid of the defects (holes). A typical barrier speed of 20

cm<sup>2</sup>/min can be set up. Before transferring, a complete pressure-area isotherm has to be taken to infer the phase transition pressure of the monolayer. Finally the monolayer is transferred onto the substrate at a desired surface pressure (assembly with desired surface pressure) and transfer velocity (for creating specific pattern) for further analysis.

### ***2.2.2. Self-assembled monolayer technique***

Self-assembly is the most common term in use in the modern scientific community to describe the spontaneous aggregation of particles without the influence of any external forces. In this thesis work, this simple technique was employed to fabricate monolayers of silver and gold nanoparticles on both planar (glass slides) and curved (optical fiber) substrates. In this technique the solid substrate is modified with organic molecules having specific functional groups and the resultant solid supported organic film is immersed into a colloidal solution of charged nanoparticles. The surface coverage of NPs depends on the time of immersion and the concentration of colloidal nanoparticles. Electrostatic interaction between the solid substrate and the nanoparticles is the main driving force for the deposition of NPs on the solid substrates. The organic molecules that were used in this thesis works are polyelectrolytes such as (poly (sodium-4-styrenesulfonate) (PSS) and Poly (diallyldimethylammonium chloride) (PDADMAC)), and 3-aminopropyltrimethoxy-silane (APTMS). For effective deposition of NPs, the substrate has to be cleaned by piranha solution to remove organic molecules from the substrates. However, piranha solution not only cleans the substrate surface but also hydroxylates the silica surface which is a requirement for adhesion of organic layer. For example, adhesion of 3-APTMS on glass takes place by hydrolytic bond formation between exposed hydroxyl sites on the glass and the methoxy groups of APTMS. When amine

terminated SAM of APTMS is submerged into colloidal solution of negatively charged metal nanoparticles, electrostatic interaction immobilized the nanoparticles on the glass (Figure 2.3.a). However, self-assembly via polyelectrolytes requires adhesion of positively charged PDADMAC on negatively charged glass slide and subsequent deposition of negatively charged NPs on the PDADMAC film (Figure 2.3. b).



Figure 2.3. Fabrication of self-assembled monolayers of nanoparticles; silanization approach (a) and polyelectrolytes deposition approach (b).

## 2.3 Technique for analysis of nanostructures morphologies

### 2.3.1 Atomic Force Microscopy

Atomic force microscopy (AFM) is a scanning technique which yields high resolution three-dimensional images of sample surfaces. In AFM, a probe tip is integrated with a micro-fabricated force-sensing cantilever and brought into contact with the surface of the sample. The force acting between the tip and the sample deflects the cantilever. The amount of cantilever's deflection is directly related to the tip-sample interaction and is used as the primary parameter to produce three-dimensional image of sample surface. AFM was first introduced by Binnig et al. in 1985.<sup>15</sup> AFMs can be used to profile any engineering surface whether it is electrically conductive or insulating in ambient liquids, various gas and air. Using AFM, ultra small forces ranging from 10nN to 1 pN have been detected by AFM and topographic images with a vertical resolution of less than 0.1 nm and a lateral resolution of about 0.2 nm have been reported.<sup>16,17</sup> There are a number of

commercial AFMs available in the market such as Nanoscience instruments Inc. (Phoenix, AZ, USA), NTEGRA (Russia), Olympus (Japan). Basic instrumentation of AFM is described in the following paragraph.

### 2.3.1.1 Instrumentation

The AFM is a relatively simple and versatile instrument. The necessary parts are the force measuring cantilever probe, piezo electric scanner connected with control system (feedback loop) for maintaining tip-sample distance, optical deflection system to detect cantilever's movement (shown in figure 2.4).<sup>18</sup>

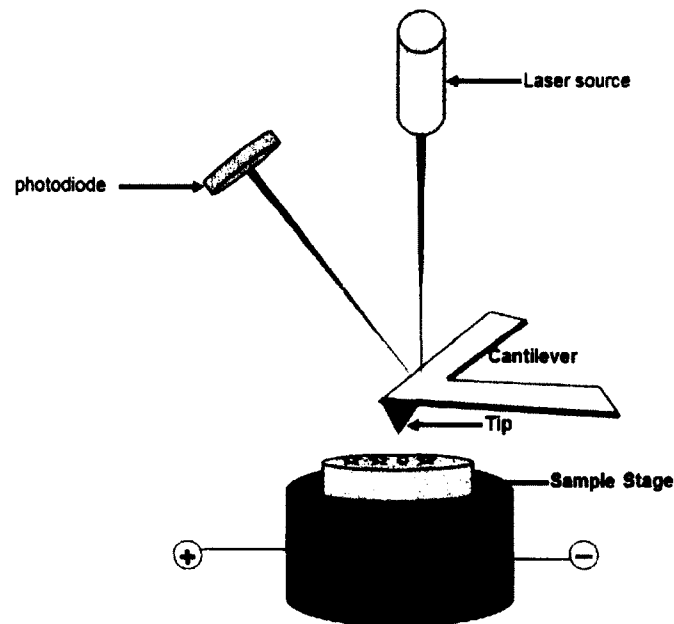


Figure 2.4. Schematic diagram of different components in an atomic force microscope (AFM).

### *Cantilever*

It is an ultra force sensing mechanical resonator usually made of single crystal silicon (Si) and silicon nitride ( $\text{Si}_3\text{N}_4$ ) with micro meter dimension. The cantilever stylus used in the AFM should meet the following criteria: (1) low normal spring constant

(stiffness); (2) high resonant frequency; (3) high cantilever quality factor  $Q$ ; (4) high lateral spring constant (stiffness); (5) short cantilever length; (6) incorporation of components (such as mirror) for deflection sensing and (7) a sharp protruding tip.<sup>5</sup> In order to register a measurable deflection with small forces, cantilever must flex with a relatively low force, requiring a higher spring constants (0.01 -100 N/m) for atomic resolution in contact mode imaging. To avoid thermal and environmental noises, the resonance frequency of the cantilever has to be higher than 10 kHz. A high lateral cantilever spring constant is desirable in order to reduce the effect of lateral forces in the AFM, as frictional forces can cause appreciable lateral bending of the cantilever. Lateral bending results in erroneous topography measurements. A sharp protruding tip must be present at the end of the cantilever to provide a well-defined interaction with the sample over a small area. Therefore, a high aspect ratio of the tip is desired. Additionally the tip should be centered at the free end of the cantilever. Commercially available atomic force microscopy tips, integrated with force sensing cantilevers, are micro-fabricated from silicon and silicon nitride by lithographic and anisotropic etching techniques. The performance of these tips can be characterized by imaging nanometer scale standards of known dimension, and the resolution is found to roughly correspond to the tip radius of curvature, the tip aspect ratio, and the sample height. Although silicon and silicon nitride tips have a somewhat large radius of curvature, low aspect ratio, and limited life time due to wear, the wide spread use of AFM today is due in large part to the broad availability of these tips. In some special cases, small asperities on the tip can provide resolution much higher than the tip radius of curvature for low- $Z$  samples such as crystal surfaces and ordered protein arrays. Several strategies have been developed to improve

AFM tip performance. Oxide sharpening improves tip sharpness and enhances tip asperities. For high-aspect-ratio samples such as integrated circuits, silicon AFM tips can be modified by focused ion beam (FIB) milling. FIB tips reach 3 degree cone angles over lengths of several microns and can be fabricated at arbitrary angles. Others high resolution and high-aspect-ratio tips are produced by electron beam deposition (EBD) in which a carbon spike is deposited onto the tip apex from the background gases in an electron microscope. Finally, carbon nanotubes have been employed as AFM tips. Their nanometer scale diameter, long length, high stiffness, and elastic buckling properties make carbon nanotubes possibly the ultimate tip material for AFM.

#### *Scanning and Control system*

The most challenging task in AFM is the nano-scale positioning of the sample from the tip during scanning. This task was solved by using a piezo-electric tube scanner. An electric field applied across a piezoelectric material causes a change in the crystal structure, with expansion in some directions and contraction in others. As a result a net volume change occurs. The piezo ceramic is molded into a tube form. The outer electrode is separated into four segments and connected to the scanning voltage. The z-voltage is applied to the inner electrode. The control system consists of electronics and software and comprises a feedback loop. The signal from the transducer is fed into the feed back loop which consist mainly a subtraction stage to get an error signal and an integrator. The error signal is sent to the piezo tube to maintain the tip- sample distance.

#### *Detection systems for cantilever deflections*

The most common cantilever deflection detection system is the optical lever. In this technique a fairly well collimated light beam is reflected off a mirror and projected to a

receiving target. Any change in the angular position of the mirror will change the position where the light ray hits the target. In an AFM using the optical lever method, a photodiode segmented into four closely spaced devices detects the orientation of the end of the cantilever. Initially the light ray is set to hit the photodiodes in the middle of the two sub-diodes. Any deflection of the cantilever will cause an imbalance of the number of photons reaching the two halves. Hence the electrical currents in the photodiodes will be unbalanced too. The difference signal is further amplified and is the input signal to the feedback loop.

#### *2.3.1.2 Operation modes of AFM*

The AFM operates in two basic modes which are the static mode and the dynamic mode. In static mode of operation, also known as repulsive or contact mode, a sharp tip at the end of the cantilever is brought into contact with the surface of the sample. The cantilever is "dragged" across the surface of the sample and the contours of the surface are measured directly using the deflection of the cantilever. During initial contact, the atoms at the end of the tip experience a very weak repulsive force due to electronic orbital overlap with the atoms in the surface measured by optical detector. A piezoelectric scanner scans the sample (under the tip) while the forces are measured through the deflections of the cantilever. To achieve more controlled imaging conditions of the samples, a feedback loop monitors the tip-sample force and adjusts the sample Z-position to hold the force constant. The topographic image of the sample is then taken from the sample Z-position data. This mode of operation is generally used for flat samples that can withstand lateral forces during scanning. However, contact mode of operation associates with contamination of tip and damage of sample surface after taking several scans. Such

issues can be by passed by using dynamic mode of operation where the cantilever is externally oscillated at or close to its fundamental resonance frequency. The oscillation amplitude, phase and resonance frequency are modified by tip-sample interaction forces. These changes in oscillation with respect to the external reference oscillation provide information about the sample's characteristics. Based on the feedback parameter dynamic mode is operated in two basic methods: amplitude- modulation operation, where the amplitude of the cantilever is used as feedback signal while frequency is kept a constant value and frequency modulation mode operation, where frequency is used as feedback signal while amplitude is kept a constant value. However, dynamic mode of operation is further subdivided into noncontact and tapping (semi-contact) modes. In noncontact mode, the tip of the cantilever does not contact the sample surface. The cantilever is instead oscillated at a frequency slightly above its resonant frequency where the amplitude of oscillation is typically a few nanometers ( $<10$  nm). The van der Waals forces, which are strongest from 1 to 10 nm above the surface, or any other long range force which extends above the surface acts to decrease the resonance frequency of the cantilever. This decrease in resonant frequency combined with the feedback loop system maintains a constant oscillation amplitude or frequency by adjusting the average tip-to-sample distance. Measuring the tip-to-sample distance at each (x,y) data point allows the scanning software to construct a topographic image of the sample surface. However, imaging viscous- samples such as polymers and biological samples in ambient conditions by the non-contact mode of operation results in sticking of the probe tip to the sample surface.<sup>20</sup> This may cause tip damage or contamination. These issues can be bypassed by using tapping or semi-contact mode of operation where the cantilever is driven to

oscillate up and down at near its resonance frequency by a small piezoelectric element mounted in the AFM tip holder similar to non-contact mode. However, the amplitude of this oscillation is greater than 10 nm, typically 100 to 200 nm.<sup>18</sup> The tip gets close to the surface during each cycle of oscillation and amplitude of oscillation is decreased due to the surface forces. The amplitude is used as feedback to maintain a constant height of the tip from the sample surface. A tapping mode AFM image is produced by imaging the force of the intermittent contacts of the tip with the sample surface.

## **2.4. Spectroscopic analysis**

### ***2.4.1. Raman Spectroscopy***

Raman spectroscopy is a spectroscopic technique based on Raman scattering effect used to study vibrational, rotational and other low-frequency modes in a molecule which provide molecular information.<sup>1</sup> Raman scattering was first documented by C.V. Raman in 1928.<sup>2</sup> However, the phenomenon was also observed by G. Landsberg and L. Mandelstam.<sup>2</sup> Raman received the Nobel Prize in 1930 for his work on the scattering of light.<sup>1</sup>

Scattering refers to light deflected from the direction of incident-light propagation upon interaction with electrons in molecules. In absorption or fluorescence, the molecule is excited to a discrete energy level but in scattering, the molecule is excited to an unstable energy level which is called virtual state.<sup>1</sup> In other word, the energy of the scattered light is less than the difference between the energy levels of the molecule which is depicted in figure 2.5. The scattered light may have the same or different frequency as the incident light and accordingly scattering are classified into two categories i.e.;

Rayleigh scattering and Raman scattering. In Rayleigh scattering (elastic scattering) the scattered light has the same frequency as that of incident light.

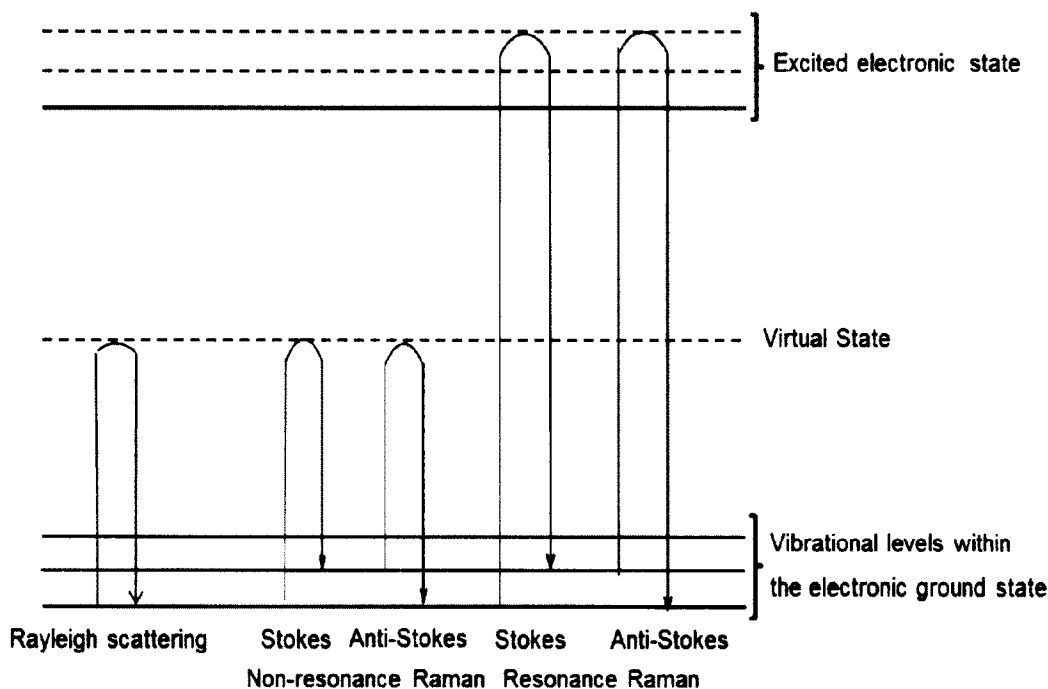


Figure 2.5. Schematic illustration of Stokes and anti-Stokes Raman effects in both non-resonance and resonance Raman scatterings.

In Raman scattering, the scattered light can have either a lower frequency, for which the effect is called Stokes Raman scattering or higher frequency in which case the effect is termed as anti-Stokes effect of Raman scattering. When photons interact with a molecule, some of their energy can be converted into various modes of vibrations of the molecules. In Stokes effect, the incident light loses energy to cause molecular vibration and the scattered light has lower frequency than the incident light. On the contrary, anti-Stokes effect involves transfer of energy from the molecules, already in excited vibrational state, to the incident light and therefore the scattered light possesses higher

frequency than the incident light. The intensities of the Stokes and anti-Stokes lines are governed largely by the Boltzmann populations of the vibrational states involved in the transition. It follows that anti-Stokes lines are usually weak because initially very few molecules are in an excited vibrational state and their (anti-Stokes) intensities increase with increasing the temperature.<sup>1</sup> However, the difference between the incident-light frequency and the scattered frequency in Stokes and anti-Stokes scattering is identical. Usually, intensity of Raman scattering is much weaker than the intensity of Rayleigh scattering (only  $10^{-6}$  of the intensity of the Rayleigh line).<sup>1,3</sup> Using a laser as light source can increase the Raman scattering as it provides intense monochromatic light. However, tuning the frequency of the laser light with respect to the electronic transition characteristics of the molecule under investigation can greatly increase the Raman scattering. When a molecule is excited with incident light whose frequency is within an electronic absorption band, the intensity of some Raman spectral lines is greatly enhanced. The effect is called resonance Raman scattering and is due to a coupling of electronic and vibrational transitions (shown in figure 2.5). In resonance Raman spectroscopy, the lines due to the vibrational modes of the chromophore or adjacent groups of atoms are selectively enhanced, and the number of resonance Raman lines is less than the number of the lines in the nonresonance Raman spectrum.<sup>3</sup> In this way detailed selective information about the chromophore can be obtained.

#### ***2.4.2. Theoretical background***

The scattering of light can be expressed in terms of classical mechanics. If a molecule interacts with light, the electric field of photons will exert oppositely directed forces on the electrons and the nuclei. As a result the electrons will be displaced relative

to the nuclei, and the polarized molecule will have an induced dipole moment caused by the external field. This oscillating dipole moment acts as a source of light scattering. The induced dipole moment  $P$  is proportional to the electric field and polarizability  $\alpha$  of the molecule:  $P = \alpha E$ . Since the electric field is an oscillating function dependent upon the frequency of the light  $\nu_0$ ,  $E = E_0 \cos 2\pi\nu_0 t$ . Therefore,  $P = \alpha E_0 \cos 2\pi\nu_0 t$ . The polarizability  $\alpha$  is dependent upon the position of the nuclei in the molecule. For nuclei, corresponding to a molecule containing  $N$  atoms, the possible positions that produce molecular vibrations are  $(3N-5)$  in case of diatomic linear molecule and  $(3N-6)$  in case of polyatomic molecule. Position dependent  $\alpha$  is expressed in terms of normal coordinates  $Q$ :

$$\alpha = \alpha_0 + \left( \frac{\delta\alpha}{\delta Q_1} \right)_0 Q_1 + \dots \dots \quad (2.6)$$

If the molecule is vibrating with frequency  $\nu_1$  and the maximum vibrational amplitude is  $Q_1^0$ , then the induced dipole moment can be expressed by

$$P = \alpha_0 E_0 \cos 2\pi\nu_0 t + \frac{1}{2} E_0 Q_1^0 \left( \frac{\delta\alpha}{\delta Q_1} \right)_0 \times [\cos 2\pi t(\nu_0 + \nu_1) + \cos 2\pi t(\nu_0 - \nu_1)] \quad (2.7)$$

This equation predicts the three basic light scattering modes due to the induced dipole moment  $P$  oscillating at frequency  $\nu_1$ .<sup>1</sup> The first term refers to Rayleigh scattering (elastic), the second term to anti-Stokes lines, and the third term Stokes lines. The fundamental difference between Raman and infrared spectroscopy is that  $\delta\alpha/\delta Q$  does not equal zero for Raman scattering. This means that a molecule must have a change in its polarizability as it vibrates in order to be Raman active.

### **2.4.3. Surface enhanced Raman spectroscopy**

Surface enhanced Raman spectroscopy (SERS) is a surface-sensitive technique that enhances Raman scattering by molecules adsorbed on or in the vicinity of metal nanostructures.<sup>24</sup> The enhancement factor can be as much as  $10^4$  to  $10^{15}$  which means the technique may detect single molecules.<sup>25</sup> SERS provides the unique vibrational spectrum of a molecule, a Raman fingerprint and does not require labels or other markers. It can directly identify the molecular structure based on the spectroscopic fingerprint. The giant enhancement in SERS can be attributed to two mechanisms. The first is a result of electromagnetic enhancement that arises due to the localized surface plasmon resonance (LSPR) modes, which can focus light into nanosized volumes, drastically increasing the E-field intensity near the nanostructures.<sup>26</sup> The second is chemical enhancement, which is thought to arise from interactions between the molecule and the nanoparticle as a result of changes to the molecular electronic states. This leads to resonant enhancement from molecular excitations or charge transfers between the molecule and the nanoparticle.<sup>27</sup> The electromagnetic mechanism is typically thought to contribute most of the enhancement ( $10^5$ - $10^8$ ), and the chemical enhancement contributes much less ( $10^1$ - $10^3$ ); however, this remains an active area of research.<sup>28,29</sup>

### **2.4.4. Instrumentation**

A Raman spectrophotometer essentially consists of a light source, sample compartment, monochromator, detector and electronic-signal-processing unit (shown in Figure 2.6). In our laboratory, Raman and SERS signals are measured by a custom designed visible Raman spectrophotometer. Its basic parts are (i) light source: argon/krypton ion laser system (Coherent) operating in the visible region of spectrum

(488 nm excitation wavelength is usually used) (ii) sample compartment: quartz cuvette (liquid) or a movable metal holder for solid substrates, (iii) monochromator: single grating monochromator (Jobin Yvon,

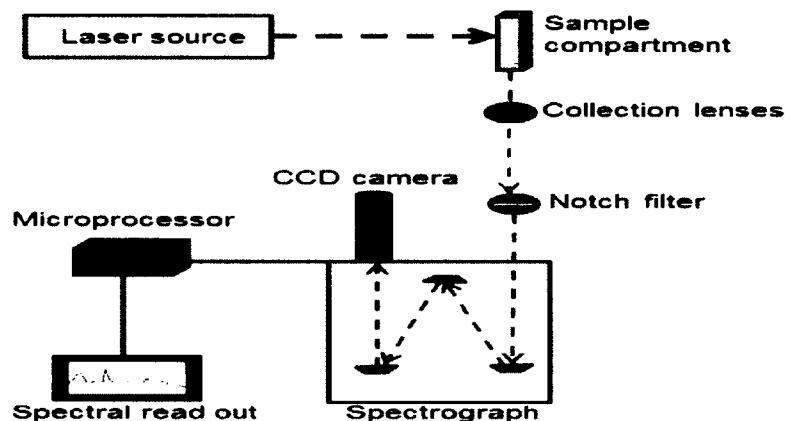


Figure 2.6. Schematic diagram of basic components in a Raman spectrophotometer.

focal length 640 mm) as well as a notch filter for removing laser light, (iv) detector: liquid nitrogen cooled charged couple device camera (Princeton Instruments) connected with a controller (v) microprocessor: to convert light into electronic signal, (vi) computer to display the spectral signal. The Raman/SERS spectra are collected by WinSpec/32 software and further processed by GRAMS/AI spectral data processing software. Spectra are displayed in pixels so a standard usually cyclohexane (as its peaks are intense and positions are known) is used to convert pixels into wavenumbers. The final spectrum is the average of several spectra, taken at different spots, of each sample.

#### **2.4.2. Ultraviolet-visible absorption spectroscopy (UV-vis spectroscopy)**

This spectroscopic technique is a common spectroscopic technique that is used to detect analyte molecules by measuring molecular absorption corresponding to electron transition (from ground state to excited state) in the ultraviolet and visible region of the spectrum. The working principle of this technique is the Beer-Lambert law ( $A = \log(I_0/I)$ )

=  $\epsilon$ . c. l) which relates the molecular absorption to its concentration. However, in plasmonics UV-vis spectroscopy has become a popular tool for far-field optical characterization of plasmonic materials. In this thesis work UV-vis spectroscopy was employed to characterize the plasmonic response of metal nanostructures and their 2D assemblies on solid substrates by measuring their extinction (absorption+ scattering) spectrum. The extinction spectrum of a nanostructure consists of peaks arising from localized surface plasmon absorption at the resonance frequency. The specific location and the number of the peaks as well as strength of the peaks depend strongly on the morphological features of the metal nanostructures and their 2D assemblies. For example, the width of the peak is related to the particle size distribution, the peak position can be used to determine particle sizes and the number of peaks is related to the shape of the nanostructures.

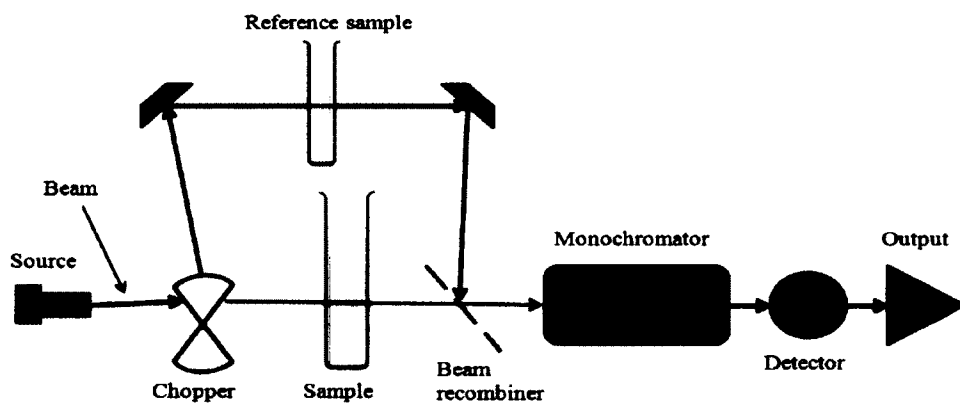


Figure 2.7. Diagram of a standard double beam UV-vis absorption spectrophotometer.

In this thesis work, extinction spectra of silver and gold nanoparticles were recorded by either CARY 3 UV-Vis spectrophotometer or Shimadzu UV-2450 UV-vis spectrophotometer (mostly used in this thesis work). The basic components of Shimadzu

UV-2450 UV-vis spectrophotometer are (I) light source: halogen and deuterium lamps, (II) monochromator: double monochromator with a high-performance double-blazed holographic grating and (III) detector: photomultiplier R-928 with spectral resolution of 0.1 nm (Figure 2.7).

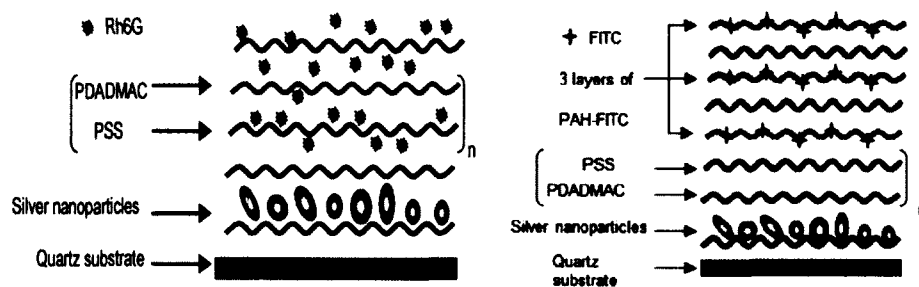
#### 2.4. References

1. Turkevich, J.; Stevenson, P.C. and Hillier, J. *Discuss. Faraday Soc.* **1951**, *11*, 55.
2. Lee, P. C.; Meisel, D. J. *Phys. Chem.* **1982**, *86*, 339.
3. Koh, A. L.; Bao, K.; Khan, I.; Smith, W. E.; Kothleitner, G.; Nordlander, P.; Maier, S. A.; McComb, D. W. *ACS Nano* **2009**, *3*, 3015.
4. Guingab, J.D.; Lauly, B.; Smith, B.W.; Omenetto, N.; Winefordner, J.D. *Talanta* **2007**, *74*, 271.
5. Wiley, B.; Sun, Y.; Xia, Y. *Acc. Chem. Res.* **2007**, *40*, 1067.
6. Hyuk Im, S.; Lee, Y.T.; Wiley, B. and Xia, Y. *Angew. Chem. Int. Ed.* **2005**, *44*, 2154.
7. Siekkinen, A. R.; McLellan, J. M.; Chen, J.; Xia, Y. *Chem. Phys. Lett.* **2006**, *432*, 491.
8. Langmuir, I. *Trans. Faraday Soc.* **1920**, *15*, 62.
9. Blodgett, K. B. I. *Am. Chem. Soc.* **1934**, *56*, 495.
10. Blodgett, K. B. I. *Am. Chem. Soc.* **1935**, *57*, 1007.
11. Yang, P and Kim, F. *ChemPhysChem* **2002**, *3*, 503.
12. Chung, S.W.; Markovich, G.; Heath, J.R. *J. Phys. Chem. B* **1998**, *102*, 6685.
13. Petty, M. Langmuir-Blodgett films: An Introduction, Cambridge university press, **1996**.

14. Roberts, G. Langmuir-Blodgett Films, Plenum press, New York, **1990**.
15. Binning, G.; Quate, C.F.; Gerber, Ch. *Phys. Rev. Lett.* **1986**, *56*,930.
16. Albrecht, T.R. and Quate, C.F. *J.Appl.Phys.***1987**, *62*, 2599.
17. Meyer, G. and Amer, N.M. *Appl.Phys.Lett.***1990**, *56*, 2100.
18. Bushan, B. Springer hand book of nanotechnology, 2<sup>nd</sup> edition.
19. Albrecht, T.R.; Akamine, S.; Carver, T.E. and Quate, C.F. *J.Vacuum Sci. Technol. A*, **1990**, *8*,386.
20. Zhong, Q; Inniss, D; Kjoller, K; Elings, V 1993, *Surface Science Letters* **1993**, *290*, L688-L692.
21. Anthony, T. Tu. "Raman Spectroscopy in biology", John Wiley and Sons, **1982**.
22. Anderson, A. The Raman Effect, Marcel Dekker INC., New York, **1973**.
23. Atkins, P.; Paula, J. De. 7<sup>th</sup> edition, W.H. Freeman and Company, New York.
24. Campion, A.; Patanjali, K. *Chem. Soc. Rev.* **1998**, *27*, 241.
25. Pillai, Z. S.; Kamat, P. V. *J. Phys. Chem. B* **2004**, *108*, 945.
26. LeRu, E.; Meyer, M.; Etchegoin, P. *J. Phys. Chem. B* **2006**, *110*, 1944.
27. Kelly, K.; Coronado, E.; Zhao, L.; Schatz, G. *J. Phys. Chem. B*,**2003**, *107*, 668.
28. Doering, W. E.; Nie, S. *J. Phys. Chem. B* **2002**, *106*, 311.
29. Rycenga, M.; Cogley, C.M.; Zeng, J.; Li, W.; Moran, C.H.; Zhang, Q.; Qin, D. and Xia, Y. *Chem. Rev.* **2011**, *111*, 3669.

## Chapter 3

### Fabrication and Studying Optical Field Enhancing Effects of Self-assembled Monolayer of Silver Nanoparticles



### 3.1. Introduction

Noble metal nanoparticles (NPs) and their assemblies are attracting increasing attention in nanotechnology due to their exciting near field and far field properties the center of which is the surface plasmon resonance.<sup>1,2</sup> Silver and gold nanoparticles are known to support surface plasmons (conduction band free electrons gas) that can be excited by external electromagnetic field such as UV-vis light.<sup>3</sup> When a surface plasmon is confined to a particle of a size comparable to the wavelength of light, the particles free electrons participate in the collective oscillation, and it is termed a localized surface plasmon (LSP). The LSP has two important effects. First, electric field near the particle's surface is highly enhanced, this enhancement being greatest at the surface and rapidly falling off with distance. This localized electric field modifies the absorption, scattering and emission processes of near-by dipoles.<sup>4, 6</sup> This enhanced local field is the basis of surface enhanced Raman scattering (SERS) and surface enhanced fluorescence (SEF).<sup>7</sup> Second, the particle's optical extinction has a maximum at the plasmon resonant frequency, which occurs at visible wavelengths for noble metal nanoparticles. This extinction peak depends on the refractive index of the surrounding medium and is the basis for the sensing applications.

The decaying nature of electric field can be realized by placing probe molecules at various distances from NPs surface and detecting their far field properties such as SERS and SEF. Such field enhancing effects are being widely used in Raman and fluorescence based molecular detection, molecular biology, and medical diagnostics.<sup>8,9</sup>

Recently, our research group studied the lateral spatial distribution of fluorescence enhancement for a system containing Rhodamine 6G (Rh6G) and a monolayer of silver nanoparticles with polyelectrolyte (PE) multilayer as spacer. The important finding of this investigation was the inhomogeneous distribution of fluorescence enhancement in those substrates.<sup>10</sup> Therefore it was of further interest to investigate the axial spatial dependence of both Raman and fluorescence enhancement in such substrates.

Distance dependent enhancement of Raman and fluorescence involve investigation of enhancement at various distances of probe molecules from the metal nanostructures. Various protocols are available for controlling the distance between metal nanostructure and the probe molecules i.e.; alternating monolayers of biotinylated bovine serum albumin–avidin, silica coating around the nanoparticles, sequential deposition of oppositely charged PE or various spacer groups having different lengths.<sup>11- 13</sup> Self-assembly monolayer (SAM) technique is a simple technique to assemble nanostructures into 2D fashion. An advanced level of self-assembly technique is the layer by layer (LBL) technique by which thin film of different thickness can be engineered.<sup>14</sup> One of the advantages of LBL technique is the ability to incorporate various materials of interest including dyes, biological agents like proteins, DNA, antibodies etc.<sup>15, 16</sup> Distance control by PE using LBL process has been found to give uniform film with controllable thickness within a short time.<sup>17</sup>

A reliable investigation of the distance dependence of SERS and SEF not only depends on how well the distance is controlled but also the interactions between probe molecules and spacer matrix, as it might affect the molecular distribution of the probe

molecule on the substrates. Therefore, interaction of probe molecules with PE film is another issue that has to be addressed. In the present work, we assembled silver nanoparticles on planer solid substrate using self-assembled monolayer technique and studied near field distribution of electric field surrounding silver nanoparticles by investigating distance dependent SERS and SEF enhancement. The distance between the NPs monolayer and the probes is maintained by depositing varied number of PE (poly (sodium-4-styrenesulfonate) (PSS)/Poly (diallyldimethylammonium chloride) (PDADMAC). Two probes that were used in this study are the Rh6G and Poly (fluorescein isothiocyanate allylamine hydrochloride) (PAH-FITC). However, as a preliminary study of this thesis work, this research work addressed different issues regarding fabrication of NPs assembly, PE thin film and possible interaction of probe molecules with the PE matrix.

## **3.2. Experimental**

### **3.2.1. Chemicals**

Poly (diallyldimethylammonium chloride) solution (PDADMAC; 35 wt % in water, MW <100,000), poly (sodium- 4-styrenesulfonate) (PSS; MW~70,000), Rhodamine 6G (Rh6G), poly (fluorescein isothiocyanate allylamine hydrochloride) (PAH-FITC; MW ~6031), and sodium borohydride 98% were received from Aldrich. Hydrogen peroxide 30 %, sodium citrate, and silver nitrate were received from Caledon, Anachemia and BioShop respectively.

### ***3.2.2. Preparation of Metal Nanoparticles***

Silver nanoparticles were synthesized by the well-known chemical reduction method.

<sup>1</sup> In a typical experiment  $\text{AgNO}_3$  ( $1 \times 10^{-3}$  M) solution was mixed with ice-chilled sodium borohydride ( $2 \times 10^{-3}$  M) solution in a 1:3 volume ratio with constant stirring. The resulting silver hydrosols exhibited a yellow color.

### ***3.2.3. Preparation of Polyelectrolytes Solutions***

A stock solution of  $1 \times 10^{-3}$  M NaCl was prepared using Milli-Q (18.2 M $\Omega$ ) water as a solvent. This solution was used for making 1mg/ml PSS, PDADMAC and PAH-FITC solutions.

### ***3.2.4. Modification of Quartz Slides***

The quartz (CHEMGLASS, 25×25mm) slides were rinsed with acetone and then sonicated in concentrated  $\text{H}_2\text{SO}_4$  for 30 min. After washing copiously with Milli-Q water, cleaned slides were heated in piranha solution consisted of 5:1:1 by volume  $\text{H}_2\text{O}:\text{NH}_3:\text{H}_2\text{O}_2$  at 70°C for 10 min to make a negatively charged substrate surface. These slides were thoroughly rinsed with Milli-Q water followed by drying in a stream of  $\text{N}_2$  gas. The slides were then immersed in a freshly prepared PDADMAC solution for 15 min to create a positively charged surface and rinsed with Milli-Q water. All the slides were subjected to drying in a stream of  $\text{N}_2$  gas prior to the deposition of metal nanoparticles.

### ***3.2.5. Assembly of Nanoparticle Monolayer on Modified Quartz Substrate***

The substrates prepared in previous steps were dipped into a colloidal solution of silver nanoparticles for 24 hours followed by rinsing with Milli-Q water for three minutes

to remove aggregates. Deposition of the nanoparticles on the substrates was monitored by the SPR absorption spectra of those substrates using CARY 3 UV-Vis spectrophotometer.

### ***3.2.6. Deposition of Polyelectrolytes Multilayer***

The polyelectrolytes layers were deposited by successively dipping the substrate (with or without a monolayer of silver nanoparticles) into the solution containing negatively charged polyelectrolyte PSS for 15 min, after which the substrates were rinsed with Milli-Q water for 2 min and then dipped into the oppositely charged polyelectrolyte, PDADMAC, solution for another 15 min. This process was repeated until the desired number of layers was achieved. The growth of the layers was checked by monitoring UV-Vis spectra of polyelectrolyte multilayers after five bilayers of PE (successive deposition of PSS/PDADMAC is referred to as one bilayer throughout the study) had been deposited. The absorption intensity of PSS at 227 nm was used as a reference signal for monitoring the layer growth. A clean quartz slide treated with piranha solution was used as a reference for the spectral measurements. All the UV-Vis spectra were processed by GRAMS/AI software.

### ***3.2.7. Deposition of Dyes on the Substrate***

Dyes (Rh6G and FITC) were deposited on the top of polyelectrolyte multilayers with negatively charged PSS being the top layer using the method described by Wang.<sup>18</sup> Briefly, the substrates (with or without nanoparticles) containing different number of PE bilayers were dipped into the solutions of Rh6G (pH~2.5,  $1 \times 10^{-3}$  M) and PAH-FITC (pH~ 4, 1mg/mL) for 20 min. However, three layers of PAH-FITC were deposited onto the PE multilayers instead of one as in the case of Rh6G. This was done by deposition of

PAH-FITC on the top PSS layer and further deposition of two additional PSS/PAH-FITC bilayers. After immersion, the substrates were rinsed thoroughly with Milli-Q water for 2 min then dried in a stream of nitrogen.

### ***3.2.8. Raman and Fluorescence Analysis***

Raman and fluorescence measurements were performed using a single grating monochromator (Jobin Yvon, focal length 640 mm) equipped with a liquid nitrogen cooled CCD camera (Princeton Instruments) and a notch filter to remove the excitation wavelength. Argon ion laser system (Coherent), operating at 488 nm excitation wavelength with an output power of 0.48 mW was used for excitation. The spectral resolution of the instrument was  $\sim 4 \text{ cm}^{-1}$ . The accumulation time was 60 s. The Raman spectra were collected by WinSpec/32 software and further processed by GRAMS/AI software.

### ***3.2.9. Topography Imaging***

The topography image of the metal nanoparticle monolayer was taken on a multimode Nanoscope III (Digital instruments, Santa Barbara, CA) or Ntegra (NTMDT, Russia) atomic force microscope (AFM) in the contact mode in air. A J scanner with maximal scan area of  $120 \mu\text{m}^2$  (Nanoscope) or  $100 \times 100 \mu\text{m}^2$  (Ntegra) and 200  $\mu\text{m}$ -long soft cantilevers with integrated pyramidal silicon nitride tips having spring constant of 60 mN/m were used for all topographic measurements. The imaging force was approximately 2 to 4 nN, and the scan rate was typically 0.5 Hz.

### 3.3. Results and Discussion

#### 3.3.1. Characterization of silver nanoparticle monolayer

Self-assembly of Ag nanoparticle on the substrate is governed by the electrostatic interaction between the negatively charged Ag nanoparticles and positively charged pre-deposited PDADMAC.<sup>1-2,16</sup> Formation of monolayer was confirmed by AFM topographic image of the substrate as shown in figure 3.1A. It is obvious from the AFM image that the monolayer consists of semi-spherical Ag nanoparticles having a mean diameter of ~20 nm with several aggregates.

The aggregates were formed either during synthesis or coalescence of smaller particles during the deposition process. UV-vis absorption spectra of the monolayer (shown as solid line in figure 3.1B) exhibits a characteristic peak centered at 400 nm corresponding to excitation of dipolar plasmon modes. However, SPR peak appears at 391 nm for colloidal nanoparticle solutions as shown by dotted line in Figure 3.1B.

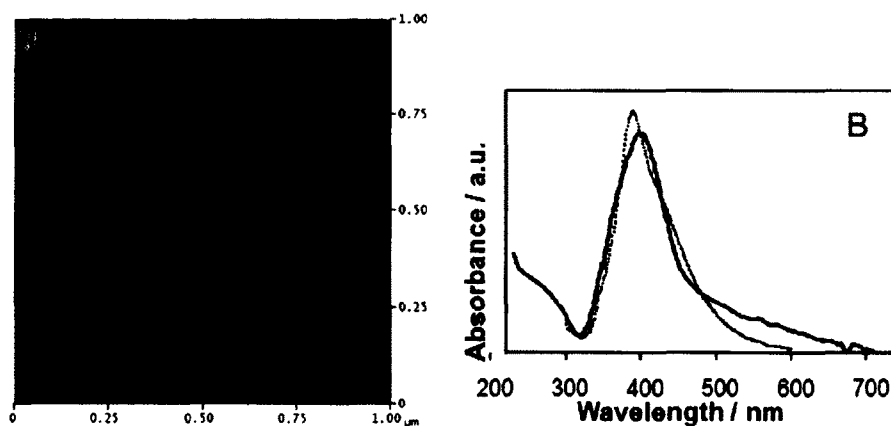


Figure 3.1. (A) AFM topography image of a substrate containing a monolayer of silver nanoparticles deposited on modified quartz slide, (B) the corresponding surface plasmon resonance absorption spectra of the Ag nanoparticle monolayer (solid line) and the spectrum of the colloidal nanoparticles solution (dotted line).

### ***3.3.2. Growth of PE film***

We prepared two series of substrates; one series contained Rh6G and another contained PAH-FITC. In each series variable number ( $n=1, 5, 10, 20,$  and  $30$ ) of polyelectrolytes bilayers (PSS/PDADMAC) were deposited on five different substrates each containing a monolayer of Ag nanoparticles. Electrostatic interaction between oppositely charged polyelectrolytes and subsequent charge reversal are the driving forces for PE film growth. The growth of the films was monitored by measuring the absorption intensity of PSS at 227 nm (Figures 3.2A and 3.4A). Plots of absorption intensity as a function of number of bilayers deposited on both series of substrates show a linear growth of PE multilayer films. Such plots are presented in figure 3.2B for Rh6G series and in Figure 3.4B for PAH-FITC series. Such linear dependence of thickness reveals regular deposition of PE in each deposition cycle which is important for distance controlled experiments.<sup>16</sup>

### ***3.3.3. Monitoring fluorophore diffusion in nanocomposites***

Reliable investigations of the lateral and axial dependence of Raman and fluorescence enhancement depend on the ability to position the probe molecules at a well-defined distance from the nanoparticles. In this work, spectral absorption peaks of Rh6G and FITC were used to confirm the homogeneity of the fluorophores distribution.

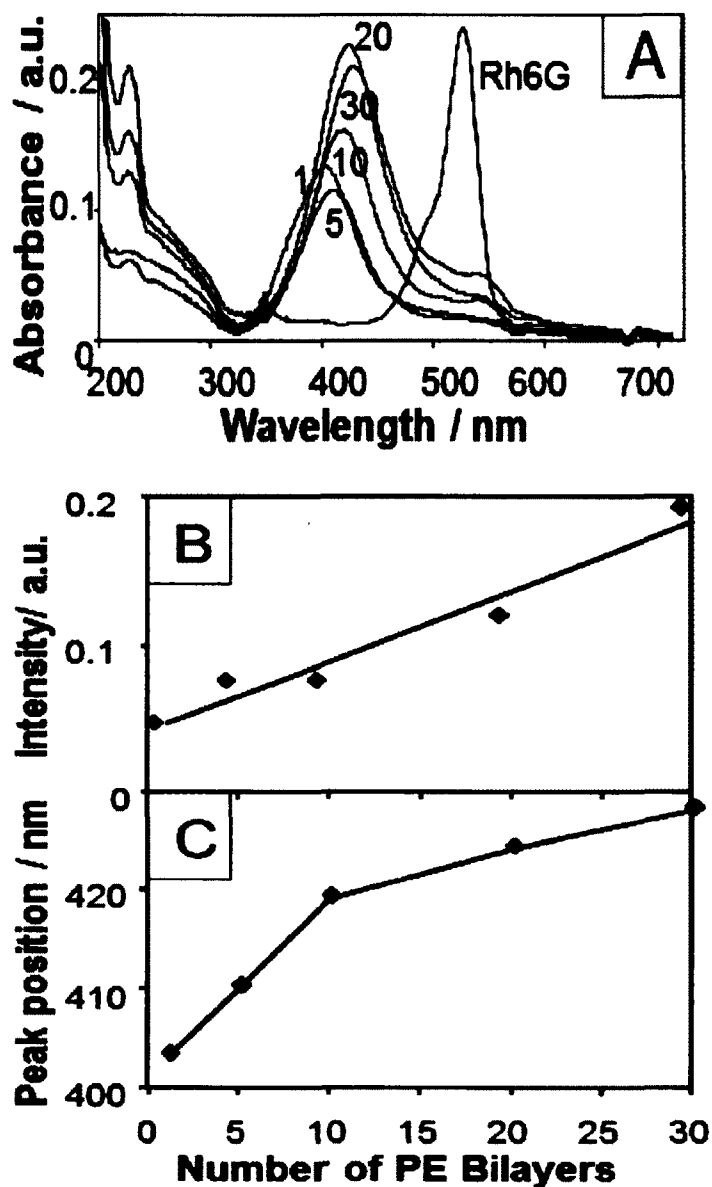


Figure 3.2. (A) UV-Vis absorption spectra of the substrates containing nanoparticles, a variable number (1, 5, 10, 20 and 30) of PE bilayers (PSS/PDADMAC) and Rh6G. Solution phase spectrum of Rh6G ( $1 \times 10^{-6}$  M, pH~2.5) is shown to track the position of Rh6G absorption signal of the substrates. (B) Absorbance at 227 nm was used to monitor the growth of PE film. (C) Position of surface plasmon (SP) absorption maxima shifts as the number of PE bilayers increases.

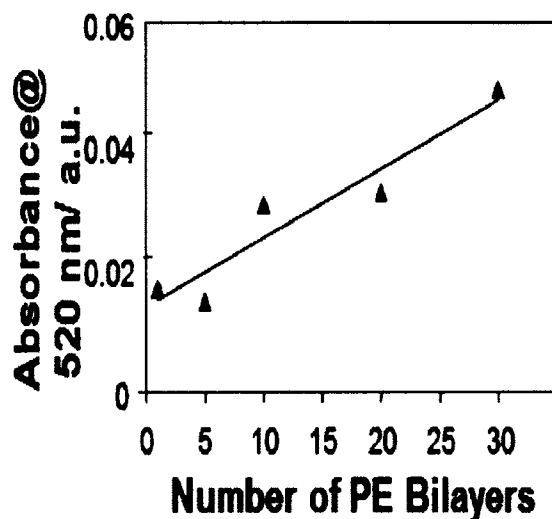


Figure 3.3. Dependence of Rh6G absorption intensity with increasing number (1, 5, 10, 20 and 30) of PE bilayers.

Figure 3.2A shows the UV-Vis absorption spectra of the substrates containing Rh6G as well as its solution phase spectrum. The growth of the PE film on the nanoparticle-monolayer can be monitored by measuring the intensity of PSS absorption at 227 nm (Figure 3.2B) as well as by the progressive shift in the position of the dipolar plasmon resonance peak (Figure 3.2C), which is known to be sensitive to the near-field change of the dielectric environment.<sup>6, 19, 20</sup> In aqueous solution Rh6G absorbs at ~520 nm.<sup>21</sup> It can be seen from the figure 3.2A that the intensity of absorption of Rh6G at ~ 520 nm increases with increasing number of PE bilayers. The linear dependence of Rh6G absorption intensity with PE film growth (Figure 3.3) indicates that dye content of the substrates increases with increasing film thickness. Since the dye deposition conditions as well as the experimental procedures were kept consistent for preparing all the substrates, the only possibility is the diffusion of Rh6G molecules through the PE film matrix with increasing film thickness.

The same experiment was carried out with PAH-FITC, a labeled polyelectrolyte (Figure 3.4). In aqueous solution FITC (pH~4) shows an absorption peak at 496 nm, (Figure 3.4A)

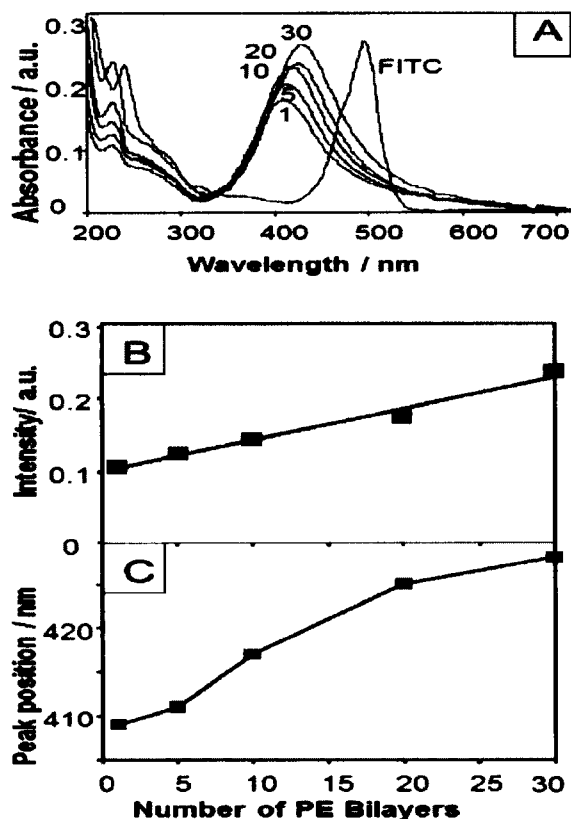


Figure 3.4. (A) UV-Vis absorption spectra of the substrates containing nanoparticle-monolayer, a variable number (1, 5, 10, 20 and 30) of PE bilayers (PSS/PDADMAC) and PAH-FITC. Solution phase spectrum of PAH-FITC ( $1 \times 10^{-6}$  M, pH~4) is shown to track the position of PAH-FITC absorption signal. (B) Absorbance at 227 nm was used to monitor the growth of PE film. (C) Position of surface plasmon (SP) absorption maxima shifts as a function of number of PE bilayers.

Three rather than one layers of PAH-FITC were deposited on the top of nanocomposite substrates in order to simplify the detection. However, no detectable signal from the adsorbed probe was noticed around 496 nm even for 30 PE bilayers. Film

thickness behavior (Figure 3.4B) and surface plasmon resonance shift (Figure 3.4C) were similar to figure 3.2 experiment.

To investigate whether any change in dye absorption intensity occurs with increasing number of PAH-FITC layers, we prepared substrates containing different number of PAH-FITC layers by replacing PDADMAC with PAH-FITC. For eliminating extinction spectra of nanoparticles which might have engulfed the absorption signal of the dye, no nanoparticles were deposited on those substrates. The UV-Vis absorption spectra of these substrates are shown in figure 5. The PSS/PAH-FITC film growth also follows a linear fashion (Figure 3.5, inset bottom). We noticed a detectable absorption signal of FITC only after 10 layers of FITC had been deposited and observed a linear increase of the absorbance with the number of PAH-FITC layers (Figure 3.5, inset, top).

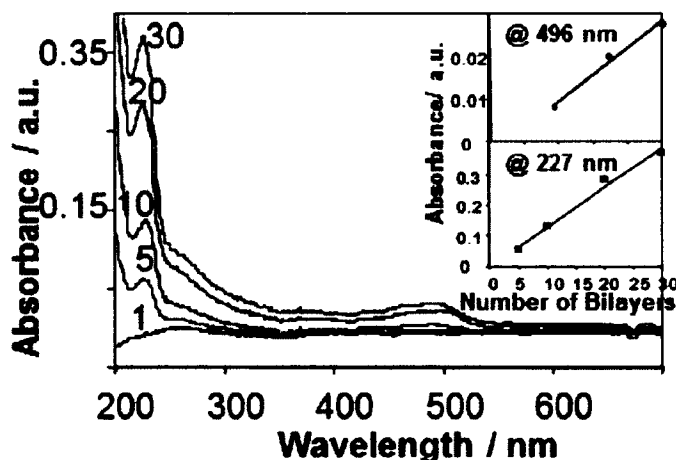


Figure 3.5. UV-Vis absorption spectra of the substrates without NP containing variable number (1, 5, 10, 20 and 30) of PE bilayers (PSS/PAH-FITC). PSS absorption at 227 nm was observed only after the deposition of 5 bilayers and a detectable FITC absorption (at 496 nm) signal was seen after deposition of 10 bilayers. Growth of PSS/PAH-FITC PE film (absorption @ 227 nm) and variation of FITC absorption intensities (absorption @ 496 nm) with increasing number of PE bilayers are shown.

These results suggest that unlike Rh6G, FITC-labeled polyelectrolyte does not diffuse through the PE film matrix.

#### ***3.3.4. Effect of local environment on surface plasmon resonance absorption***

It is known that a change in the dielectric medium around the nanoparticles causes red shift in plasmon resonance absorption.<sup>6</sup> In this present study, dielectric medium was altered by depositing different number of PE layers on the surface of the nanoparticle-monolayer. The effect of local environment on the position of dipolar plasmon resonance peak has been displayed in figures 3.2.C for Rh6G series and 3.4.C for PAH-FITC series. We found a steady increase in plasmon resonance absorption peak until 20 bilayers (corresponds to approx. 20 nm) was deposited for both series of substrates. We assume that local electromagnetic field associated with 20 nm metal nanoparticles extends to this distance. Within the region confined by the limiting distance from the nanoparticle surface, attendance of dielectric materials lowers the frequency of plasmon oscillation<sup>6</sup>. Once the dielectric function within the limiting region is established further deposition of PE layers does not bring any significant change<sup>6, 22</sup> in plasmon resonance shift.

#### ***3.3.5. Concentration correction for SERS and SEF***

It is important to normalize the SERS and SEF of the substrates containing Rh6G to account for the variation of dye content in the substrates as a result of diffusion. For concentration correction, we employed a control substrate which was a modified quartz slide containing Rh6G (without PE and NPs). We introduced a term correction factor for normalizing SERS and SEF of the substrates. Correction factor (CF) is defined as the

ratio of Rh6G absorption intensity in the nanocomposite substrate ( $^{Rh6G} I_{NC}$ ) to that of in the control substrate ( $^{Rh6G} I_{CON}$ ) i.e.; C.F. =  $^{Rh6G} I_{NC} / ^{Rh6G} I_{CON}$ . Finally, the SERS and SEF of individual substrates were divided by their corresponding correction factors to obtain the normalized SERS and SEF.

### **3.3.6. Enhancement factor calculation**

Magnitude of SERS or SEF enhancement was estimated by enhancement factor. Enhancement factor (EF) is defined by the following relation  $EF = I_{Ag} / I_0 = I_{SERS} / I_{RS}$  (or  $I_{SEF} / I_F$ ) where  $I_{Ag}$  and  $I_0$  are the intensities of SERS (or SEF) signal of dye molecules adsorbed on Ag nanoparticles substrates and that adsorbed on substrates without Ag nanoparticles respectively.  $I_{SERS}$  (or  $I_{SEF}$ ) and  $I_{RS}$  (or  $I_F$ ) are the Raman (or fluorescence) intensities of the dyes under SERS (or SEF) and non-SERS (non-SEF) conditions respectively.

### **3.3.7. SERS activities of the substrates**

Metal nanoparticles have long been known to enhance the Raman scattering of the molecules adsorbed on their surface as a result of intense electric field, induced by external EM radiation, around the nanoparticles. It is reported that the electric field is greatest on the surface and falls off within few nanometers. The decaying nature of local field can be realized by investigating SERS and SEF enhancement at different distances from the surface of NPs.<sup>3, 23-29</sup> We employed the aforementioned substrates containing Ag nanoparticles and dyes (Rh6G and PAH-FITC) to study distance dependent enhancement of SERS and SEF. These substrates contained a variable number of PE (PDADMAC/PSS) bilayers as spacer between the Ag nanoparticle monolayer and the

dyes. We also prepared a substrate containing dye adsorbed on a bare slide as a control for estimating SERS and SEF enhancement factor. Figure 3.6 shows the SERS spectra (with fluorescence background) of the substrates containing Rh6G. It is evident that Raman spectrum of the Rh6G monolayer (indicated by '0') deposited on the bare slide is very weak and cannot be resolved under the experimental conditions used. However, one can observe a weak background due to the fluorescence of Rh6G. The addition of the nanoparticles to the substrates leads to a dramatic increase in the Raman scattering intensity. The bands observed at 1364, 1513, 1581 and 1665  $\text{cm}^{-1}$ , assigned to aromatic C-C stretching vibrations of Rh6G are the characteristics of SERS signature of Rh6G.<sup>29</sup>

<sup>30</sup> Intensities of the band around 1665  $\text{cm}^{-1}$  for different substrates were measured and normalized for concentration correction as described earlier. SERS enhancement factors of different substrates were estimated from these normalized intensities and found to follow a decreasing trend with maximum enhancement exhibited by a substrate containing single PE bilayer (Figure 3.7). The enhancement of SERS is due to the intense local electric field surrounding the NP and the reduction of enhancement with increasing film thickness is because of decaying nature of the near field.<sup>31-36</sup> No detectable SERS signal from FITC was observed likely because of relatively small SERS enhancement factor.

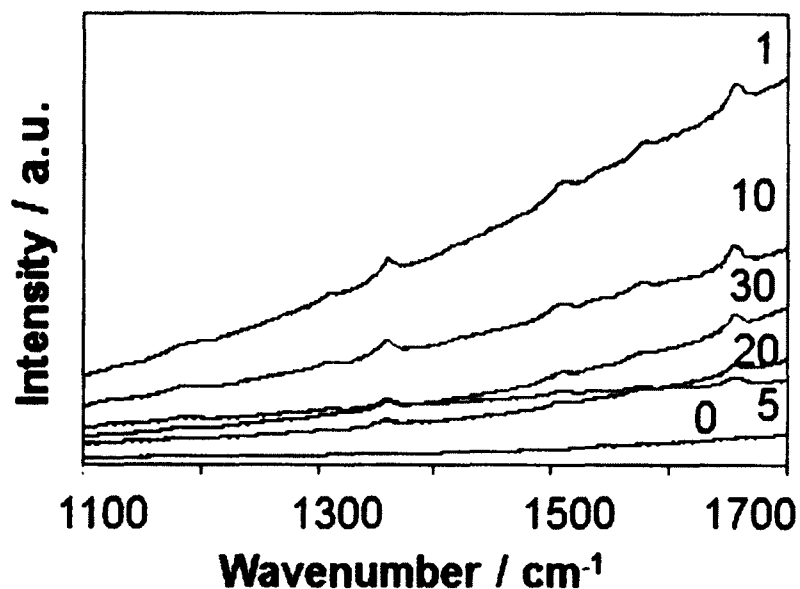


Figure 3.6. SERS spectra (with fluorescence background) for substrates containing a monolayer of Ag nanoparticles covered with variable number (1, 5, 10, 20 and 30) of PE bilayers (PSS/PDADMAC) and Rh6G. '0' refers to a substrate used as control with Rh6G deposited on bare (without Ag NP and PE bilayers) quartz slide.

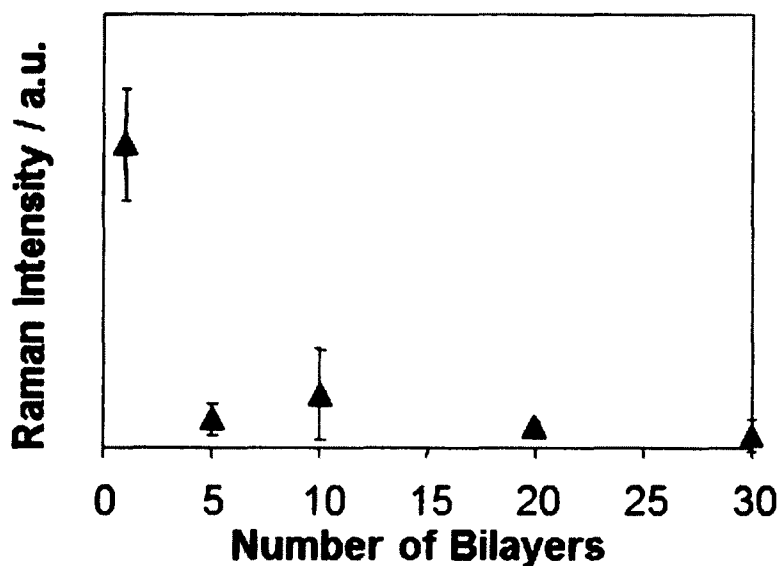


Figure 3.7. Distance dependence of the Rh6G SERS signal measured by using the intensity of the Raman scattering band at  $1665\text{ cm}^{-1}$  as a function of the number of bilayers from the figure 3.6 spectra. Intensity was adjusted by using the figure 3.3 data for the amount of Rh6G deposited on the substrates.

### **3.3.8. SEF activities of the substrates**

Similar to Raman scattering, fluorescence emission of a nearby dipole is modified by metal nanoparticles. Both enhancement and quenching of fluorescence have been reported in the literature.<sup>37</sup> In this present study, both series of substrates containing Rh6G and FITC exhibited fluorescence enhancement effect. Fluorescence emission spectra of the substrates containing Rh6G and FITC with different number of PE bilayers (1, 5, 10, 20, and 30) are presented in figures 3.6 (as a background of Raman signal) and 3.8 respectively. Fluorescence enhancement factors were calculated as described earlier. We observed a 14 fold enhancement for Rh6G and a 2 fold enhancement for FITC. Investigation of distance dependent fluorescence enhancement of Rh6G reveals that maximum enhancement occurs at a separation distance corresponding to one PE bilayer (~1 nm) and then decreases with increasing number of bilayers (Figure 3.9). Surprisingly, we did not observe quenching at the short distances reported in literature.<sup>38, 39</sup> The observed decrease in the fluorescence EF with higher number of bilayers (5 to 30) is probably explained by the formation of non-fluorescent aggregates as a result of Rh6G diffusion through the PE matrix as described in previous literature.<sup>20</sup> Distance dependent fluorescence study of PAH-FITC (Figure 3.9) shows that fluorescence intensity increases with increasing number of bilayer. The observed fluorescence enhancement is the result of two phenomena: Firstly, the static quenching of fluorescence by metal nanoparticles through non-radiative pathways, and secondly, increased radiative decay rates induced by the enhanced electric field around the nanoparticles. Since quenching decays from the

surface faster than the local EM field therefore, fluorescence intensity increases as the distance between the nanoparticles and the dye increases.<sup>6</sup>

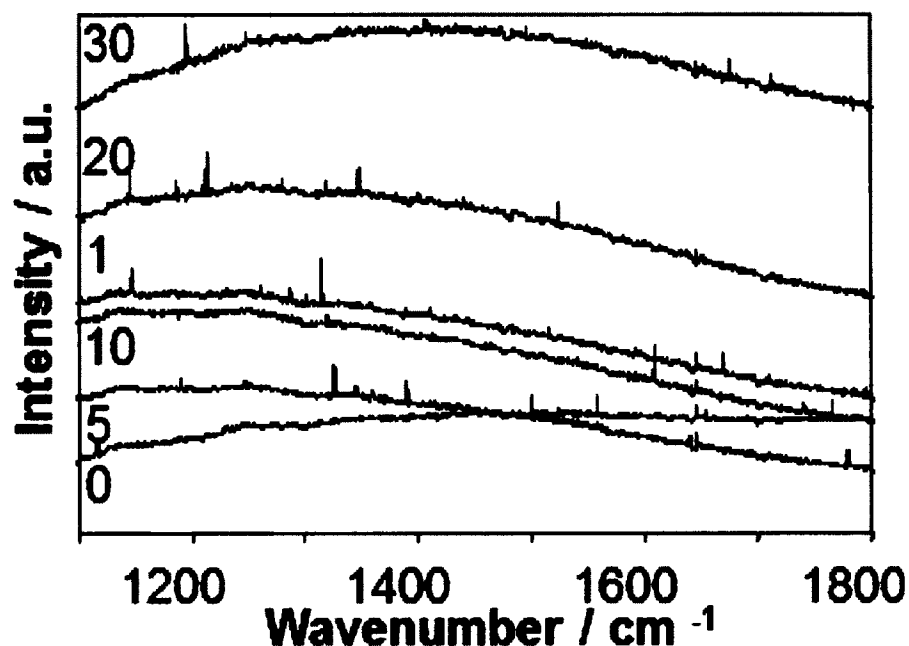


Figure 3.8. Fluorescence emission spectra of the substrates containing Ag NP, a variable number (1, 5, 10, 20 and 30) of PE bilayers (PSS/PDADMAC) with three PSS/PAH-FITC bilayers adsorbed on the top. '0' refers to a substrate used as control having PAH-FITC deposited on bare (without Ag NP and PE bilayers) quartz slide.

Compared to Rh6G, PAH-FITC exhibits an increasing trend of fluorescence enhancement with increasing number of bilayers which is consistent with the fluorescence de-quenching. The most likely explanation for this observation is that FITC molecules are bonded to PAH backbone which retards the diffusion of molecules into the PE matrix. This prevents the formation of any nonfluorescent aggregates. Another important feature is the lower fluorescence EF compares to the Rh6G which might be caused by the self-quenching of the fluorescence signal by the FITC molecules.<sup>40, 41</sup>

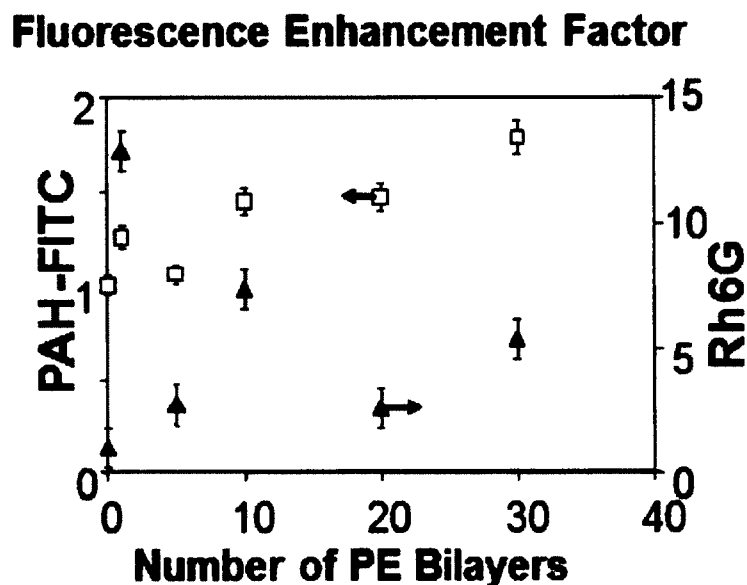


Figure 3.9. Distance dependent fluorescence enhancement of Rh6G (triangle) and FITC (rectangle) deposited on substrates containing Ag and with increasing number (1, 5, 10, 20 and 30) of PE bilayers (PSS/PDADMAC). '0' refers to the substrates used as controls having Rh6G or PAH-FITC deposited on bare (without NP and PE bilayers) quartz slides. The enhancement factors for Rh6G and FITC were estimated from the emission spectra presented in Figures 3.6 and 3.8 respectively

### 3.4. Conclusions

We fabricated silver nanoparticle-polyelectrolyte nanocomposite substrates having varied thickness and deposited two different dyes, Rh6G and PAH-FITC, on the top of the polyelectrolytes film by LBL technique process to study near field plasmonic properties of silver nanoparticle-monolayer. The distance dependent SERS enhancement of Rh6G showed a decreasing trend at distances away from the NP surface. The highest enhancement was observed at a distance corresponding to one bilayer (~1 nm). We noticed a significant diffusion of Rh6G molecules through PE matrix, which formed non-fluorescent aggregates. On the contrary, PAH-FITC did not exhibit any diffusion as it is

bound to the polyelectrolyte chain and employed to study the distance dependent SEF enhancement. However, distance dependent SEF enhancement of FITC showed an increasing trend which corroborates with de-quenching of fluorescence at distances away from nanoparticle surface. Both of the phenomena support the distance dependent decaying nature of local electric field surrounding the metal nanoparticles upon excitation of surface plasmon.

### 3.5. References

1. Jones, M.R.; Osberg, K.D.; Macfarlane, R.J.; Langille, M.R. and Mirkin, C.A. *Chem. Rev.* **2011**, *111*, 3736.
2. Caruso, F.; Spasova, M.; Salgueiriño-Maceira, V; Liz-Marzán L.M. *Adv. Materials* **2001**, *13*, 1090.
3. Rycenga, M; Cobley,C.M.; Zeng,J.; Li,W.; Moran,C.H.; Zhang,Q.; Qin,D; and Xia,Y. *Chem. Rev.* **2011**, *111*, 3669.
4. Huang, X.; El-Sayed, I.H.; Qian, W.; El-Sayed, M.A. *J. Am. Chem. Soc.* **2006**, *128*, 2115.
5. Noguez, C. *J. Phys. Chem. C* **2007**, *111*, 3806.
6. Evanoff, Jr. D.D.; White, R.L.; Chumanov, G. *J. Phys. Chem. B* **2004**, *108*,1522.
7. Jain,P. K.; Huang, W.; El-Sayed, M.A. *Nano Lett.* **2007**, *7*, 2080.
8. Domke, K.F.; Zhang, D.; Pettinger,B. *J. Phys. Chem. C* **2007** ,*111*,8611.
9. Zhang, J.; Fu,Y.; Chowdhury, M.H.; Lakowicz, J.R. *Nano. Lett.* **2007**,*7*, 2101.
10. Ianoul, A.; Bergeron,A. *Langmuir* **2006**, *22*, 10217.

11. Ray,K; Badugu,R.; Lakowicz,J.R. *Chem. Mater.* **2007**, 19, 5902.
12. Thomas,S.; Lobmaier,C.; Pittner,F. *Proc. SPIE* **1997**,2976, 129.
13. Chumanov, G.; Sokolov,K.; Gregory, B.W.; Cotton,T.M. *J. Phys. Chem.* **1995**,99, 9466 .
14. Decher, G. *Science* **1997**, 277,1232.
15. Farhat,T.R.; Hammond,P.T. *Adv. Funct. Mater.* **2006**,16, 433 .
16. Hammond, P.T. *Current Opinion in Colloid & Interface Science* **2000**,4, 430 .
17. Decher, G. "Comprehensive Supramolecular Chemistry: Templetting, Layered Nanoarchitectures via Directed Assembly of anionic and cationic molecules," *Pergamon Press, Oxford* **1996**, 9, 507.
18. Wang, Y.; Hu, C. *Thin Solid Films* 2005, 476, 84.
19. Schmitt,J.; Machtle,P.; Eck,D; Mohwald,H.; Helm, C.A. *Langmuir* **1999** ,15,3256.
20. Zhao,J.; Jensen,L.; Sung,J.; Zou,S.; Schatz,G.C.; Van Duyne,R.P. *J. Am. Chem. Soc.* **2007**,129, 7647.
21. Reisfeld,R.; Zusman,R.; Cohen,Y.; Eyal,M. *Chem. Phys. Lett.* **1988**,147, 142 .
22. Sherry,L.J.; Chang,S.H.; Schatz,G.C.; Van Duyne,R.P.; Wiley,B.J.; Xia,Y. *Nano. Lett.* **2005**,5, 2034 .
23. Jensen,T.R.; Duval,M.L.; Kelly,K.L.; Lazarides,A.A.; Schatz,G.C.; Van Duyne,R.P. *J. Phys. Chem. B*, **1999**,103, 9846 .
24. Futamata, M.; Maruyama,Y.; Ishikawa, M. *Vibrational Spectroscopy* **2002**,30, 17 .
25. Dong, S.; Zou,X. *J. Phys. Chem. B* **2006**,110, 21545 .

26. Kwon, K.; Lee, K.Y.; Lee, Y.W.; Kim, M.; Heo, J.; Ahn, S.J.; Han, S.W. *J. Phys. Chem. C* **2007**, *111*, 1161 .
27. Ringler, M.; Klar, T.A.; Schwemer, A.; Susha, A.S.; Stehr, J.; Raschke, G.; Funk, S.; Borowski, M.; Nichtl, A.; Kurzinger, K.; Phillips, R.T.; Feldmann, J. *Nano Lett.* **2007**, *7*, 2753 .
28. Le Ru, E.C.; Blackie, E.; Meyer, M.; Etchegoin, P.G. *J. Phys. Chem. C* **2007**, *111*, 13794 .
29. Pristiniski, D.; Tan, S.; Erol, M.; Du, H.; Sukhishvili, S. *J. Raman Spectroscopy* **2006**, *37*, 762.
30. Hildebrandt, P.; Stockburger, M. *J. Phys. Chem.* **1984**, *88*, 5935 .
31. Zhang, J.; Li, X.; Sun, X.; Li, Y. *J. Phys. Chem. B* **2005**, *109*, 12544.
32. McCabe, A.F.; Graham, D.; McKeown, D.; Smith, W.E. *J. Raman Spectroscopy* **2005**, *36*, 45 .
33. Le Ru, E.C.; Etchegoin, P.G. *Chem. Phys. Lett.* **2004**, *396*, 393.
34. Kambhampati, P.; Child, C.M.; Foster, M.C.; Campion, A. *J. Chem. Phys.* **1998**, *108*, 5013.
35. Compagnini, G.; Galati, C.; Pignataro, S. *Phys. Chem. Chem. Phys.* **1999**, *1*, 2351.
36. Ye, Q.; Fang, J.; Sun, L. *J. Phys. Chem. B* **1997**, *101*, 8221.
37. Fu, Y.; Lakowicz, J.R. *J. Phys. Chem. B* **2006**, *110*, 22557.
38. Lakowicz, J. R. *Anal. Biochem.* **2001**, *298*, 1.
39. Lakowicz, J. R. *Anal. Biochem.* **2005**, *337*, 171.

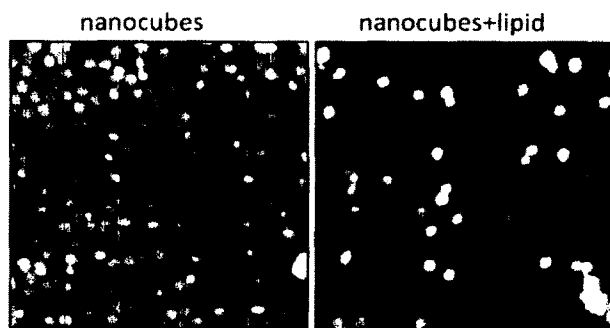
40. Deka, C. ; Lehnert, B. E. ; Lehnert, N. M. ; Jones, G. M. ; Sklar, L. A. ;  
Steinkamp, J.A. *Cytometry* **1996**,25, 271 .
41. Lakowicz, J. R.; Malicka, J.; D'Auria, S.; Gryczynski, I. *Anal. Biochem.* **2003**, 320, 1  
3.

## Chapter 4

---

### **Using Phospholipid Phase Behavior to Control Inter-particle Distance in SERS-active Substrates**

*J. Phys. Chem. C* 2011, *115* (9), 3587-3594.



#### 4.1. Introduction

Development of Surface Enhanced Raman scattering (SERS) helped alleviate the low sensitivity limitation of Raman spectroscopy<sup>1, 2</sup> by exploiting the enhanced electromagnetic (EM) field associated with excitation of surface plasmons in noble metal nanostructures. SERS was first observed with pyridine adsorbed on the surface of a roughened silver electrode.<sup>3</sup> Later it was found that colloidal metal nanoparticles (NP) can also amplify the Raman scattering by virtue of their surface plasmon excitation upon illumination with light.<sup>4,5</sup> Optical properties of metal NP can be controlled by tailoring the size and shape of the NP or through the controlled spacing of several NPs.<sup>6-10</sup> It has been demonstrated that giant enhancement of EM field occurs in NP with sharp asperities and corners as well as in inter-particle regions. Such sources capable of generating an enormous EM field are termed “hot spots”<sup>11</sup> and are thought to be good candidates for single molecule SERS substrates.<sup>12, 13</sup>

Both theoretical and experimental studies show that polyhedral shaped silver nanocrystals with well-defined facets and corners exhibit distinct optical signatures.<sup>14</sup> A nanocube (NC), entirely bound by {100} faces, exhibits specific scattering signatures because of different modes of localized surface plasmon resonances.<sup>10</sup> These nanocubes can be used as building blocks for fabrication of 2D substrates.<sup>15</sup> Since the EM field in the gaps between the nanocubes is increased due to the coupling of plasmon resonances in adjacent nanoparticles, such substrates can be used to enhance optical responses from analyte molecules located in these gaps. Nanotechnology offers several techniques to assemble nanostructures in a 2D fashion. Electron beam lithography and nanosphere lithography are two commonly used techniques to create ordered nanostructures.<sup>16,17</sup>

However, Langmuir-Blodgett (LB) monolayer technique has evolved as a versatile tool for ordering nanoscale building blocks of different compositions, morphologies and sizes.<sup>18-20</sup> El-Sayed *et al.* recently studied aggregation and optical field enhancing properties of NC substrates fabricated by LB technique.<sup>21,22</sup> They pointed out that control of inter-particle distance in a NC monolayer appears challenging. In a separate study, phase behaviour of phospholipid monolayers was used for 2D organization of hydrophobic gold nanoparticles due to the phase specific interaction of lipids with NP.<sup>23,24</sup> These two studies motivated us to investigate if phase behavior of phospholipids can be used to “disperse” NCs in a passive homogeneous matrix to help control the separation between the nanocubes. The report presented here demonstrates assembly of NC into 2D micro structures with and without phospholipids matrix. Relationship between the morphology of the monolayers and optical signal enhancing properties was studied. We employed a saturated chain phospholipid 1, 2-Dipalmitoyl-sn-Glycero-3-Phosphoethanolamine (DPPE) and its Raman- active analogue 1, 2-Dipalmitoyl-sn-Glycero-3-Phosphoethanolamine-N-(lissamine rhodamine B sulfonyl (DPPE-RhB). This study not only demonstrates the development of excellent SERS substrates with controlled inter-particle coupling but also provides a possibility of studying supported model cell membranes using plasmonic nanostructures.

## **4.2. Materials and Methods**

### **4.2.1. Chemicals**

Silver nitrate ( $\text{AgNO}_3$ , 99+ %), polyvinylpyrrolidone (PVP,  $M_w \sim 55,000$ ), ethylene glycol (EG) and chloroform were purchased from Sigma-Aldrich and used as obtained. Hydrochloric acid (HCl, 38%) and ethanol (95%) were obtained from Anachemia and

Brampton respectively and used without further purification. 1,2-Dipalmitoyl-sn-Glycero-3-Phosphoethanolamine (DPPE) and 1, 2-Dipalmitoyl-sn-Glycero-3-Phosphoethanolamine-N-(lissamine rhodamine B sulfonyl) (ammonium salt, DPPE-RhB) were purchased from Avanti Polar Lipids as a powder and used as provided.

#### **4.2.2. Preparation of nanocubes**

A colloidal solution of silver nanocubes (NC) was synthesized by a modified polyol process developed by Xia *et al.*<sup>25</sup> In a typical synthesis, 5 ml EG was placed in a 100 ml triple necked round bottom flask and heated at 140°C for 1 h under stirring with Teflon coated magnetic stirring bar using a temperature-controlled silicone oil bath. While EG was heated, EG solutions containing AgNO<sub>3</sub> (94 mM) and PVP (147 mM) were prepared. One ml of HCl solution in EG (3 mM), prepared 30 min prior to completion of EG heating time, was added quickly. Ten minutes after the injection of HCl, 3 ml of both AgNO<sub>3</sub> and PVP solutions were added simultaneously in the hot reaction mixture at a rate of ~750 ml/min using glass syringes. The resulting solution was allowed to heat for 26 h under reflux conditions. The final product was cooled to room temperature and subjected to further purification.

#### **4.2.3. Purification of colloidal silver nanocubes**

The as synthesized colloidal nanocubes contained unreacted EG, excess of PVP and nanorods as a by-product. EG and PVP were removed by diluting the colloidal solution with ethanol (1:1 by volume) followed by centrifugation at 12,000 rpm. The precipitate was collected and re-dispersed in ethanol by sonication. This process was repeated 30 times for complete removal of EG and PVP. Silver nanorods were separated from the nanocubes by filtering the pre-washed NC in ethanol using PTFE syringe filters (pore

size: 0.45  $\mu\text{m}$  and 0.22  $\mu\text{m}$ ). The purified silver NC solution was further subjected to washing with chloroform by centrifugation (at least 3 times) prior to the LB film preparation. The final volume of the nanocube solution was 4 ml.

#### ***4.2.4. Preparation of LB monolayers***

NIMA 311D trough, filled with Milli Q water (18.2  $\text{m}\Omega\text{ cm}$ ), was used to prepare the Langmuir monolayers of three different NC samples. In order to create monolayers, appropriate amount of each sample was deposited onto the water surface using a micro syringe. The first sample consisted of 500  $\mu\text{l}$  of pure NC suspended in chloroform. The second sample consisted of 250  $\mu\text{l}$  of NC, 5  $\mu\text{l}$  of DPPE (1 mg/ml) and 5  $\mu\text{l}$  of DPPE-RhB (1 mg/ml) dissolved in chloroform. The third sample consisted of 250  $\mu\text{l}$  of NC and 10  $\mu\text{l}$  of DPPE (1 mg/ml) in chloroform. Each monolayer was left for 20 min to allow chloroform evaporation. Surface pressure of the monolayer was measured with a paper Wilhelmy plate. Before transferring the monolayer onto solid supports several isotherm cycles were performed to anneal the films. Monolayer was transferred onto glass substrates cleaned with piranha solution and subsequently with a mixture of chloroform and methanol, at various surface pressures (0.1, 5, 15, 20, 25 and 35  $\text{mN/m}$ ).

#### ***4.2.5. UV-vis measurement***

UV-vis spectra of the colloidal nanocubes in ethanol and of monolayers deposited on the glass substrates were recorded using Shimadzu, UV-2450 UV-vis spectrophotometer.

#### **4.2.6. Topography measurements**

The topography of the NC monolayer, transferred onto glass substrates at different surface pressures, was obtained using an Ntegra (NTMDT, Russia) atomic force microscope in semi contact mode in air at 23°C with 512×512 points per image. A 100×100 μm<sup>2</sup> scanner (Ntegra) and cantilevers with rotated monolithic silicon tips (125 μm-long, 40 N/m spring constant Tap 300Al, resonance frequency 315 kHz, Budget Sensors) were used for all topographic measurements. The typical scan rate was 0.5 Hz. AFM images were further processed by Nova image processing software.

#### **4.2.7. SERS measurement**

Measurements of SERS spectra were performed using a single grating monochromator (Jobin Yvon, focal length 640 mm) equipped with a liquid nitrogen cooled CCD camera (Princeton Instruments) and a notch filter to remove the excitation wavelength. Argon/Krypton ion laser system (Coherent), operating at 488 nm excitation wavelength with an output power of 20 mW was used for excitation. The spectral resolution of the instrument was ~4 cm<sup>-1</sup>. The accumulation time was 60 s. Final SERS spectrum of each substrate was the average of nine spectra collected in different areas of the sample. The SERS spectra were collected by WinSpec/32 software and further processed by GRAMS/AI spectral data processing software.

### **4.3. Results and Discussion**

#### **4.3.1. Monolayers of silver nanocube substrates**

Various methods can be used for solution- based assembly of metal nanoparticles in two-dimensional structure, including self-assembled monolayers,<sup>26-28</sup> layer-by-layer depositions,<sup>29-31</sup> and others. Recently, Langmuir monolayer technique was shown as a

useful tool in 2D assembly of hydrophobic nanocubes and nanorods.<sup>32,33</sup> By varying the surface pressure in the monolayer, optical properties of the nanoparticles can be adjusted. At the same time, it is difficult to control the morphology of the films composed of nanocubes only because of the tendency of nanocubes to “stick” together even at low surface pressure, due to their hydrophobic nature. It was recently shown that distribution of small gold nanoparticles in a monolayer can be changed if the nanoparticles are mixed with phospholipid molecules.<sup>23</sup> The phase behavior of the lipid monolayers was found to be a critical factor influencing 2D organization of the nanoparticles.

In this present work, therefore, we exploited the phase behavior of different phospholipid molecules in order to achieve control over the properties of silver nanocubes in Langmuir monolayers. We chose two types of phospholipids for the study: a zwitterionic lipid DPPE and its fluorescently labeled analogue DPPE-RhB. The compression isotherms of pure DPPE showed a typical first-order transition from the liquid-expanded to liquid-condensed phase at the surface pressure of  $\sim 15$  mN/m (Figure 4.1, solid line). At the same time, the 1:1 mixture of DPPE/DPPE-RhB mainly exists in the liquid expanded phase at all surface pressures (Figure 4.1, dashed line). Therefore, when silver nanocubes are mixed with these two types of phospholipids the resulting pattern of nanocube organization is likely to be different.

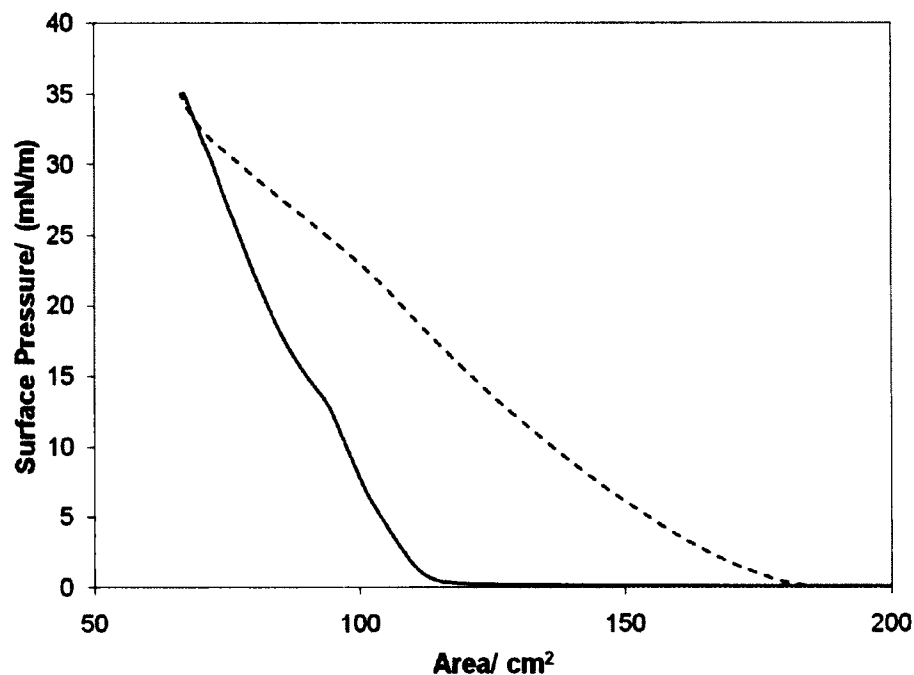


Figure 4.1. Compression isotherm of pure DPPE (solid line) and 1:1 mixture of DPPE/DPPE-RhB (dashed line)

The synthesized NCs are hydrophobic in nature because of the PVP coating on NC surfaces and are capable of forming a stable monolayer at the air/water interface.<sup>22</sup> Figure 4.2 shows the phase diagrams (surface pressure-area isotherms) of pure NC, and NC mixed with phospholipids during isothermal compression. An increase in the surface pressure of the monolayer is accompanied by a change in density and orientation of the nanocubes within the monolayer<sup>33</sup> and reveals three phases of a monolayer i.e.; gas phase, liquid expanded phase and condensed phase.<sup>15</sup> The phase diagram of pure NC monolayer exhibited distinct phase transition (at 15-25 mN/m) from liquid expanded to condensed phase, which is attributed to transition from random distribution to ordered arrangement of nanocubes. For a monolayer of NC with 1:1 mixture of DPPE/DPPE-RhB

the phase diagram is similar to that of pure NC suggesting no lipid induced reorganization of NCs.

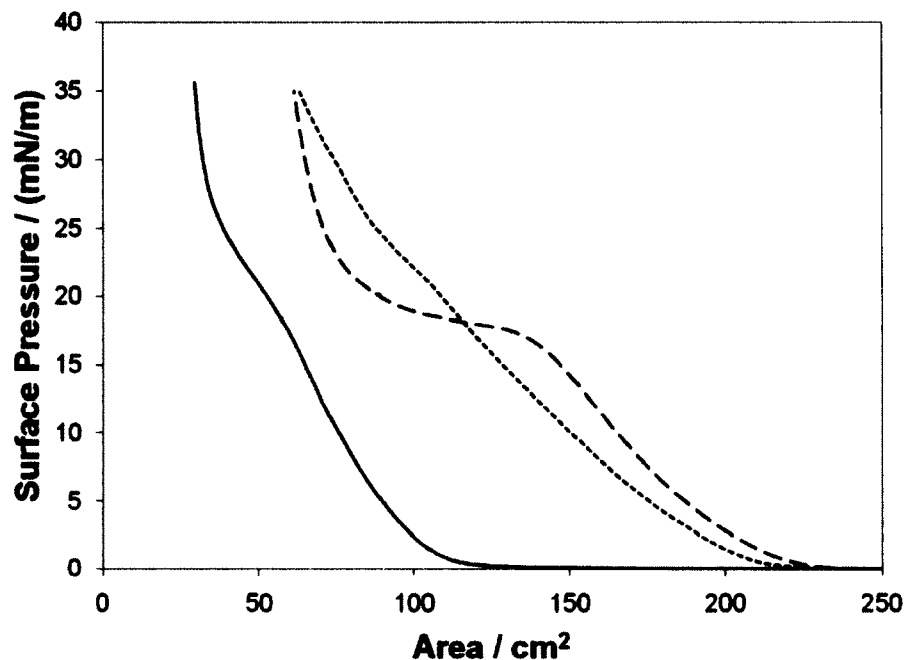


Figure 4.2. Surface pressure-area isotherm of Langmuir monolayers of silver nanocubes (solid line), nanocubes mixed with DPPE (broken line) and nanocubes with DPPE/DPPE-RhB 1/1 mixture (dashed line).

On the contrary, phase diagram of the NCs mixed with pure DPPE exhibited a clear phase transition despite having the same amount of NCs and phospholipids in both mixtures. The observed intense phase transition was due to the local reorganization of both lipids and NCs. Interestingly, the area occupied by NC/DPPE monolayer is larger than that of the monolayer of NC with DPPE/DPPE-RhB at any surface pressure below the phase transition (18 mN/m) but it is smaller above the phase transition. This indicates that orientation of NC was influenced by the phase separation of the DPPE. The transition observed in NC/DPPE mixture occurs at a pressure slightly higher than that of

pure DPPE. Incorporation of labeled lipids (Rhodamine B tagged at lipid head group) into the pure lipids shifted the isotherm to higher surface pressures as well as changed the slope of the isotherm. This indicates miscibility of the labeled lipids with pure phospholipids.

#### **4.3.2. *Surface plasmon resonance spectra***

It is well known that plasmon response of metal nanoparticles is sensitive to its morphology.<sup>34-36</sup> Both theoretical and experimental studies show that polyhedral shaped silver nanocrystals with well-defined facets and corners exhibit distinct optical signatures.<sup>37</sup> Nanocubes, entirely bound by {100} faces, exhibit specific scattering signatures because of the different localized surface plasmon (LSP) modes. Extinction spectra of nanocubes contain several bands with the number and exact position of the bands dependent on the size and local environment of the nanocubes.<sup>38</sup> In this work, colloidal solution of silver nanocubes with nominal edge length 80 nm was synthesized by polyol process as described elsewhere.<sup>25</sup> The morphology of the nanocubes is confirmed by the figure 4.3 UV-vis absorption spectra measured in chloroform. Four overlapping resonance peaks between 300 and 600 nm can be observed with the peaks at 550 and 500 nm assigned to dipolar and quadrupolar modes of LSP respectively, and whose amplitudes are stronger at the corners of the cube.<sup>14</sup> The other two peaks, arising from multipolar modes, correspond to resonances having higher amplitudes at the center of the faces.<sup>14</sup>

2D assembly of nanocubes onto the glass slide altered the shape and position of the surface plasmon resonance peaks as reported previously.<sup>21</sup> Extinction spectra of NC monolayer exhibited five peaks (Figure 4.4). Peaks due to dipolar and quadrupolar

resonances are sharper for the monolayers deposited at low surface pressures (below 15 mN/m) than they are in the solution phase spectra (Figure 4.4).

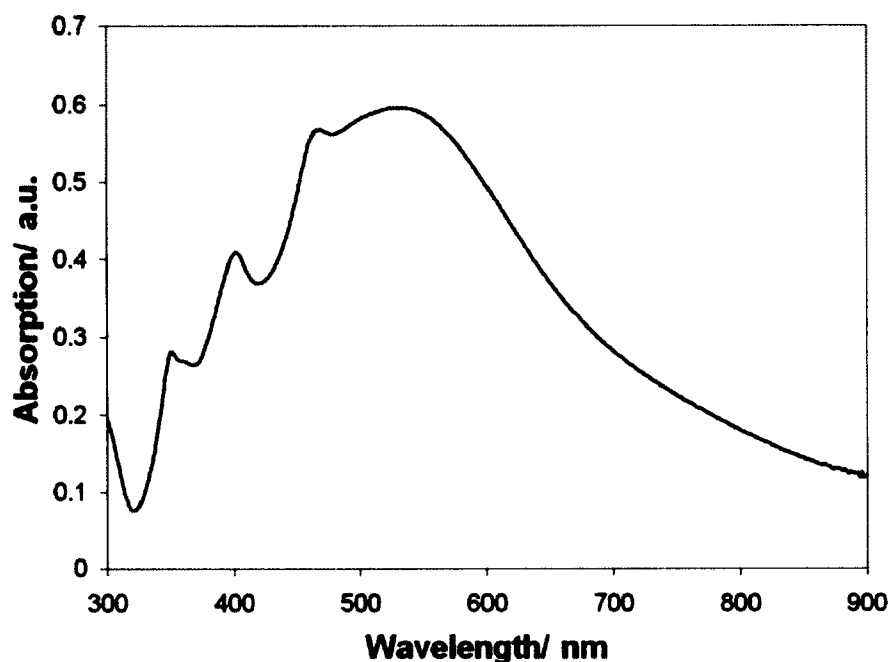


Figure 4.3. UV-vis absorption spectra of colloidal silver nanocubes with edge length 80 nm dissolved in chloroform.

This is because, within a monolayer, nanocubes are in the same plane and the position of individual nanocubes is fixed which results in intense light absorption. However, the extinction peaks that were assigned for a single nanocube overlapped for the monolayer transferred at higher surface pressure, eventually resulting in a single band at  $\sim 420$  nm (Figure 4.4). The notable observation is the decrease in separation between peaks of dipolar (550 nm) and quadrupolar (500 nm) plasmon resonances with increased surface pressure of the monolayer. Therefore, this peak separation can be used as a parameter for

both qualitative and quantitative measure of interparticle separation within the monolayer. Such an understanding can be utilized for fabricating effective SERS substrates. The overlap of different plasmon resonance peaks can be explained as follows: at low pressures the nanocubes are separated enough and without any mutual physical interference but when the surface pressure is raised the nanocubes approach each other at such a distance that their electron distribution is changed which in turn affects their plasmonic response.<sup>39,40</sup> Another indication of increased interparticle coupling is the appearance of a new broad band in the low energy part of the spectrum around 700 nm for the monolayer deposited at higher surface pressure (Figure 4.4). An overall blue shift has been observed for the peaks at 550, 370 and 350 nm; while the peak at 500 nm remains invariant. This blue shift of plasmon resonance absorption was reported in the literature as a result of quantum mechanical effects operated between nanoparticles separated from each other by a distance less than 1 nm.<sup>41</sup>

Unlike substrates of pure NCs, substrates of NCs mixed with phospholipids overlapping of the plasmon resonance peaks was not as significant even at the highest surface pressure (35 mN/m) as shown in figures 4.5 (NC with DPPE/DPPE-RhB) and 4.6 (NC with DPPE). Optical properties are similar for both types of substrates. At the same time the separation between peaks of dipolar (550 nm) and quadrupolar (500 nm) plasmon resonances is greater whereas the intensity of the peak at 700 nm is lower for the substrates of NCs inter dispersed in DPPE/DPPE-RhB compared to the substrates having NCs inter dispersed in pure DPPE, suggesting a stronger degree of inter-particle coupling for the latter.

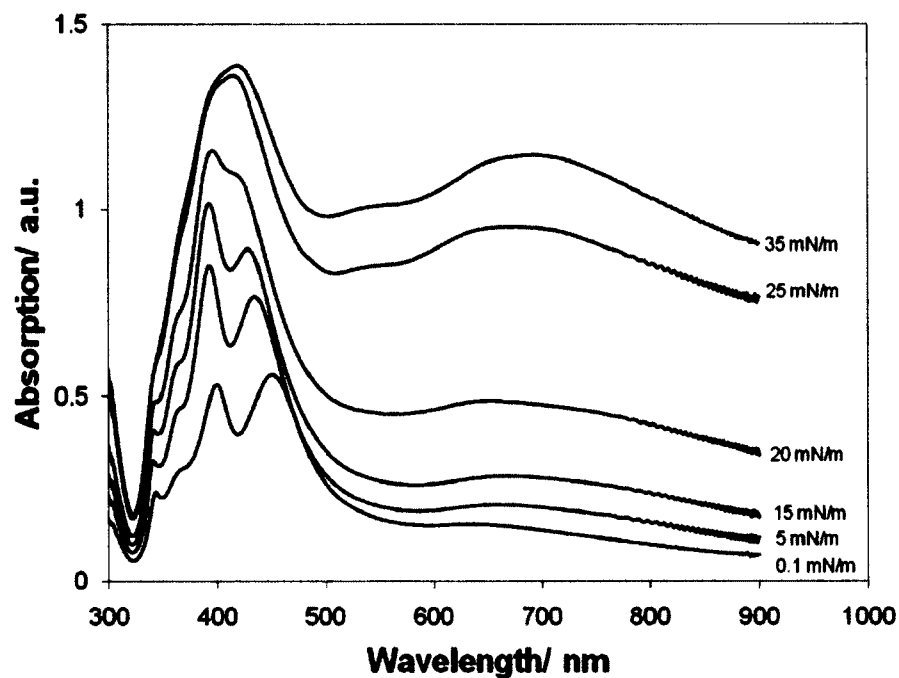


Figure 4.4. UV-vis absorption spectra of silver nanocube substrates deposited at different surface pressure (0.1, 5, 15, 20, 25 and 35 mN/m).

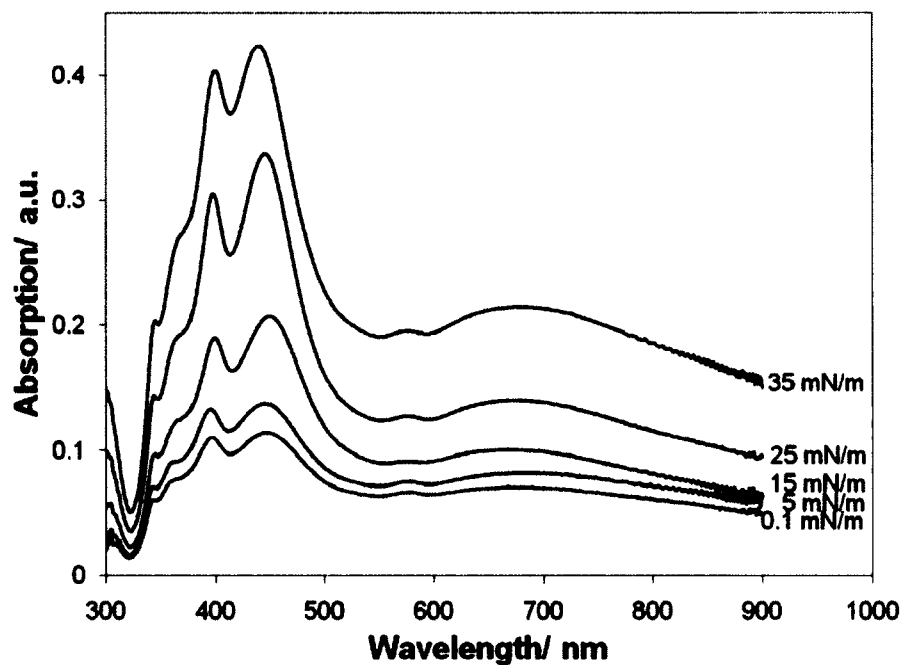


Figure 4.5. UV-vis absorption spectra of substrates prepared from silver nanocubes mixed with DPPE/DPPE-RhB and deposited at different surface pressure (0.1, 5, 15, 25 and 35 mN/m).

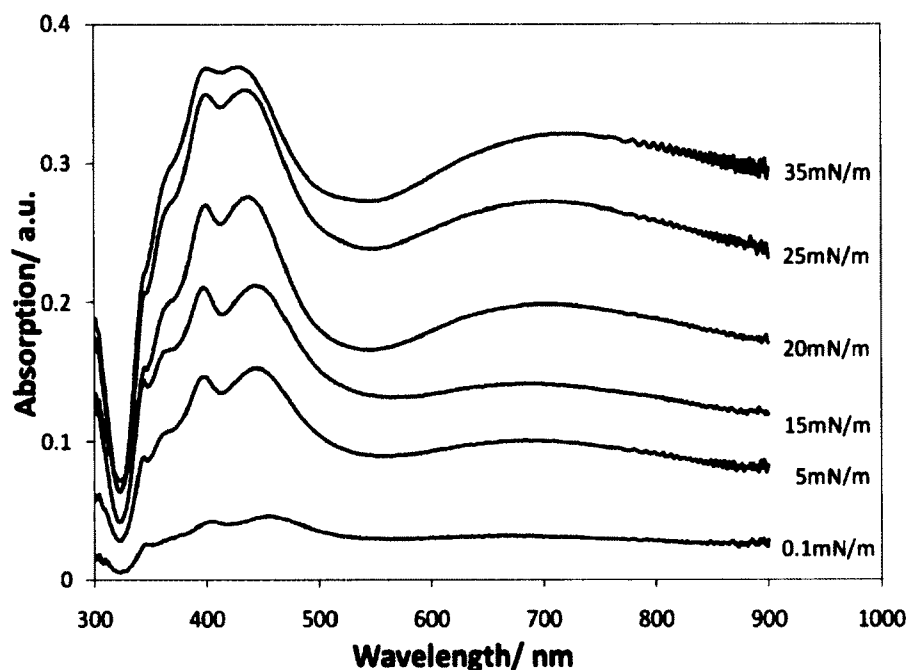


Figure 4.6. UV-vis absorption spectra of substrates prepared from silver nanocubes mixed with DPPE and deposited at different surface pressure (0.1, 5, 15, 20, 25 and 35 mN/m).

#### 4.3.3. Morphology of silver nanocube substrates

Tapping mode AFM images of the NC monolayer were recorded in order to determine the shape and size of the nanocubes as well as the morphology of the NC monolayers deposited at different surface pressures. Figure 4.7 shows AFM topographic images of pure NC monolayer deposited at different surface pressures corresponding to three representative phases. A monolayer transferred at a surface pressure of 0.1 mN/m, which corresponds to the gas phase, consisted of individual nanocubes (there are also some nanorods present, which are usually formed as a by-product during nanocube synthesis) with an average edge length of 80 nm mono-dispersed on the slide. No aggregation of nanocubes was observed. Therefore the topographic image of this

substrate corroborates its extinction spectra having the plasmon resonance peaks of single nanocubes. For a monolayer transferred at surface pressure 15 mN/m, corresponding to the phase transition from liquid condensed to solid phase, well organized aggregates of nanocubes with reduced inter-particle distance can be observed. This 2D organization and higher density of nanocubes are consistent with phase behavior of a monolayer (Figure 4.2) as well as its plasmonic response (Figure 4.4). At this point it is expected that monolayers transferred at any pressure that falls on the solid phase regime of pressure-area isotherm would have more compact structure with the nanocubes in contact with each other. The expected result was confirmed by the Figure 4.7 image showing closely packed 2D structure.

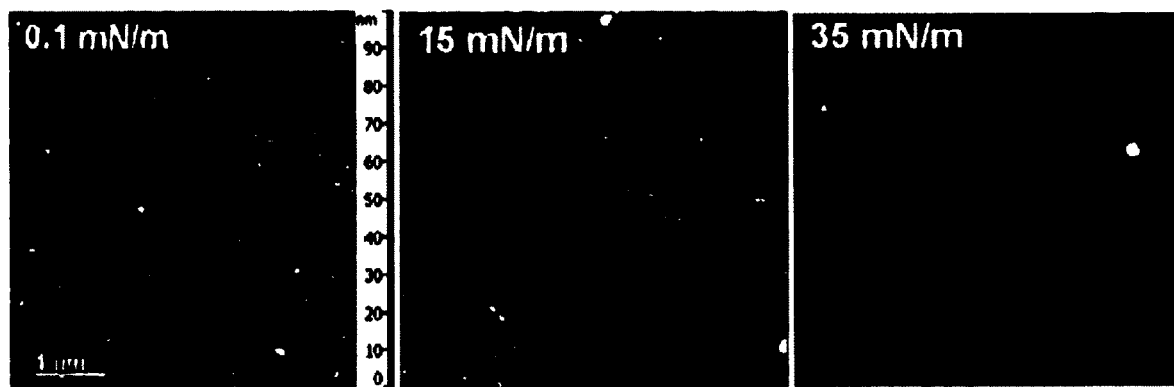


Figure 4.7. AFM topography images of silver nanocube substrates deposited at different surface pressure (0.1, 15 and 35 mN/m).

Inter-particle distance between NCs could not be measured due to the resolution limit imposed by the AFM tip. But we do believe that interparticle distance which is maintained in this structure is sufficient to allow an electron tunneling effect across the junction that blue shifted the plasmon resonance peaks and gave rise to a single band attributed to the dipolar plasmon (Figure 4.4).

It has been reported that a nanoparticle dimer separated by a distance more than 1 nm exhibits a strong EM field at the junction whereas separation of less than 1 nm reduces the electromagnetic field at the junction by the electron tunneling effect.<sup>41</sup> Therefore it is essential to maintain nanoscale separation between the nanoparticles to avoid electron tunneling. Nanocube assembly demonstrated above could maintain the required distance only at lower surface pressures as obvious from their extinction spectra and AFM images (Figure 4.7). Inter-particle distance and organization can be altered by the addition of spacers in the monolayer. For example, previously lipid molecules have been used to organize nanoparticles through phase specific interaction.<sup>23, 24</sup> In this study we used two types of lipids to prevent the NC contact even at high surface pressures: DPPE and DPPE labeled with RhB which also acts as a SERS reporter; and prepared several substrates by transferring a monolayer of NCs and DPPE/DPPE-RhB at different surface pressures. Figure 4.8 shows the AFM topographic images of three of those substrates. It is evident from the images that at sufficiently low pressure (0.1 mN/m) NCs are dispersed mostly as individual particles. Even at 15mN/m a higher density of NC was observed, but they still are well separated from each other. When the surface pressure reaches 35 mN/m, NCs remain monodispersed, with the separation between the NCs however becoming less than the NC size. Compared to the pure NC counterpart, NCs in a complex with DPPE/DPPE-RhB maintained a well-defined inter-particle distance which is also consistent with its extinction spectra (Figure 4.5). The separation can be controlled by varying the amount of the lipid added to the mixture. It is expected that this substrate would exhibit excellent SERS activity.

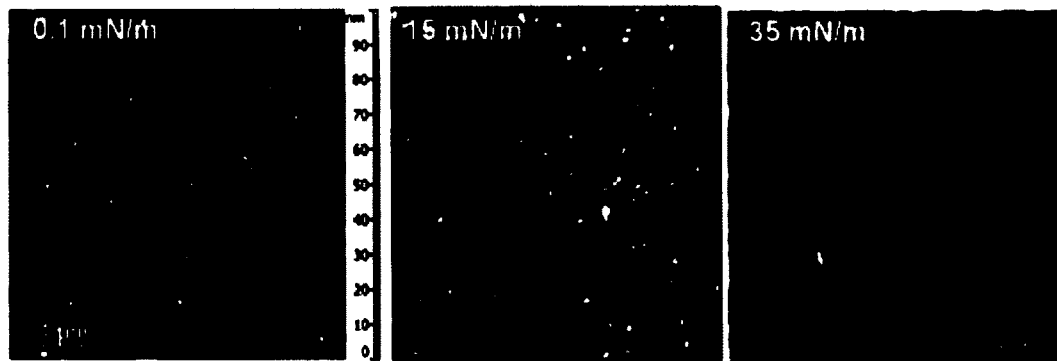


Figure 4.8. AFM topography images of substrates of nanocubes mixed with DPPE/DPPE-RhB and deposited at different surface pressure (0.1, 15 and 35 mN/m).

Furthermore, it was an interest to investigate whether the presence of the label RhB played any role in organizing the NC, so we fabricated substrates consisting of NCs and DPPE lipid at different surface pressures (Figure 4.9). It was observed that at very low pressure 0.1 mN/m, NCs formed small clusters having low density of NCs but as the surface pressure was increased to 15 mN/m, a different morphology was observed. In that case, NCs formed some clusters as well as circular arrays of single NCs with regular gaps between them (Figure 4.9). Ring formation by gold nanoparticles has been reported due to the condensed phase of lipids.<sup>23</sup> Therefore we believe that those domains observed in Figure 4.9 at 15 mN/m are formed by the DPPE condensed phase and NCs organized at the edge of the domain, while single NCs and clusters are formed in the fluid phase of the lipids. At 35 mN/m DPPE is expected to exist exclusively in the condensed phase, leading to complete segregation between the lipid and the NCs. As a result, at this pressure the density of the NCs increased and the condensed phase domains of DPPE broke down and formed islands (Figure 4.9).

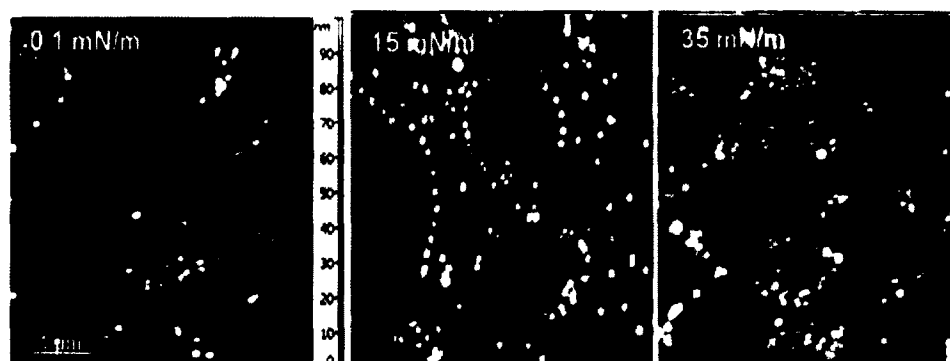


Figure 4.9. AFM topographic images of substrates of nanocubes mixed with DPPE and deposited at different surface pressure (0.1, 15 and 35 mN/m).

This result implied that addition of labeled lipids inhibits lipid molecules from forming a condensed phase due to steric hindrance of bulky head groups.

#### 4.3.4. *SERS Response of the Substrate*

To correlate the SERS activity with the morphology of substrates composed of NCs mixed with labeled phospholipid we collected average SERS spectra of substrates deposited at different surface pressures. The incident laser wavelength was 488 nm which is in resonance with the dipolar band of the nanocubes. Rhodamine B is used as a photo-stable Raman active dye.<sup>42</sup> SERS spectra of different substrates are presented in figure 4.10. The most intense band of RhB appeared at  $1651\text{ cm}^{-1}$  which is due to the C-C stretching vibration of aromatic ring.<sup>43</sup> It is evident from the spectra that there is an increasing trend of the intensity of this band with the increase of the surface pressure of the deposited monolayer. The concentration of the labeled analyte increases with increasing the surface pressure as well which might have a contribution on the total signal enhancement. Therefore to unveil the enhancement mechanism we plotted the intensity variation of the strongest band at  $1651\text{ cm}^{-1}$  as a function of surface pressure of the deposited substrates as well as the intensity of the fluorescence background (Figure 4.

11). The graph shows that both SERS and fluorescence intensities increase with increasing surface pressure. However, the SERS intensity variation is not linear for all the surface pressures and rather shows an exponential increase while the fluorescence intensity remained linear with increasing surface pressure.

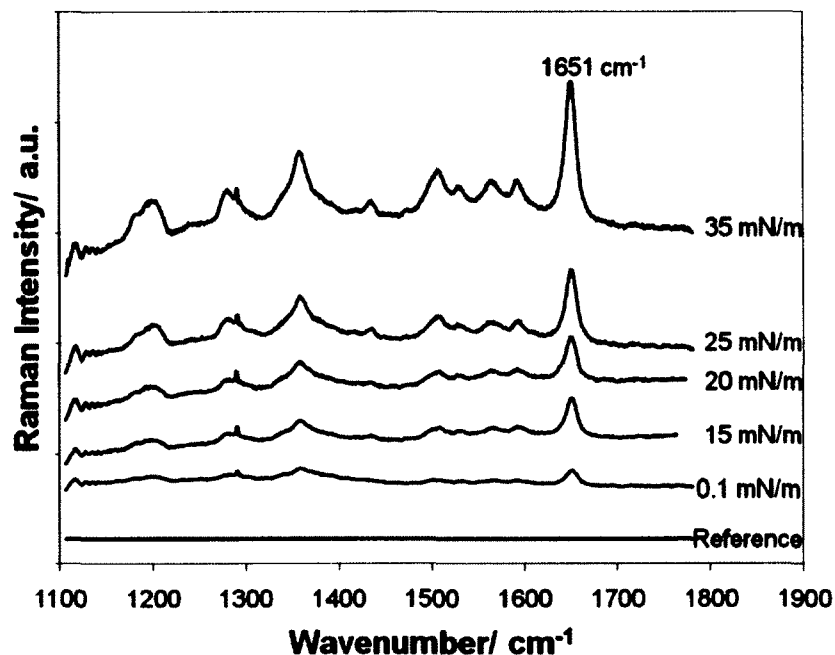


Figure 4.10. Surface enhanced Raman scattering spectra measured for substrates composed of silver nanocubes and DPPE/DPPE-RhB lipid mixture at different surface pressure (0.1, 15, 20, 25 and 35 mN/m). The reference spectrum was measured for DPPE/DPPE-RhB deposited on glass slide without nanocubes at 35 mN/m.

Linear increase of both SERS and fluorescence signal intensities observed at lower surface pressure (below 15mN/m) can be explained by the increase in particle density as well as dye concentration. But the exponential increase is explainable if we considered the additional EM field arising from the “hot spots” existing between the nanocubes at higher surface pressures. Since the lipid molecules are not chemically bonded to NCs, SERS signal enhancement due to chemical mechanism is likely negligible. Therefore,

existence of such hot spots also corroborates with extinction spectra and the morphology of the substrates as stated earlier.

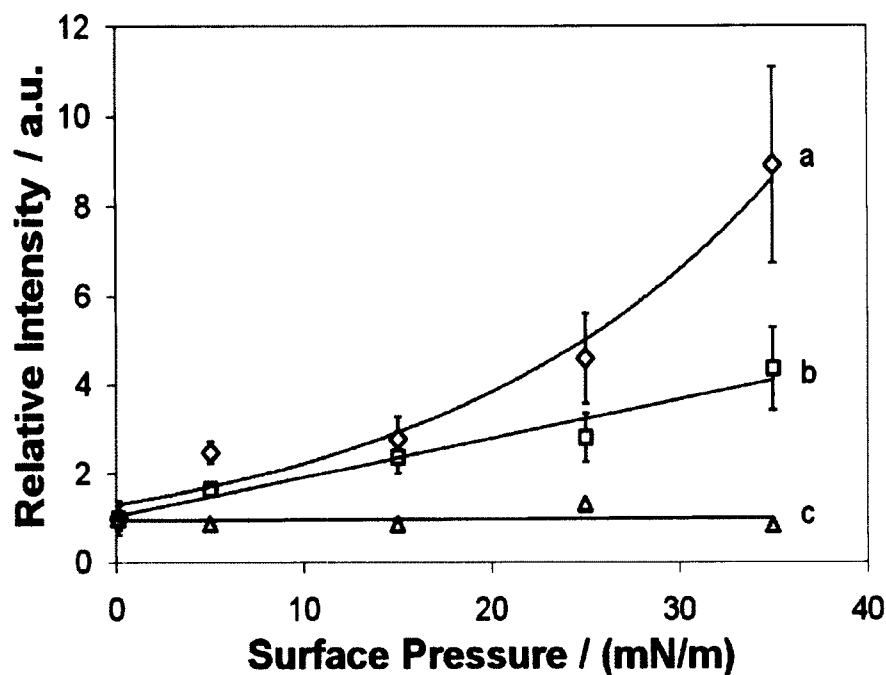


Figure 4.11. Surface pressure dependent relative (to the values at surface pressure of 0.1 mN/m) intensities of (a) SERS peak at  $1651\text{cm}^{-1}$ ; (b) fluorescence, and (c) background intensity measured for DPPE/DPPE-RhB without nanocubes.

#### 4.4. Conclusion

Monolayers of NCs were fabricated using phospholipid matrices of two different compositions to develop better SERS substrates. The fluid phase of the phospholipid allowed NCs to homogeneously distribute within the matrix whereas condensed phase organized NCs in ring like structures. Peak separation between the dipolar and quadrupolar surface plasmon resonances were found to decrease and eventually overlapped with increasing surface pressures. This peak separation can be used as a measure of interparticle coupling. SERS enhancement was found to follow a linear and then exponential increase with surface pressure. The exponential increase is due to

intense EM fields existing in the inter-particle region. Overall, the study shows that properties of SERS substrates can be effectively controlled by carefully choosing phospholipids as well as monolayer formation and transfer conditions.

#### 4.5. References

1. Botti, S.; Cantarini L.; Palucci A. *J. Raman Spectrosc.* **2010**, *41*, 866.
2. Lin, He.; Natan, M. J.; Keating, C. D. *Anal. Chem.* **2000**, *72*, 5348.
3. Fleischmann, M.; Hendra, P. J.; McQuillan, A. J. *Chem. Phys. Lett.* **1974**, *26*, 163.
4. Lee, P.C.; Meisel, D. *J. Phys. Chem.* **1982**, *86*, 3391.
5. Campion, A.; Kambhampati, P. *Chemical Society Reviews* **1998**, *27*, 241.
6. Liz-Marzan, L. M.; Pastoriza-Santos, I.; Barbosa, S. *Langmuir* **2010**, *26*, 14943.
7. Mulvaney, P. *Langmuir* **1996**, *12*, 788-800.
8. Burda, C.; Xiaobo C.; Radha, N.; El-Sayed, M. A. *Chem. Rev.* **2005**, *105*, 1025.
9. Cecilia, N.; Sosa I.O.; Barrera, R.G. *J. phys. Chem.* **2003**, *107*, 6269.
10. Andrea, T.; Prasert, S.; Peidong, Y. *Angew. Chem. Int. Ed.* **2006**, *45*, 4597.
11. Sarah, M.; Willets, K. A. *Nano Lett.* **2010**, *10*, 3777.
12. Farcau, C.; Astilean, S. *J. Phys. Chem. C* **2010**, *114*, 11717.
13. Park, W-H.; Zee, H. K. *Nano Lett.* **2010**, *10*, 4040.
14. Cecilia, N. *J. Phys. Chem. C* **2007**, *111*, 3806.
15. Andrea, T.; Prasert, S.; Peidong, Y. *Nature Nanotechnology* **2007**, *2*, 435.
16. Huebner, U.; Weber, K.; Zeisberger, M.; Popp, J. *Proc. of SPIE* **2010**, *7715*, 771536-1.
17. Song, Y.; Elsayed-Ali, H. *Applied Surface Science* **2010**, *256*, 5961.

18. Zhongming, W.; Wei, X.; Wenping, H.; Daoben, Z. *Langmuir* **2009**, *25*, 3349.
19. Peidong, Y.; Kim, F. *Chem. Phys. Chem.* **2002**, *3*, 503.
20. Yuan, C.; Furlong, J.; Burgos, P.; Linda, J. *J. Biophysical J.* **2002**, *82*, 2526.
21. Mahmoud, M. A.; Tabor, C.E.; El-Sayed, M.A. *J. Phys. Chem C* **2009**, *113*, 5493.
22. Mahmoud, M. A.; El-Sayed, M. A. *J. Phys. Chem. C* **2008**, *112*, 14618.
23. Mogilevsky, A.; Roman, V.; Jelinek R. *Langmuir* **2010**, *26*, 7893.
24. Tang, N. Y-Wa.; Badia, A. *Langmuir* **2010**, *26*, 17058.
25. Sang, H. I.; Yun, T. L.; Benjamin, W; Xia, Y. *Angew. Chem. Int. Ed.* **2005**, *44*, 2154.
26. Kumara, M. T.; Brian, C. T.; Muralidharan, S. *Chem. Mater.* **2007**, *19*, 2056.
27. Zhenlin, W.; Chan, C. T.; Weiyi, Z.; Naiben, M.; Ping, S. *Phys. Rev. B* **2001**, *64*, 113108.
28. Kalsin, A. M.; Fialkowski, M.; Paszewski, M.; Smoukov, S. K.; Grzybowski, B. A. *Science* **2006**, *312*, 420.
29. Chanwoo, L.; Inpyo, K.; Hyunjung, S.; Sanghyo, K.; Jinhan, C., *Nanotechnology* **2010**, *21*, 185704.
30. Olaf, S.; Oxana, I.; Matthias, H.; Manesh, G.; Christiane, A. H. *Langmuir* **2010**, *26*, 15219.
31. Xingjie, Z.; Zhaohui, Su. *Thin Solid Films* **2010**, *518*, 5478.
32. Andrea, T.; Franklin, K.; Christian, H.; Joshua, G.; Rongrui, H.; Yugang, S.; Xia, Y.; Peidong, Y. *Nano Lett.* **2003**, *3*, 1229.
33. Andrea, T.; Jiaying H.; Peidong, Y. *Accounts of Chemical Research* **2008**, *41*, 1662.

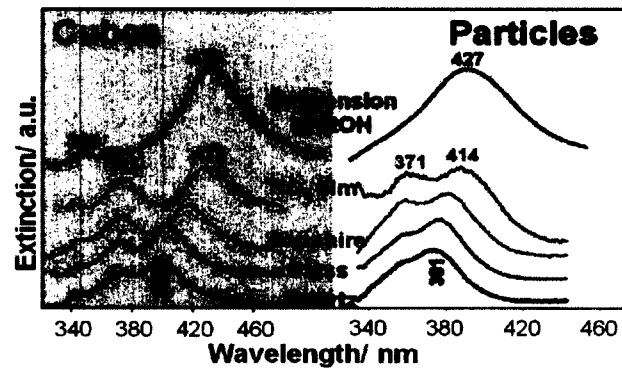
34. Haynes, C. L.; Van Duyne, R. P. *J. Phys. Chem. B* **2001**, *105*, 5599.
35. Kelly, K. L.; Coronado, E.; Zhao, L. L.; Schatz, G. C. *J. Phys. Chem. B* **2003**, *107*, 668.
36. Jin, R.; Cao, Y. C.; Hao, E.; Metraux, G. S.; Schatz, G. C.; Mirkin, C. A. *Nature* **2003**, *425*, 487.
37. Xia, Y.; Benjamin, J. W.; Sang, H. I.; Andrew, S.; Joseph M. *J. Phys. Chem. B*, **2006**, *110*, 15666.
38. Jeffrey, M.M.; Wang, Y.; Van Duyne R. P.; George, C. S. *J. Phys. Chem. C*, **2009**, *113*, 2731.
39. Halas, N.J.; Lassiter J. B.; Daniel, W. B. *Nano Lett.* **2008**, *8*, 1212.
40. Nordlander, P.; Stephan, L.; Yanpeng, Wu. *ACS Nano*. **2010**, *4*, 4657.
41. Zuloaga, J.; Prodan, E.; Nordlander, P. *Nano Lett.* **2009**, *9*, 887.
42. Joseph, R. L.; Ignacy, G.; Chris, D. G. *Journal of Fluorescence*, **2002**, *12*, 299.
43. Peter, H.; Manfred, S. *J. Phys. Chem.* **1984**, *88*, 5935.

## Chapter 5

---

### Optimizing Refractive Index Sensitivity of Supported Silver Nanocube Monolayers

J. Phys. Chem. C 2012 (In Press)



## 5.1. Introduction

Noble metal nanostructures have been of great interest due to their unique optical properties useful in numerous applications. Recently significant progress has been made in the development of nanoparticle fabrication methods<sup>1</sup> and theory,<sup>2</sup> leading to the discovery of novel phenomena. Giant enhancement of local electric field near the surface of plasmonic nanoparticles due to the excitation of their localized surface plasmon resonances (LSPR) has led to increase in optical response from molecules in the vicinity of such nanoparticles, resulting in surface enhanced Raman,<sup>3,4</sup> fluorescence,<sup>5-8</sup> IR<sup>9</sup> or second harmonic generation<sup>10</sup> phenomena. The localized electric field is also very sensitive to the refractive index change in the environment, making LSPR an excellent sensing platform.<sup>11-13</sup> In addition, interacting plasmonic nanoparticles have recently been shown to possess some novel properties, such as collective plasmonic modes,<sup>14,15</sup> Fano resonances,<sup>16</sup> etc., leading to improvement of sensing devices,<sup>11,16</sup> fabrication of nano-antennas,<sup>17,18</sup> and nano-rulers.<sup>19</sup>

Size, shape, material and dielectric environment control the plasmonic signature of metal nanoparticles.<sup>20-25</sup> As the nanoparticles become bigger, in addition to a single dipolar LSPR mode, higher order plasmonic modes appear.<sup>1,26,27</sup> It is well recognized that interactions with a support (dielectric or conducting) as well as inter-particle separation and local order are crucial factors in controlling the plasmonic signature. LSPR- induced charges in a dielectric substrate disturb the nanoparticles' electric field leading to splitting of a single dipolar plasmonic mode into two.<sup>28-32</sup> For spherical particles these two modes correspond to dipolar oscillations with orthogonal polarizations.<sup>28</sup> For nanocubes,

however, substrate leads to plasmon mode hybridization resulting in two bands- dipolar and quadrupolar with corresponding charge oscillations located at the opposite sides of the nanocube.<sup>29-32</sup> The wavelength difference between the two bands was found to be greater than for the spherical particles, dependent on the size,<sup>32</sup> edge sharpness,<sup>29</sup> and separation from the substrate.<sup>29,32</sup> The bands show strong dependence on the refractive index of the medium.

Detailed investigations of the plasmon mode hybridization have been performed at the single supported nanoparticle level.<sup>29-31</sup> Such approach provides certain advantages over the ensemble measurements, due to the increased sensitivity and also narrower plasmonic bands.<sup>33</sup> However, single nanoparticle measurements are difficult to perform when the size is smaller than 20 nm.<sup>13</sup> Also, for routine and consistent measurements it is important to develop substrates that can be easily and reproducibly fabricated.<sup>12,13</sup> Additionally, certain plasmonic phenomena can be only observed for interacting nanoparticles. Therefore, it is important to investigate the unique properties, particularly refractive index sensitivity of silver nanocubes in monolayers where the degree of interparticle coupling can be controlled. To the best of our knowledge, no detailed studies of this kind have been performed. Although the single nanoparticles usually have narrower bands, if the sample has high monodispersity in particle size the plasmonic band width for the ensemble can be narrow as well. In the present work we systematically investigated the refractive index sensitivity of mono-disperse silver nanocubes, both in suspension and in monolayers transferred onto a solid support by the Langmuir technique as a function of nanocube size, spacing, as well as dielectric properties of a substrate.

## 5.2. Materials and Methods

### 5.2.1. Chemicals

Silver nitrate ( $\text{AgNO}_3$ , 99+ %), polyvinylpyrrolidone (PVP,  $M_w \sim 55,000$ ), anhydrous 99.8% ethylene glycol (EG), sodium sulfide and chloroform were purchased from Sigma-Aldrich and used as obtained. Hydrochloric acid (HCl, 38%) and ethanol (95%) were obtained from Anachemia and Brampton respectively and used without further purification. 1,2-Dipalmitoyl-sn-Glycero-3-Phosphoethanolamine-N-(lissamine rhodamine B sulfonyl) (ammonium salt, DPPE-RhB) was purchased from Avanti Polar Lipids as a powder and used as provided.

### 5.2.2. Preparation of nanocubes

Silver nanocubes (NC) with an edge length of 40 nm were synthesized according to the procedure described in the literature.<sup>34</sup> Typically, a 100 ml round bottom flask containing 35 ml of EG and a clean stir bar was placed in a silicone oil bath set to 150°C and allowed to heat for 1 hour. Using a glass syringe 5 ml of EG containing 0.4 g of dissolved PVP was injected. Five minutes later using a micropipette, 400  $\mu\text{l}$  of 3 mM sodium sulfide dissolved in EG was added. After an additional 5 minutes 2.5 ml of 282 mM silver nitrate dissolved in EG was injected slowly using a glass syringe. Upon addition of the silver nitrate the solution immediately turned black and slowly became a transparent yellow, then changed to an ochre color while some plating in the flask occurred. The reaction was monitored by periodically taking small aliquots out of the reaction flask using a pasture pipette and dispersing it in a cuvette filled with ethanol for UV-visible spectroscopy. The reaction was quenched by placing the flask in an ice bath when the appearance of a small but distinct peak at 350 nm was observed in the spectra.

Cubes with edge lengths of 80 and 130 nm: a colloidal solution of silver NC was synthesized by a modified polyol process developed by Xia *et al.*<sup>35</sup> In a typical synthesis, 5 ml EG was placed in a 100 ml triple necked round bottom flask and heated at 140°C for 1 h under stirring with Teflon coated magnetic stirring bar using a temperature-controlled silicon oil bath. While EG was heated, EG solutions containing AgNO<sub>3</sub> (94 mM) and PVP (147 mM) were prepared. One ml of HCl solution in EG (3 mM), prepared 30 min prior to completion of EG heating time, was added quickly. Ten minutes after the injection of HCl, 3 ml of both AgNO<sub>3</sub> and PVP solutions were added simultaneously in the hot reaction mixture at a rate of ~750 ml/min using glass syringes. The resulting solution was allowed to heat for 26 h under reflux conditions. The final product was cooled to room temperature and subjected to further purification.

### ***5.2.3. Purification of colloidal silver nanocubes***

The as synthesized colloidal nanocubes contained unreacted EG, excess of PVP and nanorods as a by-product. EG and PVP were removed by diluting the colloidal solution with ethanol (1:1 by volume) followed by centrifugation at 12,000 rpm. The precipitate was collected and re-dispersed in ethanol by sonication. This process was repeated 30 times for complete removal of EG and PVP. Silver nanorods were separated from the nanocubes by filtering the pre-washed NC in ethanol using PTFE syringe filters (pore size: 0.45 μm and 0.22 μm). The purified silver NC solution was further subjected to washing with chloroform by centrifugation (at least 3 times) prior to the LB film preparation. The final volume of the nanocube solution was 4 ml.

#### **5.2.4. Preparation of LB monolayers**

Nanocube substrates were prepared according to the procedure reported previously.<sup>36</sup> Briefly, NIMA 311D trough, filled with Milli Q water (18.2 m $\Omega$  cm), was used to prepare the Langmuir monolayers of different NC samples. In order to form monolayers, appropriate amount of each sample was deposited onto the water surface using a micro syringe. Each monolayer was left for 20 min to allow chloroform evaporation. Surface pressure of the monolayer was measured with a paper Wilhelmy plate. Before transferring the monolayer onto solid supports several isotherm cycles were performed to anneal the films to the maximum pressure of 20-25 mN/m. Monolayers of pure nanocubes and nanocube/lipid mixtures were transferred onto substrates cleaned with aqua regia and subsequently with a mixture of chloroform and methanol, at various surface pressures by vertical upward dipping at 2 mm/min at room temperature (usually 25-30 °C).

#### **5.2.5. UV-vis measurement**

UV-vis spectra of the colloidal nanocubes in ethanol and of monolayers deposited on the substrates were recorded using Shimadzu, UV-2450 UV-vis spectrophotometer. Spectra were analyzed using GRAMS/AI spectral data processing software. Spectral deconvolution was performed using appropriate number of mixed Gaussian- Lorentzian functions and a linear baseline to achieve the best fit to the original trace while minimizing  $\chi^2$  values. To determine the refractive index sensitivities (RIS), silver nanocubes samples were dispersed in water-ethylene glycol mixture solutions with varying volume percentages, and the extinction spectra were measured. The refractive indices of the mixtures were calculated from the volume percentages of the ingredients

according to the Lorentz-Lorenz equation.<sup>37</sup> The refractive indices of the pure solvents were 1.3334 and 1.4318, for water and EG, respectively.<sup>37</sup> The plasmon shifts were plotted as a function of the refractive index. The refractive index sensitivities were obtained from the slope of the linear fitting. The figures of merit (FOM) were calculated as ratios of RIS to the full width at half maximum (FWHM) for the peaks obtained from the peak fitting procedure.

### ***5.2.6. Topography measurements***

The topography of the NC monolayer, transferred onto glass substrates at different surface pressures, was obtained using an Ntegra (NTMDT, Russia) atomic force microscope in semi contact mode in air at 23°C with 512×512 points per image. A 100×100  $\mu\text{m}^2$  scanner (Ntegra) and cantilevers with rotated monolithic silicon tips (125  $\mu\text{m}$ -long, 40 N/m spring constant Tap 300Al, resonance frequency 315 kHz, Budget Sensors) were used for all topographic measurements. The typical scan rate was 0.5 Hz. AFM images were further processed by Nova image processing software.

## **5.3. Results and Discussion**

### ***5.3.1. Effect of nanocube size on the refractive index sensitivity***

Three batches of silver nanocubes were prepared in this work with the edge lengths of 40, 80 and 130 nm. Figure 5.1 shows representative AFM images of monolayers deposited by the Langmuir technique at low surface pressures, as well as histograms of height distribution in the samples. After purification by numerous rounds of centrifugation and filtration, the resulting nanocube samples were of high monodispersity, without nanorod impurities and with a size variation less than 10%. Inspection of the nanocube samples using SEM demonstrated that cubes had well defined

sharp edges. As a result of such high monodispersity UV- vis spectra show characteristic and narrow plasmonic extinction bands (Figure 5.2). Extinction spectrum of the 40 nm nanocube suspension shows two sharp peaks (Figure 5.2A): a dipolar at 428 nm and a peak at 350 nm, often assigned to octupolar plasmonic mode.<sup>38</sup>

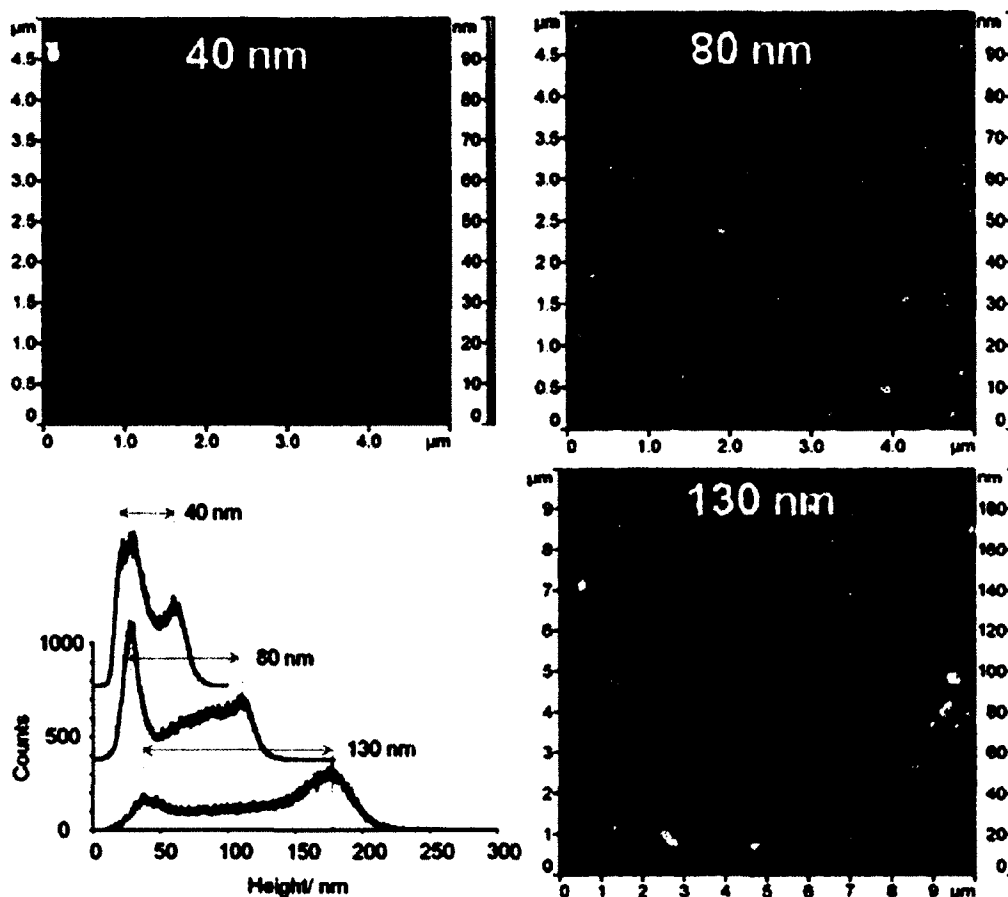


Figure 5.1. AFM topographic images of supported nanocube substrates prepared by Langmuir monolayer technique at low (0.1-1 mN/m, 15 mN/m for 130 nm cubes) surface pressure. The histograms show height distribution in the samples (bottom, left).

As the size of the nanocubes increases, new bands appear and the dipolar shifts to lower energies. It has been found that when the size of silver nanocubes exceeds 40-50 nm, a quadrupolar peak appears.<sup>1,39</sup> Therefore, for 80 nm cubes in addition to a dipolar peak at 530 nm, we observed a quadrupolar mode at ~450 nm and a peak at ~400 nm

which is often assigned to a quadrupolar mode,<sup>38</sup> but also to mixed dipole/quadrupole plasmonic mode,<sup>27</sup> and a peak at 350 nm (Figure 5.2B). For 130 nm cube sample the dipolar peak is found at ~680 nm, the first quadrupolar at 530 nm, the second quadrupolar (hybrid dipolar/quadrupolar) at ~404 nm and a peak at 350 nm (Figure 5.2C).

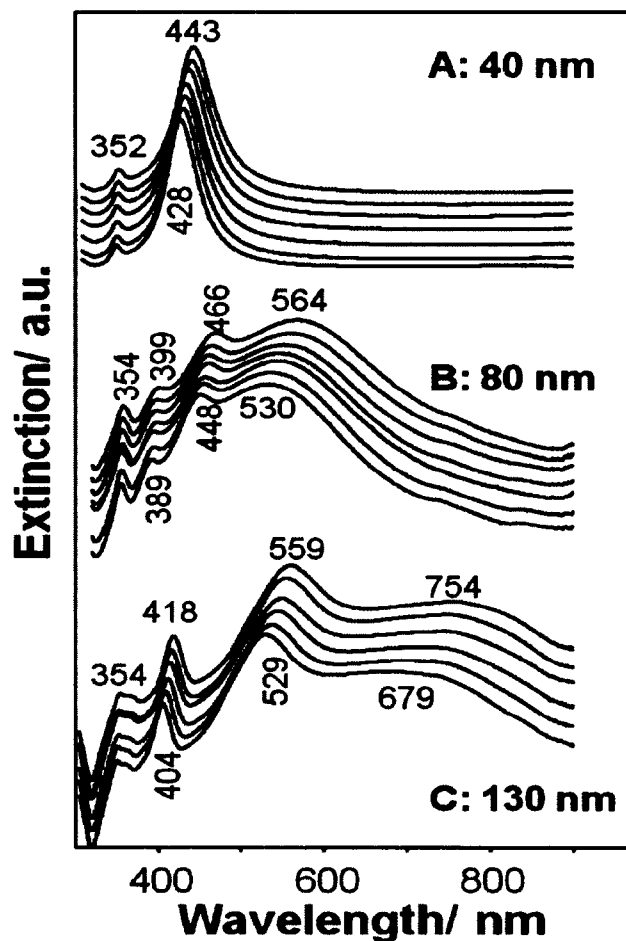


Figure 5.2. Extinction spectra of colloidal suspensions in different water/ethylene glycol solutions for A: 40 nm, B: 80 nm, and C: 130 nm nanocubes. The spectra were measured in water (bottom spectrum in series), followed by water: EG 4:1, ethanol (40 and 80 nm only), water: EG 3:2, 2:3, 1:4, and pure EG.

Peak fitting of the spectra was performed using mixed Gaussian-Lorentzian functions. The peaks half widths were found to increase with the nanocubes size. For

example, the FWHM of the dipolar peak increases from 55 to 235 to 330 nm for 40, 80, and 130 nm nanocubes respectively (Table 5.1). The same trend was observed for the quadrupolar peaks.

Table 5.1. Refractive indices sensitivities of silver nanocubes in suspension.

Size/ nm	Plasmon peak Position $\lambda$ /nm	Full width at half maximum/nm	Refractive index sensitivity(nm/ RIU)	Figure of merit
40	428	55	176+/-14	<b>3.3</b>
	350	15	29+/-1.6	1.88
80	530	235	361+/-50	<b>2.43</b>
	448	65	158+/-42	1.54
	389	40	74+/-26	1.83
	350	22	20+/-9	0.9
130	679	330	480+/-74	1.46
	529	138	304+/-29	2.2
	404	27	125+/-14	<b>4.55</b>

Extinction spectra of silver nanocubes in suspension were further measured in different solvent mixtures with increasing refractive index to probe the refractive index sensitivity. Figure 5.2 series consist of an extinction spectra obtained in water (bottom spectrum in the series) followed by water: EG 4:1 mixture, ethanol, water: EG 3:2, 2:3, and 1:4 mixtures, and pure EG. The plot of plasmonic shifts versus corresponding refractive index can be seen in figure 5.3. As expected, the positions of the plasmonic bands red shift as the refractive index of the solvent increases. The calculated RIS are

listed in table 5.1. The highest RIS was determined for the dipolar peak of 130 nm nanocubes- 480 nm/RIU. Figures of merit, measured as a ratio of RIS to the peak half width, on the other hand decreased with size (Table 5.1). The highest figure of merit of 4.55 was determined for the peak attributed to the dipolar/quadrupolar mixed plasmonic mode of the 130 nm cubes.

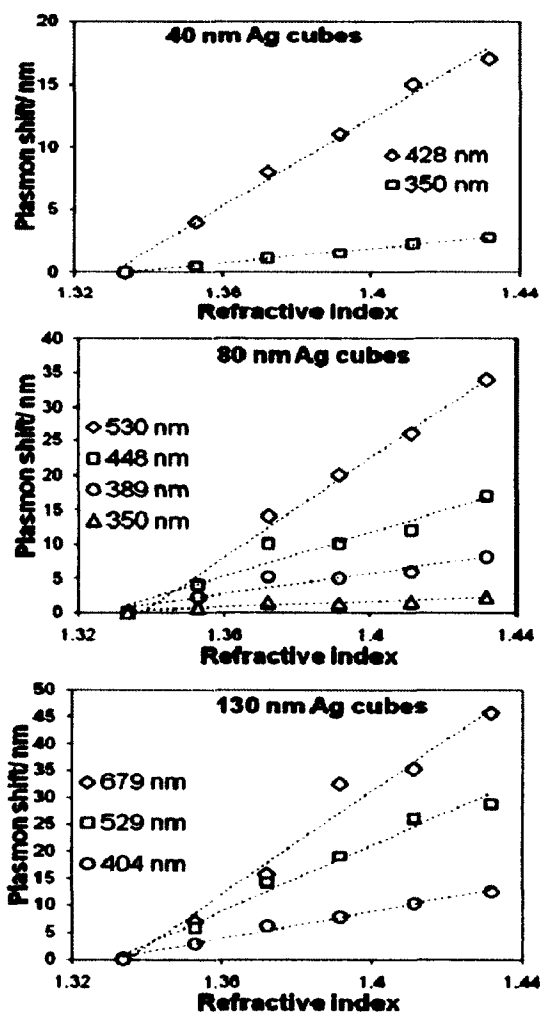


Figure 5.3. Plasmonic shifts as functions of refractive index for silver nanocube suspensions.

Data presented here are consistent with recently published results.<sup>38</sup> For example, RIS of  $336\pm 15$  nm/RIU measured for the dipolar band of  $84\pm 6$  nm Ag nanocubes,<sup>38</sup> is very close to  $360\pm 50$  nm/RIU obtained in this work for  $80\pm 5$  nm cubes. RIS for other plasmon modes are also similar. However, the figures of merit do not match very well, likely due to variations in the edge and corner sharpness of the nanocubes, as well as different peak fitting procedures used.

### ***5.3.2. Refractive index sensing by supported vs. suspended nanocubes***

Often applications require ensembles of nanoparticles to be deposited on a solid support for better reproducibility and control.<sup>12,13</sup> Interaction with a solid support, however, is known to alter the plasmonic optical properties of metal nanoparticles, such as refractive index sensitivity.<sup>30</sup> To test the effect of solid dielectric support on the refractive index sensing by nanocube ensembles of different size, we used Langmuir monolayer technique to deposit monolayer of NC on different substrates. The technique enables facile and reproducible fabrication of substrates with controlled interparticle separation and density that is dependent on the surface pressure at which the monolayer is transferred.<sup>36</sup> We first looked at the substrates prepared at low surface pressure to minimize the interparticle interactions and to facilitate the comparison with nanocubes in suspension. At such low pressure the dipole-dipole near-field coupling between adjacent nanocubes is weak, as can be monitored using a low energy broadband in the spectra (for 130 nm cubes sample such conditions maintained even at 15 mN/m). Figure 5.4 shows extinction spectra of supported nanocube substrates for three sizes in air (lowest, separate spectra in the series) and immersed in liquids with an increasing refractive index. When deposited on a solid support the spectra change considerably compared to those in

colloidal suspension. For the largest 130 nm nanocubes studied, the dipolar peak shifts from 680 to 477 nm, the first quadrupolar shifts from 529 to 435 nm, the second quadrupolar/ mixed peak from 400 to 369 nm and a peak at 350 to 340 nm. The same trend is observed for the 80 nm sample, with all four bands blue shifted.

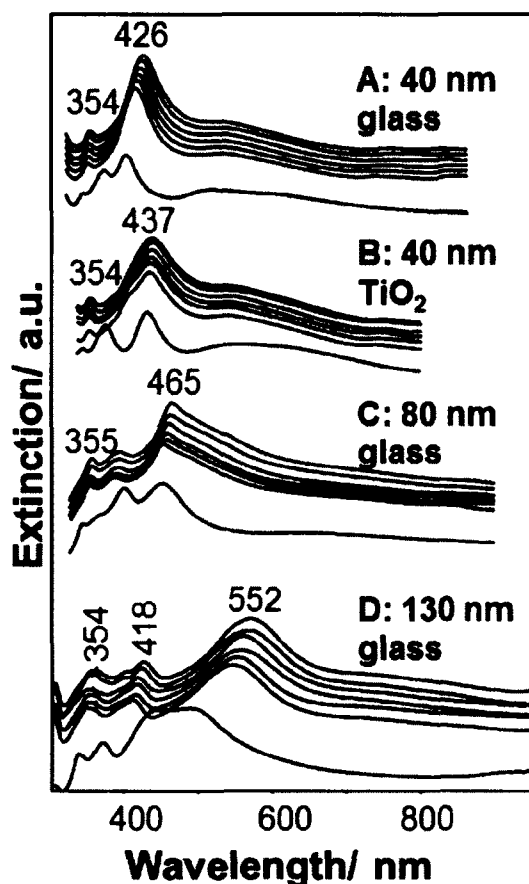


Figure 5.4. Extinction spectra of supported nanocube monolayers in air (lowest spectra in series) and immersed in different water/ ethylene glycol solutions for A: 40 nm on a glass substrate, B: 40 nm on a glass substrates coated with 5 nm  $\text{TiO}_2$  film; C: 80 nm, and D: 130 nm nanocubes. The spectra were measured in water (first spectra in series), followed by water: EG 4:1, water: EG 3:2, 2:3, 1:4, and pure EG.

For the 40 nm cubes however, the substrate induced a more dramatic spectral change. For the dipolar peak at 428 nm plasmon mode hybridization takes place resulting in two peaks: dipolar at  $\sim 400$  nm (FWHM  $\sim 35$  nm) and quadrupolar at  $\sim 374$  nm (FWHM  $\sim 20$  nm). Unlike larger nanocubes, the quadrupolar mode can not be excited in 40 nm

cubes in a suspension.<sup>1,39</sup> However, when the substrate is present, plasmon induces charge oscillations in the substrate which act to disturb the electric field in the nanocube.<sup>30,31</sup> As a result, two new modes can be excited: a lower energy dipolar mode with charge oscillating at the side of the nanocube near the substrate, and a higher energy quadrupolar mode with corresponding charge oscillations at the nanocube side away from the substrate. The wavelength difference between the two peaks increases with the substrate refractive index (will be discussed later).

The half widths of all bands decrease for supported nanocubes due to introduction of a preferred orientation with all the cubes aligned in the same plane. It is possible however that occasional dimer formation broadens the spectra in solutions. The measured FWHM for the dipolar bands are 35 nm for 40 nm cubes, 80 nm for 80 nm cubes, and 130 nm for 130 nm (Table 5.2). This is about half the widths measured for the suspensions, which is useful for increasing the FOM values.

Table 5.2. Refractive index sensitivities of supported silver nanocube monolayers on glass at low<sup>a</sup> surface pressure.

Size/nm	Plasmon peak Position $\lambda$ /nm	Full width at half maximum/nm	Refractive index sensitivity(nm/RIU)	Figure of merit
40	420	44	93+/- 11	2.11
	352	13	31+/- 2	<b>2.4</b>
40, TiO <sub>2</sub>	420	54	57+/- 5	1.05
	400	27	90+/- 5	<b>3.3</b>
	350	10	29+/- 1.1	2.9
80	480	159	73+/- 27	0.46
	450	42	89+/- 20	<b>2.12</b>
	380	46	46+/- 13	1.0
	350	23	39+/- 10	1.69
130	700	n.d. <sup>b</sup>	n.d.	n.d.
	527	128	155+/-32	1.2
	409	30	77+/- 11	<b>2.6</b>
	350	32	35+/- 3	1.12

(<sup>a</sup> Surface pressure between 0.2 mN/m and 1 mN/m. For 130 nm nanocubes surface pressure was 15 mN/m. <sup>b</sup> Not determined)

When the slides with glass-supported nanocube monolayers are immersed into solutions for measuring the refractive index response the spectra undergo significant changes. In all cases red-shifting of the plasmonic bands was observed. For the 40 nm cubes the plasmonic mode hybridization disappeared, and a single band at 415 nm emerges when the substrate is immersed in water (Figure 5.4 A, lower spectrum). For the 80 nm substrate the dipolar band broadens with FWHM increasing to 160 nm and red-shifts from 450 to ~480 nm, and the quadrupolar band remains fairly sharp with 45 nm FWHM and red-shifts from 400 to ~450 nm. For the biggest nanocubes the dipolar peak broadens to more than 200 nm FWHM and shifts to ~700 nm, the quadrupolar peak- to 530 nm with FWHM of ~130 nm. When plasmonic shifts are plotted as functions of refractive index (Figure 5.5), refractive index sensitivities as well as FOM can be

calculated (Table 5.2). RIS values are considerably smaller for the supported nanocubes, than in suspension, particularly for the dipolar modes.

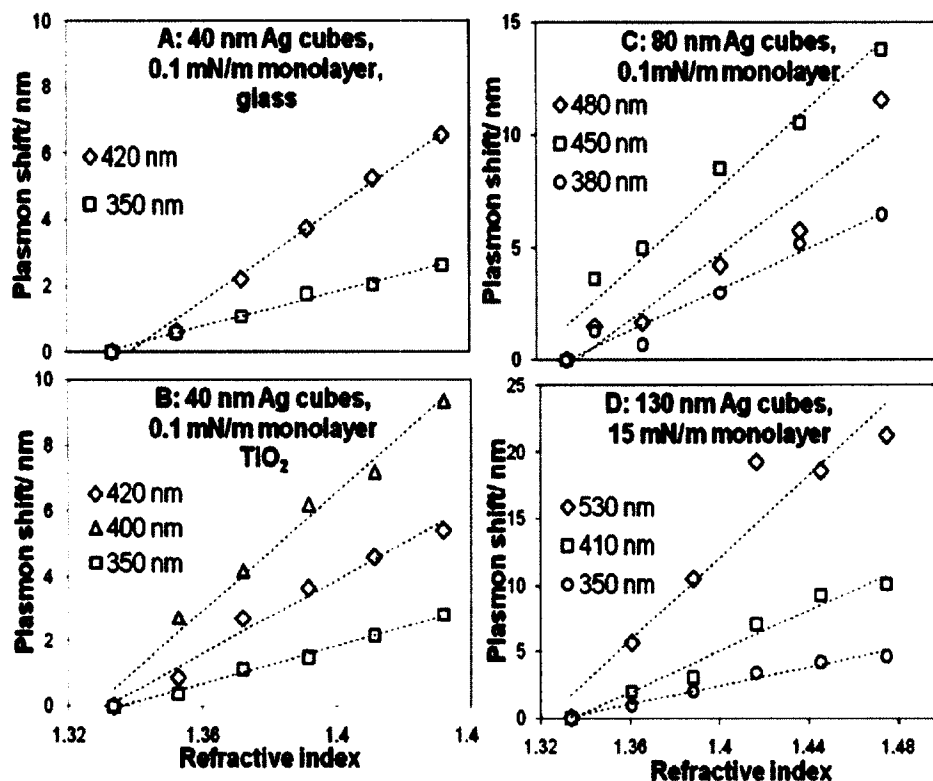


Figure 5.5. Plasmonic shifts as functions of refractive index for supported silver nanocubes.

The FOM are smaller as well, but to a lesser extent than RIS, due to the sharper band profiles for the supported nanocubes. The reduced sensitivity of the dipolar mode of supported nanocubes to the solution refractive index change is a direct result of the charge oscillations corresponding to this mode near the surface of the substrate, thus making the mode less sensitive to bulk refractive index change.<sup>30,31</sup>

If the nanocube monolayers are prepared at a higher surface pressure (>5 mN/m, above the transition from the gas to condensed phase in the nanocube monolayer) the nanocubes aggregate and the dipolar and quadrupolar bands merge due to near-field

coupling.<sup>36,40-42</sup> As a result, it becomes impossible to separate the two modes and refractive index sensitivity of such supported monolayer drops dramatically (Table 5.3).

Table 5.3. Refractive index sensitivities of monolayer of 80 nm silver nanocube on glass as a function of surface pressure.

Surface pressure (mN/m)	Plasmon peak position $\lambda$ /nm	Refractive index sensitivity (nm/RIU)	Figure of merit
0.1 mN/m	480	73+/- 27	0.46
	450	89+/- 20	<b>2.12</b>
	380	46+/- 13	1.0
	350	39+/- 10	1.67
5 mN/m	480	n.d. <sup>a</sup>	n.d.
	450	103+/-17	<b>2.3</b>
	380	50+/- 6	1.3
20 mN/m	480	225+/-70	1.56
	450	83+/- 8	<b>2.2</b>
	380	42+/-16	1.0
25 mN/m	480	n.d.	n.d.
	450	87+/-30	1.3
	380	98+/-30	<b>2.1</b>
35 mN/m	480	n.d.	n.d.
	450	n.d.	n.d.
	380	71+/-17	1.2
5 mN/m with spacer <sup>b</sup>	480	280+/-138	1.6
	450	81+/-20	<b>1.7</b>
	380	48+/-18	1.2
	350	32+/-12	1.92
35 mN/m with spacer <sup>b</sup>	480	114+/-55	0.7
	450	77+/-6	<b>1.76</b>
	380	51+/-16	1.34
	350	28+/-9	1.4

<sup>a</sup> Not determined, <sup>b</sup>Phospholipid 1, 2-Dipalmitoyl-sn-Glycero-3-Phosphoethanolamine-N-(lissamine rhodamine B sulfonyl) (ammonium salt, DPPE-RhB) was added as a inert spacer to prevent the nanocubes from aggregation.

At the same time, if a passive spacer is introduced in the monolayer prior to the transfer to prevent the nanocubes from aggregating, the two modes are well separated

even at a high surface pressure<sup>36</sup> and the RIS and FOM remain unchanged up to the 35 mN/m surface pressure (Table 5.3).

It has to be mentioned however, that the “sharpness” of the spectral peaks decreased after several series of measurements in solutions, likely due to the previously reported smoothening/etching of the nanocube edges.<sup>30,43</sup> As a result the RIS and FOM decreased.

It is evident from results presented here that in terms of the figure of merit the quadrupolar mode of supported nanocube monolayers is the most sensitive to the solution refractive index change, due to the location of the oscillating charges away from the surface. This confirms previous experimental and theoretical considerations.<sup>30,31</sup>

Here we also observe the disappearance of the quadrupolar mode when the substrate is immersed in liquid, especially for smaller nanocubes. Although some averaging over a large ensemble of particles takes place, the FWHM of the substrates used in the present work is fairly narrow, and comparable to that of single nanocube measurements. For example the ~20 nm FWHM measured for the quadrupolar mode of 40 nm cubes in air (Figure 5.4A) is comparable to that of 0.146 eV<sup>30</sup> (22 nm<sup>11</sup>) FWHM for a single silver nanocube of comparable size. AFM images also confirm that the particles are fairly monodisperse. The disappearance of the quadrupolar band is therefore not a result of averaging, but rather of insufficiently large difference between the refractive indexes of the support and the solution to induce plasmon mode hybridization.<sup>31</sup> It is hence desirable to create conditions under which this mode is present even when immersed in solution. Such conditions can be likely obtained when refractive index difference between the solvent and the substrate is increased. Therefore, we selected several substrates with different refractive indices and prepared monolayers of 40 and 80 nm nanocubes.

### 5.3.2. Effect of substrate on the refractive index sensitivity

Figure 5.6A shows extinction spectra of 40 nm silver nanocube monolayers on different substrates with increasing refractive index (spectra 1-4) as well as the colloidal solution spectrum measured in ethanol (6).

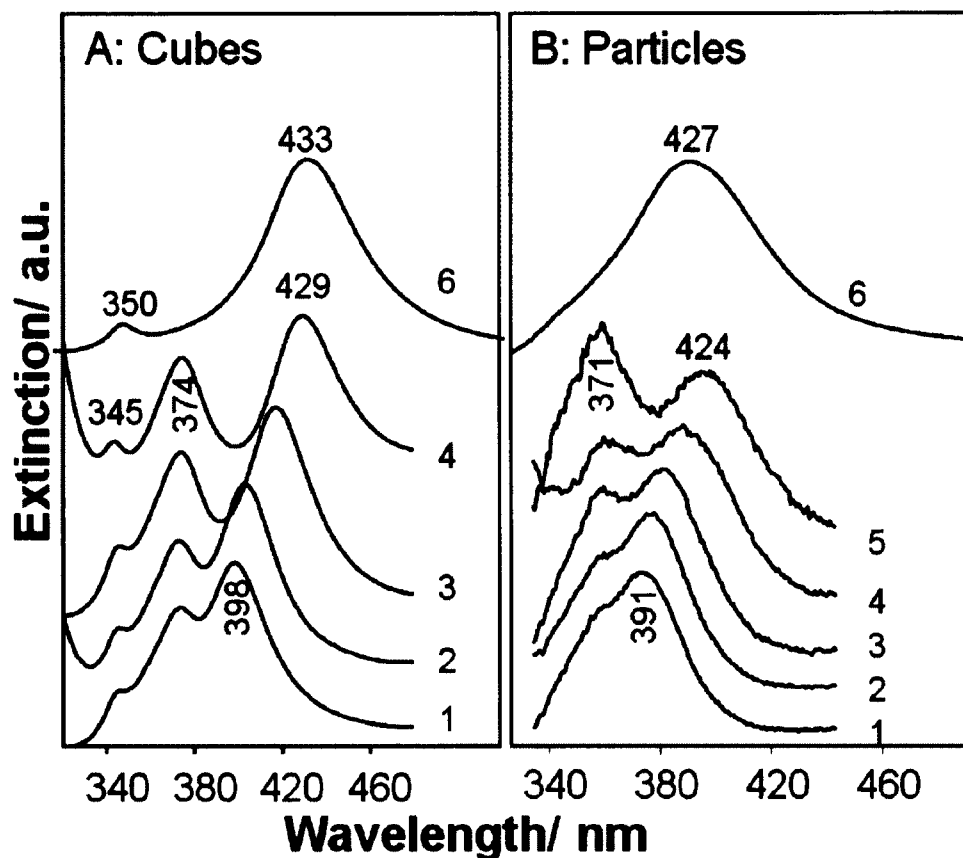


Figure 5.6. UV-vis spectra of supported 40 nm nanocubes (A) and irregular shaped nanoparticles (B) on different substrates: (1) quartz, (2) glass, (3) sapphire, (4) glass slide with coated with 5 nm  $\text{TiO}_2$  film, (5) glass slide coated with 5 nm of silicon, (6) spectra of suspensions in ethanol.

Instead of a dipolar mode, which is present in solution at 430 nm two new dipolar (D) and quadrupolar (Q) modes appear when supported on a dielectric substrate. The separation between the two bands depends linearly on the refractive index of the substrate (Figure 5.7).

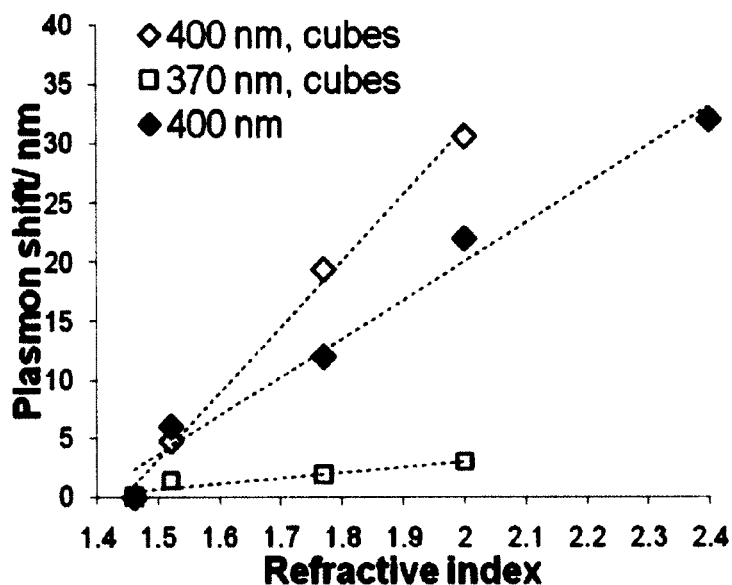


Figure 5.7. Plasmon shift of the dipolar (diamonds) and quadrupolar (squares, cubes only) bands in extinction spectra of supported 40 nm Ag nanocubes (open symbols) and irregular Ag nanoparticles (filled symbols) as a function of support refractive index.

However, the dependence of the D band observed at a longer wavelength is more pronounced, as it shifts from  $\sim 398$  nm for a quartz substrate ( $n=1.44$ ) to 429 nm for a substrate with 5 nm  $\text{TiO}_2$  film on glass, for which the refractive index of  $\sim 2.0$  was measured. At the same time the Q mode shifts only by 3 nm.

We calculated the sensitivities of the two bands to the substrate refractive index to be 56 nm/RIU and 4.6 nm/RIU for the dipole and quadrupole modes respectively. The corresponding FOM are 1.5 and 0.2. The two bands are fairly narrow with FWHM of  $\sim 40$  and 20 nm for D and Q modes respectively. Similar trend was observed for larger nanocubes. For monolayers of 80 nm nanocubes prepared on different substrates the dipolar mode gradually shifted from 410 to 436 to 452 to 471 nm for quartz, sapphire,  $\text{TiO}_2$  and silicon films respectively giving a refractive index sensitivity of 62 RIU/nm.

At the same time, positions of the quadrupolar and octupolar bands remained fairly constant (Figure 5.7).

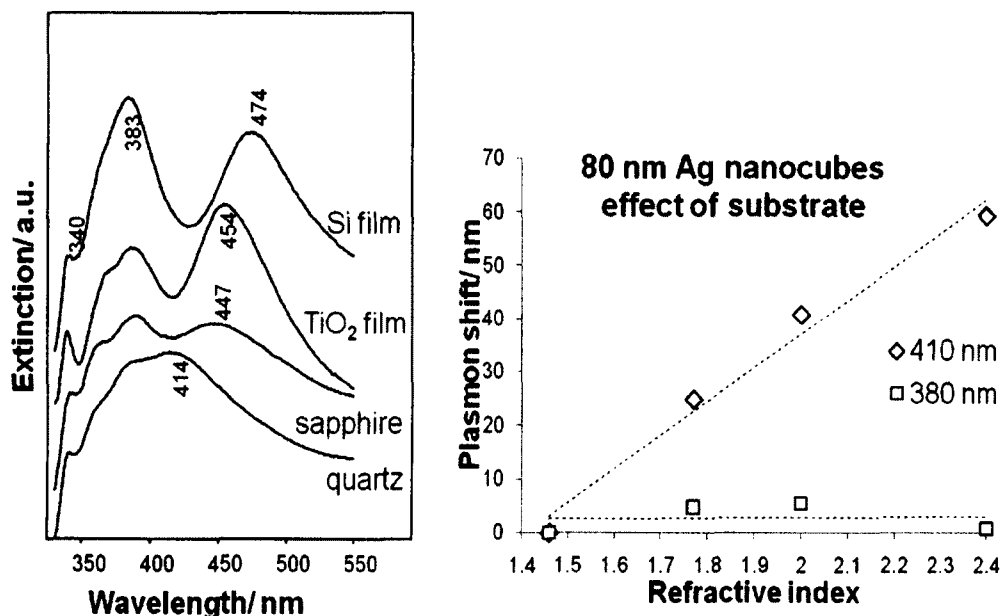


Figure 5.8. UV-vis spectra of supported 80 nm nanocubes on different substrates: quartz, sapphire, glass slide with coated with 5 nm TiO<sub>2</sub> film, glass slide coated with 5 nm of silicon (left). Plasmon shifts plotted vs. the refractive index of a substrate (right).

Since Q and D modes are well separated on a high refractive index substrate, such as TiO<sub>2</sub> film, we tested the sensitivity of the spectra to the refractive index of the solution. It is expected that in contrast to the glass substrate, the two plasmonic bands will remain separated on substrates with higher refractive index even when immersed in liquid. This should allow capitalizing on higher RI sensitivity of the Q mode. Results of the experiment are shown in figure 5.4. Indeed, the spectra of TiO<sub>2</sub> supported nanocubes immersed in low refractive index solvent (water) show clearly a shoulder at 400 nm (FWHM~ 27 nm) corresponding to the Q mode in addition to the main D mode at 432 nm (FWHM ~54 nm). As the refractive index increases, the shoulder gradually disappears. For pure ethylene glycol (refractive index 1.4318- ~0.6 lower than the

substrate) the shoulder is essentially absent. When the monolayer deposited on glass ( $n=1.52$ ) is immersed in water ( $n=1.33$ ) the RI difference between the substrate and the solution is already less than 0.2 units. Therefore, we conclude that for 40 nm nanocubes it is necessary to have a refractive index difference of at least 0.7 between the substrate and the solvent if we are to observe and use the Q mode for RI sensing.

Despite the fact that the Q mode essentially disappears for high RI solutions, peak fitting of the  $\text{TiO}_2$  supported 40 nm nanocube substrate spectra was attempted. Sensitivities of Q and D modes to the solution refractive index change were estimated to be 57 nm/RIU for D, 90 nm/RIU for Q mode, and 29 nm/RIU for the band at 350 nm (Figure 5.4B). The corresponding FOM are 1.3., 3.3, and 2.9. The figure of merit obtained for the Q mode is greater than calculated for the glass supported substrate (Table 5.2), and is very close to that of the colloidal solution (Table 5.1). It is obvious, that inability to separate the two peaks in liquid prevented us from calculating the RIS and FOM for the Q mode more precisely. It is expected that substrates with even higher refractive indexes would help in separating the two bands. In such case even higher FOM for the supported monodisperse nanocube monolayer can be achieved.

It is interesting to note, that the intensity of the Q band in UV vis spectra increases with angle between the substrate normal and the direction of light (Figure 5.9). When the angle increases excitation of out of plane charge oscillations becomes possible.<sup>38,44</sup> At the same time, it allows better interactions of light and dark modes, such as quadrupolar resonance.<sup>44</sup> Therefore, it is possible that measurements performed at larger incident angles could provide another tool in optimizing RIS and FOM.

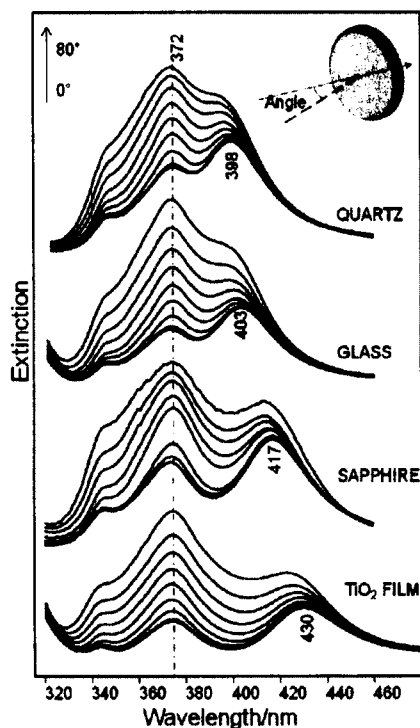


Figure 5.9. Angular dependence of UV-vis extinction spectra for 40 nm nanocubes deposited on different substrates.

Finally, to determine the role of cubic geometry in the substrate induced plasmon mode hybridization, appearance of new dipolar and quadrupolar modes, and consequent change in sensitivity to the refractive index, nanoparticles of the same size (40-45 nm, measured by AFM), but with more spherical shape (truncated nanocubes based on the extinction spectra) were used to form monolayers on different substrates. UV-visible extinction spectra are presented on figure 5.6B. The spectrum of colloidal suspension of these nanoparticles contains a dipolar peak at 427 nm, which is much broader than that of the nanocube suspension (Figure 5.6B and A, top spectra respectively). When deposited on a dielectric substrate two new bands appear. With increasing refractive index of the substrate the separation between the bands increases, which is similar to the nanocubes substrates. The degree of separation is however, significantly smaller resulting in the

refractive index sensitivity of the lower energy band  $\sim 33$  nm/RIU (Figure 5.6). Such behavior has previously been reported for spherical nanoparticles.<sup>28</sup> The two bands were reported to be dipolar modes with orthogonal moments: the lower energy band corresponding to electron oscillations parallel to the surface, and the higher energy band perpendicular to the surface.<sup>32</sup> In contrast the nanocube geometry allows different types of electron oscillations to be excited for the supported nanocube monolayers due to the larger contact area with the substrate<sup>30,31</sup> giving two bands with higher sensitivity to the refractive index changes of the substrate (D band) or the solvent (Q band), than that for the spherical particle monolayers.

#### **5.4. Conclusion**

In this work we compared the refractive index sensing properties of silver nanocubes for three different sizes suspended in solution and supported in monolayers on dielectric substrates. We found that under certain conditions supported nanocube monolayers can have refractive index sensitivity comparable to that of those in suspension. At the same time FOM can be even greater for substrate supported cubes. This could be achieved if mono-disperse nanocube samples and high refractive index substrates are used.

## 5.5. References

1. Rycenga, M. M.; Cogley, C.M.; Zeng, J.; Li, W.; Moran, C.H.; Zhang, Q.; Qin, D.; Xia, Y. *Chem. Rev.* **2011**, *111*, 3669.
2. Morton, S.M.; Silverstein, D.W.; Jensen, L. *Chem. Rev.* **2011**, *111*, 3962.
3. Lee, P.C.; Meisel, D. *J. Phys. Chem.* **1982**, *86*, 3391.
4. Fleischmann, M.; Hendra, P. J.; McQuillan, A. J. *Chem. Phys. Lett.* **1974**, *26*, 163.
5. Ianoul, A.; Bergeron, A. *Langmuir* **2006**, *22*, 10217.
6. Parfenov, A.; Gryczynski, I.; Malicka, J.; Geddes, C. ; Lakowicz, J.R. *J. Phys. Chem. B* **2003**, *107*, 8829.
7. Anger, P.; Bharadwaj, P.; Novotny, L. *Phys. Rev. Lett.* **2006**; *96*, 113002.
8. Rigneault, H.; Capoulade, J.; Dintinger, J.; Wenger, J.; Bonod, N.; Popov, E.; Ebbesen, T.W.; Lenne, P.-F. *Phys. Rev. Lett.* **2005**; *95*, 117401.
9. Hartstein, A.; Kirtley, J.R.; Tsang, J.C. *Phys. Rev. Lett.* **1980**, *45*, 201.
10. Chen, C.K.; de Castro, A.R.B.; Shen, Y.R. *Phys. Rev. Lett.* **1981**, *46*, 145.
11. Mayer, K.M.; Hafner, J.H. *Chem. Rev.* **2011**, *111*, 3826.
12. Galush, W.J.; Shelby, S.A; Mulvihill, M.J.; Tao, A.; Yang, P.; Groves, J.T. *Nano Lett.* **2009**, *9*, 2077.
13. Anker, J.N.; Hall, W.P.; Lyanders, O.; Shah, N.C.; Zhao, J.; Van Duyne, R. *Nature Materials* **2008**, *7*, 442.
14. Zou, S.; Janel, N.; Schatz, G.C. *J. Chem. Phys.* **2004**, *102*, 10871.
15. Auguie, B.; Barnes, W.L. *Phys. Rev. Lett.* **2008**, *101*, 143902.
16. Halas, N.J.; Lai, S.; Chang, W.-S.; Link, S.; Nordlander, P. *Chem. Rev.* **2011**, *111*, 3913.

17. Giannini, V.; Fernandez-Dominguez, A.I.; Heck, S.C.; Maier, S.A. *Chem. Rev.* **2011**, *111*, 3888.
18. Seok, T.J.; Jamshidi, A.; Kim, M.; Dhuey, S.; Lakhani, A.; Choo, H.; Schuck, P.J.; Cabrini, S.; Schwartzberg, A.M.; Bokor, J.; Yablonovitch, E.; Wu, M.C. *Nano lett.* **2011**, *11*, 2606.
19. Liu, N.; Hentschel, M.; Weiss, T.; Alivisatos, A.P.; Giessen, H. *Science* **2011**, *332*, 1407.
20. Kelly, K. L.; Coronado, E.; Zhao, L. L.; Schatz, G.C. *J. Phys. Chem. B* **2003**, *107*, 668.
21. Barbosa, S.; Agrawal, A.; Rodriguez-Lorenzo, L.; Pastoriza-Santos, I.; Alvarez-Puebla, R. A.; Kornowski, A.; Weller, H.; Liz-Marzan, L. M. *Langmuir* **2010**, *26*, 14943.
22. Mulvaney, P. *Langmuir* **1996**, *12*, 788.
23. Burda, C.; Chen, X.; Narayanan, R.; El-Sayed, M. A. *Chem. Rev.* **2005**, *105*, 1025.
24. Sosa I.O.; Noguez, C.; Barrera, R.G. *J. Phys. Chem.* **2003**, *107*, 6269.
25. Tao, A.; Sinsermsuksakul, P.; Yang, P. *Angew. Chem. Int. Ed.* **2006**, *45*, 4597.
26. Kumbhar, A.S.; Kinnan, M.K.; Chumanov, G. *J. Am. Chem. Soc.* **2005**, *127*, 12444.
27. Zhou, F.; Li, Z-Y.; Liu, Y.; Xia, Y. *J. Phys. Chem. C* **2008**, *112*, 20233.
28. Knight, M.K.; Wu, Y.; Lassiter, J.B.; Nordlander, P.; Halas, N.J. *Nano lett.* **2009**, *9*, 2188.
29. McMahan, J. M.; Wang, Y.; Sherry, L.J.; Van Duyne R. P.; Marks, L.D.; Gray, S.K.; Schatz, G.C. *J. Phys. Chem. C* **2009**, *113*, 2731.

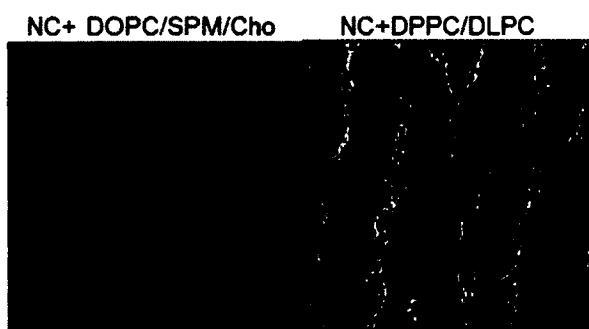
30. Sherry, L.J.; Chang, S-H.; Schatz, G.C.; Van Duyne, R.P.; Wiley, B.J.; Xia, Y. *Nano lett.* **2005**, *5*, 2034.
31. Zhang, S.; Bao, K.; Halas, N.J.; Xu, H.; Nordlander, P. *Nano lett.* **2011**, *11*, 1657.
32. Ringe, E.; McMahon, J. M.; Sohn, K.; Cobley, C.; Xia, Y.; Huang, J.; Schatz, G.C.; Marks, L.D.; Van Duyne R. P. *J. Phys. Chem. C* **2010**, *114*, 12511.
33. Henry, A.-I.; Bingham, J.M.; Ringe, E.; Marks, L.D.; Schatz, G.C.; Van Duyne, R.P. *J. Phys. Chem. C* **2010**, *115*, 9291.
34. Mahmoud, M. A.; El-Sayed, M. A. *Nano Lett.* **2011**, *11*, 946.
35. Skrabalak, S. E; Au, L.; Li, X.; Xia, Y. *Nature Protocols* **2007**, *2*, 2182.
36. Ahamad, N.; Ianoul. A. *J. Phys. Chem. C* **2011**, *115*, 3587.
37. Chem, H.; Kou, X.; Yang, Z.; Ni, W.; Wang, J. *Langmuir*, **2008**, *24*, 5233.
38. Lee, Y.H.; Chen, H.; Xu, Q.-H.; Wang, J. *J. Phys. Chem C* **2011**, *115*, 7997.
39. Siekkinen, A.R.; McLellan, J.M.; Chen, J.; Xia, Y. *Chem. Phys. Lett.* **2006**, *432*, 491.
40. Lassiter J. B.; Aizpurua, J.; Hernandez, L.I.; Brandl, D.W.; Romero, I.; Lal, S.; Hafner, J.H.; Nordlander, P; Halas, N.J. *Nano Lett.* **2008**, *8*, 1212..
41. Slaughter, L.S.; Wu, Y.; Willingham, B.A.; Nordlander, P.; Link, S. *ACS Nano.* **2010**, *4*, 4657.
42. Zuloaga, J.; Prodan, E.; Nordlander, P. *Nano Lett.* **2009**, *9*, 887.
43. Goldys, E.M.; Calander, N.; Drozdowicz-Tomsia, K. *J. Phys. Chem. C* **2011**, *115*, 676.
44. Hao, F.; Sonnefraud, Y.; Van Dorpe, P.; Maier, S.A.; Halas, N.J.; Nordlander, P. *Nano lett.* **2008**, *8*, 3983.

## Chapter 6

---

### **Assembling Plasmonic Nanostructures into Distinct Configurations on Solid Substrates Using Lipids as Templates**

J. Nanopart. Res 2012 (Accepted)



## 6.1. Introduction

The Langmuir-Blodgett (LB) technique was developed for investigating physicochemical behavior of amphiphilic molecules such as lipids and fatty acids in monolayers formed at air-water interface.<sup>1</sup> The advantage of LB technique is that water supported monolayer can be transferred onto a solid support for further investigation by various surface characterization techniques.<sup>2</sup> Presently, LB technique has evolved as a powerful assembly approach for bottom-up fabrication of complex hierarchical structures consisting of various macromolecules to nanoscale building blocks with desired functional properties.<sup>3</sup> LB technique is considered as possible alternative for conventional lithographic technique as it provides more flexibility in patterning complex 3D surfaces. Langmuir monolayers of lipids and colloidal hydrophobic metal nanoparticles have been reported to form different patterns including parallel stripes and channels, circular domains, etc.<sup>4-10</sup> Recent studies have shown that Langmuir monolayers of block copolymers and lipids constrain hydrophobic Au nanoparticles (NP) into defined structures where lipids or polymer molecules serve as structure directing agents.<sup>2,11-13</sup> It is known that metal nanoparticles and their assemblies exhibit unique optical properties<sup>14</sup> which vary upon assembling.<sup>15,16</sup> Assembling metal nanoparticles into 2D structures has attracted particular interest in material science because of their unique optical properties which can be exploited to develop plasmon based sensor platform, surface enhanced Raman scattering (SERS) substrates etc.<sup>17-19</sup> Silver nanocubes (NCs) exhibit distinction plasmonic signature both in colloidal and solid supported 2D assemblies due to their sharp edges and corners.<sup>20,21</sup> In a previous report, we demonstrated plasmonic properties of 2D assemblies of silver nanocubes with controlled inter-particles distance using

phospholipids.<sup>22</sup> In the present research work we demonstrate strategy for assembling silver nanocubes into different micro-scale patterns i.e.; rounded islands and linear-branched chains by exploiting lipids phase behaviors. Our approach paves the way to fabricate pattern surfaces which may have application in nanotechnology as well as fundamental research on interaction of model cell membrane with hydrophobic nanoparticles.

## **6.2. Materials and methods**

### **6.2.1. Chemicals**

Silver nitrate ( $\text{AgNO}_3$ , 99%+), polyvinylpyrrolidone (PVP,  $M_w \sim 55,000$ ), ethylene glycol (EG) and chloroform were purchased from Sigma-Aldrich and used as obtained. Hydrochloric acid (HCl, 38%) and ethanol (95%) were obtained from Anachemia and Brampton respectively and used without further purification. Cholesterol, 1,2-dioleoyl-sn-glycero-3-phosphocholine (DOPC), sphingomyelin (SPM, Egg, Chicken), 1,2-dipalmitoyl-sn-glycero-3-phosphocholine (DPPC) and 1,2-Dilauroyl-sn-glycero-3-phosphocholine (DLPC) were purchased from Avanti Polar Lipids, Alabaster, AL.

### **6.2.2. Preparation of nanocubes**

A colloidal suspension of silver nanocubes (NC) was synthesized by a modified polyol process developed by Xia et al.<sup>23</sup> In a typical synthesis, 5 ml EG was placed in a 100 ml triple necked round bottom flask and heated at 140°C for 1 h under stirring with Teflon coated magnetic stirring bar using a temperature-controlled silicon oil bath. While EG was heated, EG solutions containing  $\text{AgNO}_3$  (94 mM) and PVP (147 mM) were prepared. One ml of HCl solution in EG (3 mM), prepared 30 min prior to completion of EG heating time, was added quickly. Ten minutes after the injection of HCl, 3 ml of both

AgNO<sub>3</sub> and PVP solutions were added simultaneously in the hot reaction mixture at a rate of ~750 ml/min using glass syringes. The resulting solution was allowed to heat for 26 h under reflux conditions. The final product was cooled to room temperature and subjected to further purification.

### **6.2.3. Purification of colloidal silver nanocubes**

The as synthesized colloidal nanocubes contained unreacted EG, excess of PVP and nanorods as a by-product. EG and PVP were removed by diluting the colloidal solution with ethanol (1:1 by volume) followed by centrifugation at 12,000 rpm. The precipitate was collected and re-dispersed in ethanol by sonication. This process was repeated 30 times for complete removal of EG and PVP. Silver nanorods were separated from the nanocubes by filtering the pre-washed NC in ethanol using PTFE syringe filters (pore size: 0.45µm and 0.22µm). The purified silver NC solution was further subjected to washing with chloroform by centrifugation (at least 3 times) prior to the LB film preparation. The final volume of the nanocubes solution was 4 ml.

### **6.2.4. Preparation of LB monolayers**

Langmuir monolayers were prepared on Langmuir-Blodgett trough (NIMA 611, Coventry, UK) using Milli-Q water as the sub-phase. Monolayers of DOPC/SPM/Cholesterol (1:1:1 or 2:2:1 mole ratios) mixed with silver NCs were prepared by mixing 20 µL of lipids mixture (total lipid concentration 1mM in chloroform) with 250 µL of NCs suspended in chloroform and subsequent spreading of this final mixture on the water sub-phase. Monolayer of DPPC/DLPC (1/3 mole ratio) mixed with silver NCs was prepared by mixing 10 µL of lipid mixture (total lipid concentration 1mM in chloroform) with 250 µL of silver NCs suspended in chloroform

followed by spreading the final mixture on the water sub-phase. Each monolayer was left on the trough for 20 min for chloroform evaporation. At least three isotherm cycles were collected to anneal the monolayers. Each monolayer was compressed at a rate of 20 cm<sup>2</sup>/min to the desired surface pressure (measured with a precision of 0.1 mN/m using a Wilhelmy plate) at which the monolayer was transferred onto the solid substrates. All the monolayers were deposited onto glass slides except DPPC/DLPC/NCs monolayer for which freshly prepared mica was used.

**6.2.5. UV-vis measurement:** UV-vis spectra of different 2D assemblies of silver NCs deposited on the glass substrates were recorded using Shimadzu, UV-2450 UV-vis spectrophotometer.

#### **6.2.5. Topography measurements**

The topography of different lipid/NCs films was obtained using an Ntegra (NTMDT, Russia) atomic force microscope in semi contact mode in air at 23°C with 512×512 points per image. A 100×100 μm<sup>2</sup> scanner (Ntegra) and cantilevers with rotated monolithic silicon tips (125 μm long, 40 N/m spring constant Tap 300Al, resonance frequency 315 kHz, Budget Sensors) were used for all topographic measurements. The typical scan rate was 0.5 Hz. AFM images were further processed by Nova image processing software.

### 6.3. Results and Discussions

#### 6.3.1. *Assembly of silver nanocubes into circular islands*

It has been reported by our group as well as others that hydrophobic metal nanoparticles usually reside in liquid extended (LE) phase in binary lipids mixture.<sup>2, 22</sup> Such preferential localization of nanoparticles in the LE phase is attributed to higher mobility of nanoparticles in LE phase compared to that in liquid condensed (LC) phase of the lipid mixtures. More complex lipid mixtures can also exhibit phase separation. For example, Johnston et al studied the size of the lipid rafts in mixtures consisting of DOPC/SPM/cholesterol (1:1:1) using AFM.<sup>5</sup> They reported that SPM forms LC phase round domains interspersed in LE phase DOPC matrix on LB monolayer of DOPC/SPM transferred at 15 mN/m on mica. Such round domains of SPM exhibited a wide range of size distribution ranging from hundreds of nanometers to few micrometers. They also demonstrated the effect of cholesterol on the size of those rafts by investigating LB monolayer of DOPC/SPM with varied amount of cholesterol (20 and 33 %). Their findings include the formation of both small and large scale domains at lower surface pressure of 7 mN/m. Increasing both the surface pressure and cholesterol fraction increase the number and size of those domains. In this context, cholesterol is postulated to have a preferential affinity for the SPM and have ability to condense the lateral packing of SPM.<sup>24-26</sup> Therefore, we hypothesized that it may possible to achieve uniform raft domains by varying the amount of cholesterol in the raft mixture and organize the nanoparticles at the interface between LE phase of DOPC and LC phase of SPM/Cholesterol to fabricate ring- like configuration of nanoparticles using LB technique. We therefore investigated properties of LB monolayers composed of silver

NCs mixed with two different raft mixtures with varied cholesterol composition: DOPC/SPM/cholesterol (2:2:1) and DOPC/SPM/cholesterol (1:1:1).

To observe the effect of LC phase of SPM/cholesterol and LE phase of DOPC on the morphology of the NCs assembly on LB monolayer, AFM topographic images were recorder. Figures 6.1 and 6.2 depicts the AFM topographic images of raft (2:2:1 and 1:1:1)/NC monolayers, transferred on glass slides at different surface pressures. We were expecting a ring like pattern where NCs localize on LE phase of DOPC matrix enclosing rounded LC phase domain of SPM/cholesterol. Interestingly however, it is noted that instead of forming ring like pattern, NCs formed round islands. It appeared that assemblies of NCs superimposed on LC phase SPM/cholesterol domain interspersed in LE phase of DOPC matrix. Firstly, raft (2:2:1)/NC monolayer transferred at low surface pressures (5 and 10 mN/m) consisted of separated round islands of NCs with a wide range of size distribution ranging from hundreds of nanometer to tens of micrometers as shown in the figure 6.1 (5 and 10 mN/m). For monolayer transferred at higher surface pressure (25 mN/m), the micron size rounded domains no longer existed, rather the larger domains collapsed into a large number of nanoscale domains distributed in the entire substrate (Figure 6.1, right column).

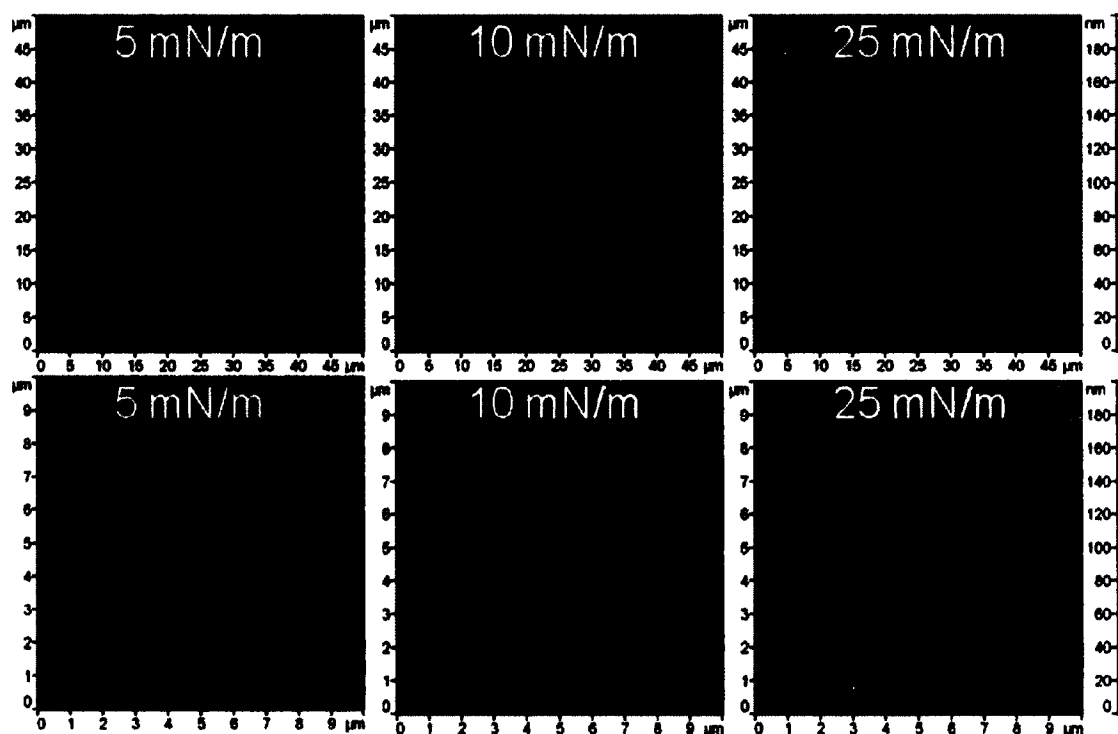


Figure 6.1. AFM topography images (top,  $50 \times 50 \mu\text{m}^2$  and bottom,  $10 \times 10 \mu\text{m}^2$ ) of DOPC/SPM/cholesterol (2:2:1)/NCs monolayers deposited on glass at different surface pressures.

On the contrary, raft (1:1:1)/NC monolayer transferred at low surface pressures (5 and 10 mN/m) showed clear phase separated islands of NCs (Figure 2, 5 mN/m and 10 mN/m). Further increase in surface pressure enlarged the islands size due to the coalescence of the smaller islands (Figure 6.2, right column). An interesting morphology was observed for the monolayer transferred at a surface pressure of 10 mN/m. At this pressure circular islands of NCs having diameter  $3 \pm 1 \mu\text{m}$  were interspersed within the substrates.

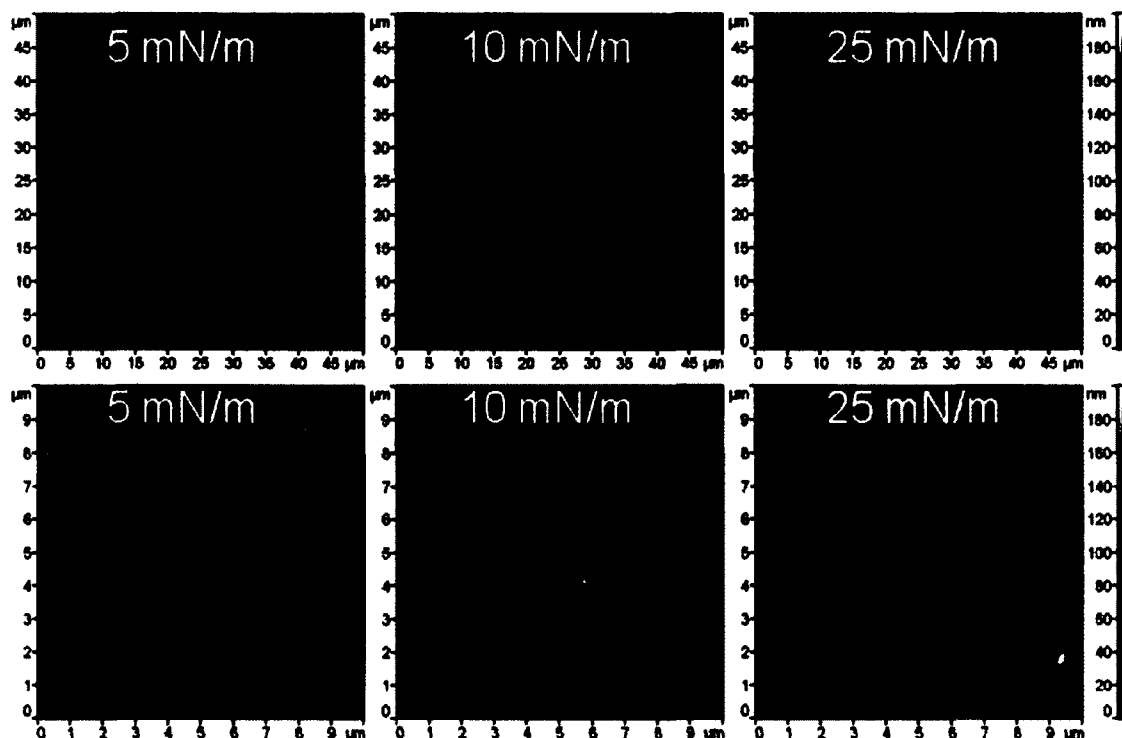


Figure 6.2. AFM topographic images (top,  $50 \times 50 \mu\text{m}^2$  and bottom,  $10 \times 10 \mu\text{m}^2$ ) of DOPC/SPM/cholesterol (1:1:1)/NCs monolayers deposited on glass at different surface pressures.

The morphological difference between NCs assemblies within the two raft mixtures are: (1) size and shape are more uniform in raft (1:1:1)/NC monolayer than these are in raft (2:2:1)/NC and (2) interparticle gap within individual NCs island is shorter in raft (111) than it is in raft (221). Variation of the interparticles distance can be followed by the change in plasmonic signature of silver NCs in the 2D assemblies i.e.; extinction spectra of the NCs assembly as reported previously.<sup>22</sup> Extinction spectra of 80 nm silver NCs comprises of four plasmon modes in solid supported assembly of NCs with low density.<sup>22</sup> The two major peaks observed at 435 and 389 nm are assigned to dipolar and quadrupolar modes of localized surface plasmon resonances (LSP) respectively, and whose amplitudes are stronger at the corners of the cube. As the NCs approach each others, at a certain distance, electron distribution of individual NC is changed which in

turn affects their plasmonic response. In this situation, overlapping of dipolar and quadrupolar resonance peaks takes place. The extinction spectra of raft (1:1:1)/NCs and raft (2:2:1)/NCs substrates transferred at a surface pressure of 10 mN/m reveal that overlapping of dipolar and quadrupolar resonance bands is less in raft (221)/NCs than it is in raft (111)/NCs as shown in figure 6.3. This suggests that NCs are more concentrated in raft (111)/NCs substrate than in raft (221)/NCs, which is consistent with AFM images.

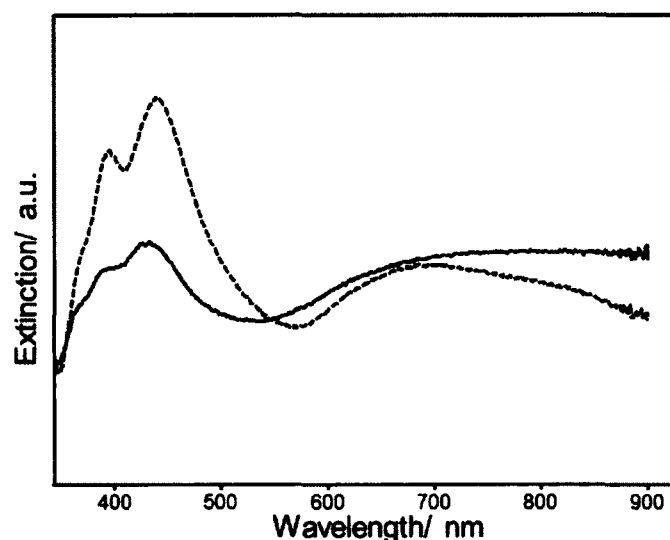


Figure 6.3. Extinction spectra of glass supported monolayers of DOPC/SPM/cholesterol (2:2:1)/NCs (dashed line) and DOPC/SPM/cholesterol (1:1:1)/NCs (solid line). The transfer pressure for both monolayers was 10 mN/m.

The morphological features of the NCs assemblies within raft mixtures resemble the phase behavior of the raft mixture consisting of DOPC/SPM/cholesterol itself as reported in the literature.<sup>26</sup> It is reported that SPM/cholesterol form LC phase round domains within the LE phase matrix of DOPC while transferring DOPC/SPM/cholesterol (2:2:1) monolayer on mica at low pressures. The role of cholesterol has been described as to help packing the SPM molecules.<sup>27,28</sup> An increase in cholesterol concentration in the raft forming mixture reduces the size of domains.<sup>29</sup> Hydrophobic matching between

cholesterol and the longer saturated acyl chains of SM maximizes the formation of hydrogen bonds between the cholesterol hydroxyl group and the amide function in sphingomyelins.<sup>29</sup> Thus, it is likely that NCs preferentially localize within LC phase of SPM/cholesterol domains. To verify that such patterns were not formed in DOPC, we investigated AFM image of DOPC/NCs monolayer transferred at a surface pressure of 10 mN/m (Figure 6.4). The result showed a homogeneous distribution of NCs in DOPC matrix. This indicates that DOPC existed in LE phase and was not responsible for domain formation when the raft mixtures were used.

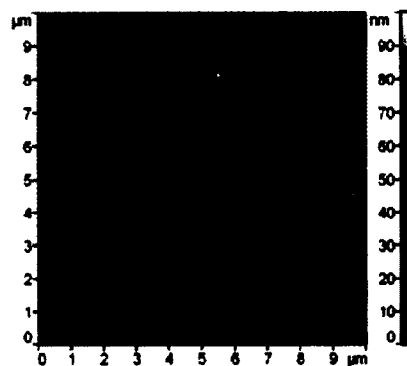


Figure 6.4. AFM topographic images of DOPC/NCs monolayer deposited on glass at 10 mN/m surface pressure.

From this result we concluded that nanocubes preferentially aggregate on the SPM/cholesterol rich domain where cholesterol acts as packing agent. It is likely that hydroxyl groups of cholesterol formed hydrogen bonding with the polar groups of PVP that capped on the silver NCs. The basis of such assumption is that PVP capped silver NCs are highly soluble in ethanol and ethylene glycol. Finally, we hypothesized that cholesterol interacted with silver NCs through hydrogen bonding between hydroxyl groups of cholesterol and polar carbonyl groups of PVP capped on NCs' surface during the initial mixing of the raft mixture with NCs and NCs-cholesterol complex preferentially located in the LC phase of SPM.

### **6.3.2. Linear-branched chains of silver nanocubes**

Pattern formation consisting of periodic stripes and channels have been reported for single (DPPC)<sup>30</sup> and double (DPPC/DLPC)<sup>4</sup> phospholipid monolayers deposited on a solid support. Such pattern is obtained when Langmuir film is transferred at a lateral surface pressure below or close to the phase transition between LE to LC phase of the film component.<sup>4,30</sup> Formation of this stripe pattern is attributable to dynamic wetting instability during film transfer. This instability is caused by substrate (mica) mediated condensation, a process whereby the Langmuir monolayer is deposited onto solid substrate in a more condensed state compared to the state on the water surface.<sup>4</sup> During the film deposition, the adhesion force tends to decrease the height of film meniscus whereas the vertical pulling motion of substrate tends to increase the meniscus. These two counteracting processes lead to an oscillation of the meniscus which gives rise to the periodic pattern. However, Langmuir monolayer of two components lipid system like DPPC/DLPC (1/3) exhibits phase separation at high lateral surface pressure (32 mN/m). DPPC forms circular LC phase while DLPC exists as LE phase. Therefore during the film transfer, wetting instability causes deposition of LC phase of DPPC and LE phase of DLPC in a periodic manner.<sup>4,9</sup> It might be possible to assemble silver NCs into distinct pattern by exploiting the specific interaction of NCs with lipid phases (LE vs. LC).

To reveal the effect of lipid phase behavior (LE vs. LC) on the morphology of silver NCs assembly, Langmuir monolayers of DPPC/DLPC/NCs and DPPC/NCs were transferred onto freshly cleaved mica at desired surface pressures and subsequently AFM topographic images were obtained (Figure 6.5). AFM image of DPPC/DLPC/NCs deposited at 15 mN/m surface pressure showed (Figure 6.5A) discrete chain like islands

having nanoscale circular NCs- free spaces inside of them. It is likely that LC phase DPPC formed circular domains at surface pressure below 15 mN/m and the NCs localized on the LE phase DLPC enclosing the domain which further coalesced to form islands during the monolayer transfer. But when the monolayer was transferred at a surface pressure of 32 mN/m, it formed periodic-branched chains extending to tens of micrometers (Figure 6.5B). The mean width of the islands is 1.8  $\mu\text{m}$  and the mean separation distance between two parallel islands is 8.3  $\mu\text{m}$ . Moreover, the alignment of those islands was normal to the monolayer transfer direction.

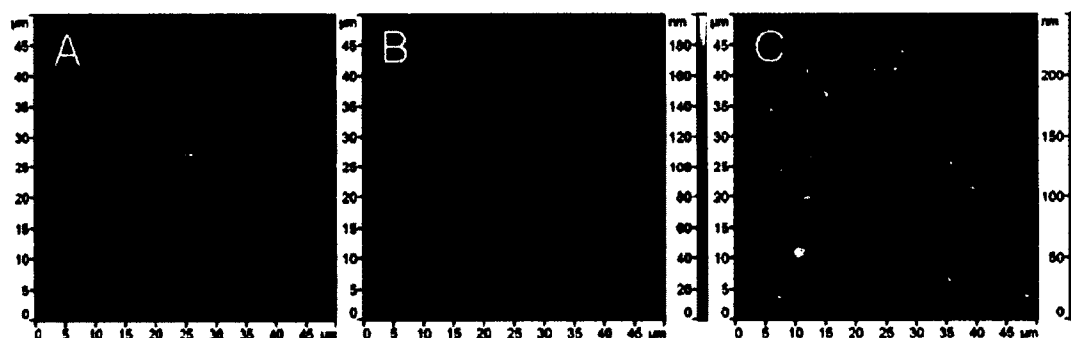


Figure 6.5. AFM topography images of DPPC/DLPC (1/3)/NCs deposited on mica at two different surface pressures (A) 15 mN/m, (B) 32 mN/m. (C) AFM topography image of DPPC/NCs deposited at 32 mN/m.

The mechanism of islands formation is likely similar to that of periodic stripes and channels formation in DPPC/DLPC LB monolayer.<sup>4</sup> However, in DPPC/DLPC/NCs Langmuir monolayer NCs preferentially localize in the LE phase of DLPC because of higher mobility in LE phase compared to the LC phase.<sup>2</sup> During the monolayer transfer onto mica, the oscillation of three phase contact line brings about the deposition of LC phase DPPC and LE phase of DLPC along with NCs aggregates on top in a periodic manner. To further confirm that such pattern was not formed by substrates mediated

condensation of DPPC we deposited a monolayer of DPPC/NCs under the same conditions as DPPC/DLPC/NCs monolayer deposition. AFM image of this substrate (Figure 6.5C) showed a completely different morphology: silver NCs aggregated around circularly shaped NCs- free spaces in the films. The circular regions most likely comprised of LC phase DPPC domains which restrict the NCs into adjacent areas. Such pattern formation has been reported earlier.<sup>30</sup> However, to compare with earlier report that stripe pattern is not formed on the glass substrate<sup>9</sup> we transferred DPPC/DLPC/NCs monolayer on the glass at 15 and 32 mN/m surface pressures under the same conditions and took the AFM image which are presented in figure 6.6.

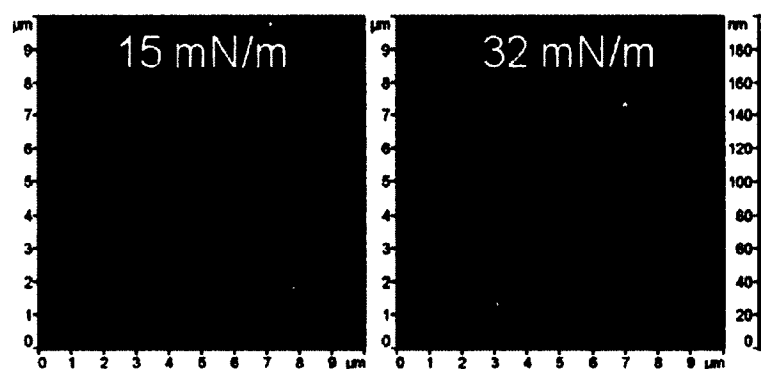


Figure 6.6. AFM topography images of DPPC/DLPC (1/3)/NCs monolayer deposited on glass at 15 and 32 mN/m surface pressures.

It is obvious that instead of the stripe pattern, a homogeneous distribution of NCs assembly is obtained. Therefore we concluded that periodic linear-branched chains like pattern was formed by the differential wetting ability of LE phase of DLPC and LC phase of DPPC during the transfer process.

#### 6.4. Conclusion

This study presents an approach to assemble plasmonic silver nanocubes into distinct patterns i.e.; circular islands and linear branched islands by exploiting the lipids phase behavior in Langmuir monolayer. Analyzing the topographic images of the LB film, an explanation of such patterns formation has been put forward. First, circular islands of silver NCs ( $3\pm 1\mu\text{m}$  in diameter) were observed in LB monolayer of DOPC/SPM/cholesterol (1:1:1) mixed with silver NCs transferred at a lateral surface pressure of 10 mN/m. This pattern was formed by specific affinity of silver NCs, coated with PVP, for condensed phase SPM/cholesterol domain. Cholesterol was found to play important role in governing the size and shape of those islands. Second pattern consisted of linear-branched chains with mean width of 1.8  $\mu\text{m}$  separated by channels having a mean width of 8.3  $\mu\text{m}$ . The islands were made of aggregates of NCs that were originally present in LE DLPC phase and the channels were made of LC phase DPPC. This periodic pattern of NCs islands was formed by phase specific localization of NCs in Langmuir monolayer followed by alignment and phase induced deposition during the transfer process. It is likely that further optimization of the lipid mixtures and transfer processes would allow better control of domain size to extend the approach down to the nanoscale.

## 6.5. References

1. Zasadzinski, J.A.; Viswanathan, R.; Madsen, L.; Garnaes, J.; Schwartz, D.K. *Science* **1994**, *263*, 1726.
2. Mogilevsky, A.; Volinsky, R.; Dayagi, Y.; Markovich, N. and Jelinek, R. *Langmuir* **2010**, *26*, 7893.
3. Yang, P.; Kim, F. *ChemPhysChem* **2002**, *3*, 503.
4. Moraille, P. ; Badia, A. *Langmuir* **2002**, *18*, 4414.
5. Yuan, C.; Furlong, J.; Burgos, P.; Johnston, L.J. *Biophys. J.* **2002**, *82*, 2526.
6. Tao, A.R.; Huang, J.; Yang, P. *Accounts of Chemical Research* **2008**, *41*, 1662.
7. Kopf, M.H.; Gurevich, S.V.; Friedrich, R.; Chi, L. *Langmuir* **2010**, *26*, 10444.
8. Chen, X. ; Lenhert, S. ; Hirtz, M. ; Lu, N.; Fuchs, H. ; Chi, L. *Acc. Chem. Res.* **2007**, *40*, 393.
9. Moraille, P. ; Badia, A. *Langmuir* **2003**, *19*, 8041.
10. Lu, N. ; Gleiche, M. ; Zheng, J. ; Lenhert, S. ; Xu, B. ; Chi, L. ; Fuchs, H. *Adv. Mater.* **2002**, *14*, 1812.
11. Mogilevsky, A.; Jelinek, R. *Langmuir* **2011**, *27*, 1260.
12. Bai, X. ; Dong, B. ; Zheng, L. *Langmuir* **2010**, *26*, 14970.
13. Jones, M.R. ; Osberg, K.D. ; Macfarlane, R.J. ; Langille, M.R. ; Mirkin, C.A. *Chem. Rev.* **2011**, *111*, 3736.
14. Rycenga, M; Cogley, C.M ; Zeng, J. ; Li, W. ; Moran, C.H. ; Zhang, Q. ; Qin, D. ; Xia, Y. *Chem. Rev.* **2011**, *111*, 3669.
15. Halas, N. J. ; Lai, S. ; Chang, W. S. ; Link, S. ; Nordlander, P. *Chem. Rev.* **2011**, *111*, 3913.

16. Ou, F.S. ; Hu, M.; Naumov, I. ; Kim, A. ; Wu, W. ; Bratkovsky, A.M. ; Li, X. ; Williams, R.S. ; Li, Z. *Nano Lett.* **2011**, *11*, 2538.
17. Obare, S.O.; Jana, N.R.; Murphy, C.J. *Nano Lett.* **2001**, *1*, 601.
18. Lindquist, N.C.; Johnson, T.W.; Norris, D.J.; Oh, S.-H. *Nano Lett.* **2011**,*11*,3526.
19. Ruan, W.; Wang, C.; Ji, N.; Lu, Z.; Zhou, T.; Zhao, B. J.R. Lombardi, *Langmuir* **2008**, *24*,248417.
20. Tao, A.; Sinsersuksakul, P.; Yang, P. *Nature Nanotech.* **2007**, *2*, 435.
21. Tao, A.; Sinsersuksakul, P.; Yang, P. *Angew. Chem. Int. Ed.* **2006**, *45*, 4597.
22. Ahamad, N.; Ianoul, A. *J. Phys. Chem. C* **2011**, *115*, 3587.
23. Sang, H.I. ; Yun, L.T. ; Benjamin, W. ; Xia, Y. *Angew. Chem. Int. Ed.* **2005**, *44*, 442154.
24. Veatch, S.L.; Keller, S.L. *Biophys. J.* **2003**, *84*,725.
25. McMullen, T.P.W.; McElhaney. R.N. *Curr. Opin. Colloid and Interface Sci.* **1996**, *1*, 83.
26. Ianoul, A.; Strekal, N.; Maskevich, S. *J. Nanosci. Nanotechnol.* **2006**, *6*, 61.
27. Collado, M.; Gofii, F.M.; Alonso, A.; Marsh, D. *Biochemistry* **2005**, *44*, 4911.
28. Bittman, R.; Kasireddy, C.R.; Mattjus, P. ; Slotte, J.P. *Biochemistry* **1994**, *33*, 11776.
29. Milhiet,P.E.; Domec, C.; Giocondi, M.C.; Van Mau, N.; F. Heitz, Le Grimellec, C. *Biophys. J.* **2001**, *81*, 547.
30. Gleiche, M.; Chi,L.F.; Fuchs, H. *Nature* **2000**, *403*, 173.

## **Chapter 7**

---

### **Conclusions and Recommendations for Future Work**

## 7.1. Conclusions

The purpose of this thesis was to synthesize silver and gold nanostructures by chemical methods and engineer solid supported 2D assemblies of those nanostructures with controlled plasmonic properties in order to develop novel plasmonic sensors.

To realize the nature of near field on plasmonic nanoparticles, generated by surface plasmon excitation, we studied distance dependent SERS and SEF enhancement of a self-assembled monolayer consisted of 20 nm silver nanoparticles (NPs). Polyelectrolytes multilayers were used as spacer layer between the monolayer and the probes (Rh6G and PAH-FITC). The solid supported assembled nanoparticles exhibited both SERS and SEF activities. However, the distance dependent SERS enhancement of Rh6G showed a decreasing trend at distances away from the NP surface. The highest enhancement was observed at a distance corresponding to one bilayer (~1 nm). We noticed a significant diffusion of Rh6G molecules through polyelectrolytes matrix, which formed non-fluorescent aggregates. On the contrary, PAH-FITC did not exhibit any diffusion as it was bound to the polyelectrolyte backbone and employed to study the distance dependent SEF enhancement. However, distance dependent SEF enhancement of FITC showed an increasing trend which corroborates with de-quenching of fluorescence at distances away from nanoparticle surface. Both of the phenomena support the distance dependent decaying nature of local electric field surrounding the metal nanoparticles upon excitation of surface plasmon.

Control over inter-particle distance while creating effective SERS substrates is crucial to exploit an enhanced electromagnetic field. It is difficult to manipulate nanoscale interparticles distance in 2D self-assembled monolayer of nanoparticles. To

address this issue, we exploited phase behavior of zwitterionic phospholipid 1, 2-Dipalmitoyl-sn-Glycero-3-Phosphoethanolamine (DPPE) and of a 1:1 mixture of DPPE with DPPE analogue labeled with Rhodamine B (DPPE-RhB) to control interparticle distance and therefore optical properties of silver nanocube substrates prepared by Langmuir monolayer technique. A more homogeneous distribution of the nanocubes was observed in DPPE/DPPE-RhB mixture, compared to DPPE at all surface pressures due to a more fluid nature of the mixed lipid monolayer. As a result, inter-particle coupling and corresponding optical properties can be effectively controlled with DPPE/DPPE-RhB monolayer. SERS enhancement of RhB was detected, and found to increase exponentially with increasing surface pressure due to the creation of an intense electromagnetic field in inter-particle gaps. Results of this study show that the phospholipid matrix enables effective control over the inter-particle spacing in the monolayer.

In order to develop novel platforms for sensing device based on plasmonic sensing we addressed our research on optimizing refractive index sensitivity of supported silver nanocube- monolayers. Refractive index (RI) sensitivity of extinction spectra was compared experimentally for silver nanocubes in solution and in supported monolayers prepared by the Langmuir technique. The size of the nanocubes, RI of supporting dielectric substrate, and the monolayer surface pressure were used as variables in refractive index sensing (RIS) optimization. The dipolar plasmon modes of the colloidal nanocubes were found to have the highest RIS values of 176, 361 and 480 nm/RI units for 40, 80 and 130 nm cubes respectively. The largest figure of merit (FOM) of 4.55 was measured for a quadrupolar mode of 130 nm nanocubes. When compared to suspensions,

RIS of supported nanocubes were reduced by ~50%, and decreased with the monolayer surface pressure. RIS of 40 nm nanocube monolayer appeared to be sensitive to the substrate RI due to the RI- dependent dipolar plasmon modes hybridization into dipolar and quadrupolar modes. Intensity of the spectral peak corresponding to quadrupolar modes was found to increase with the angle of incident light. This work demonstrates that using high refractive index dielectric substrates, a passive molecular spacer and large angles of incidence can facilitate the detection of plasmonic response of supported nanocube monolayers.

Patterning solid surfaces with plasmonic nanostructures is demanded in nanotechnology. We present an approach to assemble plasmonic silver nanocubes into distinct patterns i.e.; circular islands and linear branched islands by exploiting the lipids phase behavior in Langmuir monolayer. Analyzing the topographic images of the LB film, an explanation of such patterns formation has been put forward. First, circular islands of silver NCs ( $3\pm 1\mu\text{m}$  in diameter) were observed in LB monolayer of DOPC/SPM/cholesterol (1:1:1) mixed with silver NCs transferred at a lateral surface pressure of 10 mN/m. This pattern was formed by specific affinity of silver NCs, coated with PVP, for condensed phase SPM/cholesterol domain. Cholesterol was found to play important role in governing the size and shape of those islands. Second pattern consisted of linear-branched chains with mean width of 1.8  $\mu\text{m}$  separated by channels having a mean width of 8.3  $\mu\text{m}$ . The islands were made of aggregates of NCs that were originally present in LE DLPC phase and the channels were made of LC phase DPPC. This periodic pattern of NCs islands was formed by phase specific localization of NCs in

Langmuir monolayer followed by alignment and phase induced deposition during the transfer process.

## **7.2. Recommendation for future work**

1. In our research work we showed that self-assembled monolayer technique can be used to engineer 2D assembly of silver nanoparticles on planar glass substrates. The same technique can be employed to make monolayer of metal nanoparticles on the curved surface such as optical fiber and further implementation of electroless metal plating, the monolayer can be made a continuous thin film that supports surface plasmon polariton (SPP). The optimum thickness of the film to support SPP can be optimized by using a tilted fiber Braggs grating (TFBG) sensor. A schematic diagram of such a sensor platform is presented in figure 7.1.a. Our research group in collaboration with professor J. Albert demonstrated fabrication of infrared fiber SPR sensor using electroless plating of gold on TFBG sensor coated with a monolayer of gold nanoparticles which is shown in figure 7.1.b (*Optics Express* **2011**, *19*, 18742-18753). A control over the kinetics of metal deposition will provide additional flexibility in batch fabrication of the TFBG-SPR sensors. However, TFBG could be inserted amongst other kinds of sensors being plated simultaneously. It is also likely that other metals could be plated and monitored in similar fashion. We also demonstrated real-time monitoring of polyelectrolytes coating on the fiber surface as well as detection of their conformational change during the deposition events using a TFBG-SPR sensor the result of which is shown in figure 7.1.c (*Optics Express* **2010**, *18*, 20409- 20421). Therefore, TFBG-SPR sensor could be employed for

studying protein dynamics and sensing bio-molecular recognition events such as antibody/antigen interaction.

2. In this thesis work we have demonstrated the optimization of refractive index sensitivity of 2D assemblies of silver nanocubes on planar substrates by tailoring size of the NCs, refractive index of the supporting substrates and the interparticles gaps within the assemblies. Similarly, silver nanocubes can be assembled on optical fiber to fabricate fiber SPR sensors with improved refractive index sensitivity. One of our attempts to assemble NCs on optical fiber using LB technique is shown in figure 7.1.d. Such fiber-SPR sensors can be employed for sensing bulk refractive index change for chemical sensing as well as bio recognition events between molecules immobilized on silver nanocubes and target molecules in a solution. However, the same fiber –SPR sensor can be used for molecular detection based on SERS and SEF. The unique advantages of this kind of SPR sensors are improved refractive index sensitivity, low fabrication cost, small volume of sensing solution and multi-functionality.
3. We showed that silver NCs form micron size circular islands and parallel stripes patterns by incorporating them in either liquid condensed phase or liquid extended phase of lipids mixture in a Langmuir monolayer. The size and shape have been found to depend on the appropriate composition of the lipids mixtures (DOPC/SPM/Cholesterol). It would be worthy to optimize the lipid mixtures and transfer processes to achieve better control of domain size to extend the approach down to the nanoscale to pattern micro scale substrates. Further study can also be

directed to justify our hypothesis that silver nanocubes preferentially interact with cholesterol rich domains of DOPC/SPM/Cholesterol raft mixture. This would provide insight into the cholesterol mediated interaction of nanoparticles with the cell membrane. Moreover, channel width of the stripe pattern exhibited by DPPC/DLPC/NCs mixture can be reduced down to nanoscale by optimizing composition of the lipid components and monolayer transfer pressure. Such stripe patterns with nanoscale channels may be used to fabricate microfluidic devices.

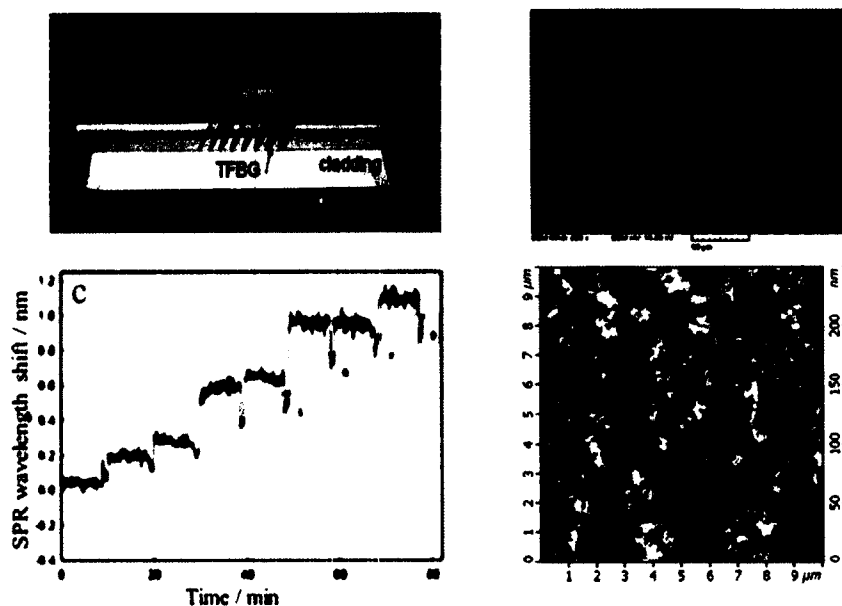


Figure 7.1 Schematic diagram of TFBG-SPR sensor platform (a), SEM image of the fiber's circumference after 45 min of electroless deposition (b), response of the TRBG-SPR sensor to the LBL deposition of polyelectrolytes (c) and AFM image of a LB monolayer of silver NCs deposited on the fiber surface (d).

4. We found that larger ( $> 80$  nm) silver NCs exhibit strong extinction signature (absorption + scattering) in UV-vis region of the spectrum. Incorporation of silver NCs within semiconductor media may increase the absorption efficiency of the semiconductor. Therefore it would be worthwhile to direct future research to incorporate silver NCs within semiconductor media to develop novel plasmonic solar cell.